ALEXANDER STUKOWSKI

ATOMIC-SCALE MODELING OF NANOSTRUCTURED METALS AND ALLOYS

Zur Erlangung des akademischen Grades des Doktors der Naturwissenschaften (Dr. rer. nat.) genehmigte Dissertation vorgelegt von Dipl.-Phys. Alexander Stukowski aus Seeheim-Jugenheim

Fachgebiet Materialmodellierung
Fachbereich Material- und Geowissenschaften
Technische Universität Darmstadt

Referent: Prof. Dr. Karsten Albe
Korreferent: Prof. Dr. Horst Hahn

Tag der Einreichung: 12. Mai 2010
Tag der Prüfung: 2. Juli 2010

Darmstadt, 2010
D 17

ATOMIC-SCALE MODELING OF NANOSTRUCTURED METALS AND ALLOYS

ALEXANDER STUKOWSKI

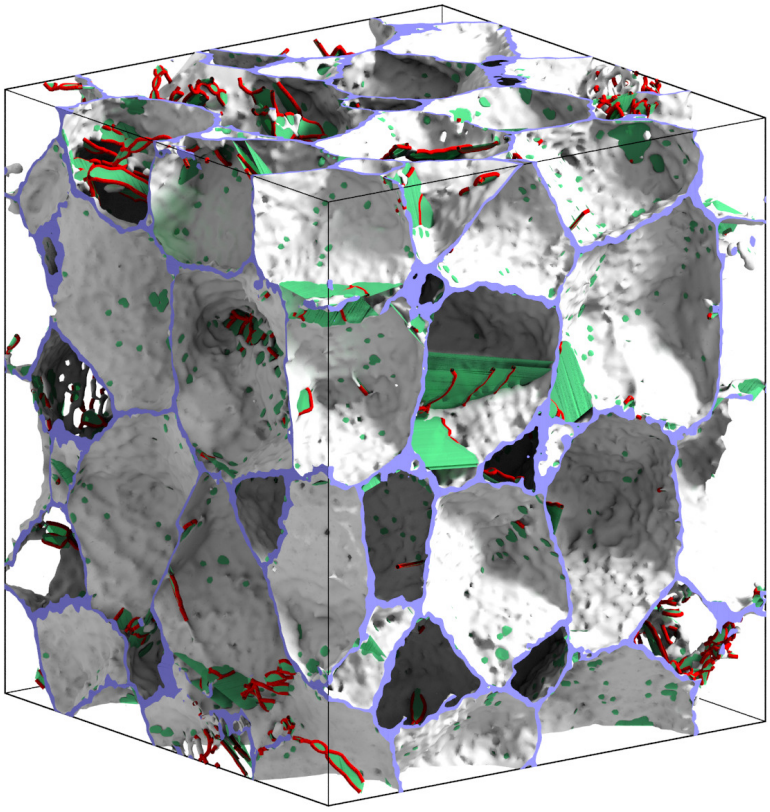

Dissertation

Mai 2010

On the cover: Nanocrystalline microstructure loaded with dislocations and twin boundaries after tensile deformation. The visualization has been derived from an atomistic simulation with the help of a new analysis method described in this thesis.

CONTENTS

LIST OF FIGURES

ABSTRACT

The prospect of realizing materials with highest strengths and other unique properties has driven a large number of research activities on nanostructured materials in recent years. The present dissertation deals with the atomic-scale modeling of nanocrystalline and nanotwinned metals and alloys, employing state-of-the-art atomistic simulation and analysis methods.

The aims of the present work are two-fold: to develop novel computational techniques in the field of atomistic materials modeling, and to use these methods to shed light on the structure and atomic-scale plasticity of nanostructured materials. In the first part of this thesis the newly developed data analyis and visualization software OVITO is described, which provides the basis for all following work. It serves as an integral part in the search for the origins of microstrain broadening in x-ray diffraction (XRD) data of nanocrystalline materials. To this end, virtual nanocrystalline structures are characterized by means of simulated diffraction experiments as well as a real-space strain field analysis. By correlating the results from the strain field analysis with the XRD measurements, conclusions on the features of nanometer-sized grains contributing to peak broadening can be drawn.

In the second part two sophisticated analysis algorithms are developed, which allow to extract the complete dislocation network from an atomistic simulation. The identification of single dislocation lines and the determination of their Burgers vector has been a laborious task usually done by hand in the past. The new method makes this information available within seconds, enabling a quantitative assessment of dislocation processes in large-scale molecular dynamics (MD) simulations. It is employed in a study of dislocation plasticity of nanotwinned metals, which can exhibt highest strength and ductility compared with their twin-free counterparts. The deformation mechanisms of Cu and Pd with ultrahigh twin densities are investigated by means of MD simulations. While nanotwins have a strengthening effect in Cu, they lead to a softening in Pd. This difference is discussed in terms of the characteristic dislocations occurring during deformation.

The third part is dedicated to nanocrystalline alloys. First, an atomistic simulation method is described that allows to model such materials by taking into account both structural and chemical equilibration in large-scale MD simulations. It is complemented by an efficient implementation of a concentration-dependent interatomic potential scheme, which enables a precise description of the energetics of mixing in multi-component systems over the whole concentration range. These tools are then employed in a study

of nanocrystalline Pd–Au. The stress-strain behavior of this miscible alloy is discussed in terms of the interplay of grain boundary solute segregation, fault energies, and grain size.

Part I

INTRODUCTION

1 INTRODUCTION

1.1 MOTIVATION

Polycrystalline materials with a grain size of less than 100 nm exhibit unique mechanical properties: some nanocrystalline (nc) metals are characterized by remarkable mechanical strength and the occurrence of superplasticity; enhanced ductility is found for ceramics at nano grain sizes and nc coatings stand out due to highly improved wear, friction and corrosion behavior. The unusual mechanical behavior of nc materials leads to a great variety of applications, like nc magnesium for hydrogen storage [219] or nc palladium for solid state gas sensor applications [192].The outstanding mechanical properties found for nc metals are a result of the mechanisms relevant for plastic deformation at small grain sizes, which fundamentally differ from those present in coarse-grained metals [183]. Plastic deformation of nanostructured metals is thought to arise from the intricate interplay between dislocation and grain boundary (GB) processes. The underlying concepts and fundamental mechanisms of this complex interplay, however, have still not been fully exposed [214], although nc metals have been studied intensively since the synthesis of the first nc metals in bulk form about 20 years ago [60]. Some of the many remaining experimental and theoretical challenges include identifying and quantifying (new) deformation mechanisms, elucidating the influence of plastic deformation on structural transformations (including structural stability against grain growth), and understanding the role of distinct structural elements of grain boundaries in deformation processes in nanocrystalline materials. The interest in the mechanical properties of nc metals has been highly increasing over the last years, which is as well attributed to the enhanced computer performance allowing more and more realistic numerical models. In the past, molecular dynamics (MD) simulations led to substantial progress in understanding plastic deformation of nc metals [215, 185, 150, 217], which motivated the present work to follow this successful route.

The work for the present dissertation was carried out within the joint research group *Plasticity of Nanocrystalline Metals and Alloys* (DFG714), funded by the Deutsche Forschungsgemeinschaft. The goal of this ongoing collaborative research effort was –and still is– to advance synthesis methods and to shed light on the structure and fundamental plastic behavior of this

promising class of materials by means of both experiments and modeling. Nanocrystalline palladium and its alloys were chosen as primary objects of investigation, mainly because of existing experimental expertise in synthesis and characterization procedures for this material, existing data on the mechanical behavior of nc Pd, and interatomic potentials, which enable atomic-scale computer simulations (see section 1.3.1).

The use of x-ray diffraction techniques has played a central role in the microstructural characterization of nc materials. They allow a determination of mean grain size and distribution [94], and also root-mean-square strain [206], through peak profile analysis. This root-mean-square strain, which is also known as *microstrain*, is an experimentally measured quantity, which is related to lattice strain fields present in the material. It is most prominent in nc materials with grain sizes of around 30 nm and below. Here, irrespective of the synthesis route, the root-mean-square magnitude of the microstrain reaches values of up to 1% [110, 180]. This is much higher than in coarse-grained materials even if they have been heavily deformed. Dislocations, however, appear not to control the microstrain broadening at the smaller grain sizes. Markmann et al. [118] found that, although the grain interiors are free of lattice defects, the microstrain of computer-generated nc structures is significant and matches closely that of experiments on samples of similar grain size. This raises the question for alternative sources of microstrain at small grain size, for instance (i) strain fields due to stress concentrations at the many triple junctions, (ii) displacement fields near grain boundaries, and (iii) strain caused by compatibility constraints [205]. To elucidate the nature of the experimentally measured microstrain, one key idea followed in this thesis is to exploit the full atomic-scale structure information provided by computer-generated samples to interpret results of experimental diffraction data analysis. We study the origin of x-ray microstrain broadening in nanocrystalline metals generated via molecular dynamics simulation by combining the simulated diffraction approach with a direct analysis of the atomic displacement fields (performed in real space). In particular, we address the following questions in chapter 3:

(i) Does the microstrain inferred from the x-ray data analysis reflect real atomic disorder, or is it merely an artifact originating from the scattering data analysis?

(ii) What is the microscopic nature and origin of the displacement fields that cause the reflection broadening?

In order to make a comparison with experimental microstrain data possible, an atomistically defined measure of the local lattice distortions must be developed that allows to identify those regions of the crystal that effectively contribute to x-ray microstrain broadening.

The grain size of polycrystals can be refined to the nanometer regime only under extreme conditions, and in pure metals, a grain size in the nanometer range is difficult to stabilize against the strong driving force for grain growth. That is why segregating solutes have been used to prevent grain growth, which occurs even at room temperature in nanocrystalline metals [62, 206, 43]. Even though the atomic-scale structure and mechanical properties of segregating nc alloys have been studied to some extend, much less attention has been paid to miscible solutes that in principle allow to specifically tune important materials properties, which control the mechanical behavior: The nucleation of partial dislocations, for instance, is stimulated by miscible solutes as shown by Rajgarhia et al. [142] in MD simulations. Alloying also affects the thermal stability of grain boundaries and leads to a variation of the generalized planar fault energy (GPFE) of the bulk material [86, 126, 127, 128, 95, 28], which in turn controls many dislocation processes [185] and determines the twinnability of the material [10, 169, 84, 85]. Moreover, it is well known that the grain boundary structure and energy depends on the type and number of solutes [177], and chemically enhanced equilibration of GBs might affect the mechanical properties of alloyed nanocrystals. The complex interplay of these various factors affecting the deformation behavior of nanocrystalline alloys will be studied in chapter 7 using molecular dynamics simulations for the case of the Pd–Au miscible alloy system. To this end, new simulation techniques need to be developed first (chapter 6). The virtual samples of various grain sizes are prepared with a hybrid MD/Monte-Carlo scheme accounting for both structural and chemical equilibration, which we will describe in section 6.2. Since modeling of nanocrystalline structures requires extended system sizes with several millions of atoms, efficient parallelization strategies need to be devised to handle large systems in Monte-Carlo simulations. In addition, an interatomic potential is required to model the Pd–Au binary. To this end, we first refine the so-called concentration-dependent embedded atom method (CD-EAM) [26], to enable efficient Monte-Carlo simulations based on this advanced potential scheme (section 6.3). Finally, we use the CD-EAM model to derive a cross-potential for the Pd–Au binary on the basis of existing EAM potentials for the pure constituents.

In the conventional grain size regime, a reduction in grain size usually leads to an increase in ductility. In the nanocrystalline regime, however, one often finds disappointingly low tensile ductilities, typically less than 2% elongation for most nanocrystalline metals with grain sizes <25 nm [91, 100]. In addition to processing artifacts (pores) present in such materials, Koch [90] identified tensile instabilities and crack nucleation or shear instability as sources of limited ductility. The low work hardening rate of many nc materials leads to early strain localization and failure. So far, this trade-

off between strength and ductility of nanocrystalline materials has limited their applications. Several recent experimental studies have shown, however, that nanoscale growth twins in ultrafine Cu can significantly improve mechanical properties as compared to twin-free samples. In tensile tests and nanoindentation experiments, nanotwinned samples with various twin densities exhibit higher yield strength, tensile strength, and hardness, as well as ductility [113, 36, 112]. The observed increase in strength with decreasing twin boundary distance is comparable to that found for conventional grain size refinement. That is, nanoscale twin boundaries seem to impart as much strengthening as conventional high-angle GBs by blocking dislocation motion [113, 111] and exhibit a Hall–Petch type behavior. In contrast to nanocrystalline Cu with general GBs, however, nanotwinned Cu does not lose its tensile ductility when refined to the nanometer regime. In addition, twin boundaries usually exhibit much higher mechanical and thermal stability, and less electric resistivity in comparison to other grain boundaries [114, 111].

With only a very few exceptions [59, 57, 98], most work on the effect of growth twins on the mechanical properties of metals have been performed in Cu. Frøseth et al. [59, 57], however, have reported that nanotwinned Al exhibits enhanced plasticity in constant-stress simulations compared to its twin-free counterpart. This result suggests that other nanotwinned face-centered cubic (fcc) materials might not show the strengthening effect found for Cu. Jin et al. [78, 77] studied the interaction of single dislocations with a twin boundary in Cu, Ni, and Al. They found several possible reactions, being dependent on the material's energy barriers, type of dislocation, and loading condition. For nanotwinned Pd, however, Kulkarni et al. [98] predict a performance based on simulated indentation studies that is very similar to Cu. In view of these results, the question arises whether the strengthening effect of twins observed in Cu is a general phenomenon present in all fcc metals. To address this question, we will accurately compare the behavior of both nanotwinned Cu and Pd under realistic conditions using large-scale MD simulations of Cu and Pd polycrystals. In particular, we employ a newly developed dislocation analysis method that allows us to study the numbers and types of dislocations that occur during deformation, compare them to experimental measurements, and finally, to link these microscopic processes to the macroscopic stress-strain behavior of fcc metals.

In general, the MD simulation method used throughout the present work yields two types of output: (i) the thermodynamic properties of the simulated system, like total energy, temperature, and pressure/stress as functions of simulation time, and (ii) the trajectories of the atoms. The thermodynamic data can be directly used to interpret the general behavior of the system, for example, by relating it to experimental measurements of macroscopic

properties like the stress–strain curve. But the atomic coordinates are in fact the more valuable output, because they contain a wealth of information, which is usually not accessible via experimental techniques. They describe the state and the evolution of the system in its entirety. The raw atomic coordinates alone, however, are not sufficient to enable an instructive sight into the material. Usually, sophisticated tools and post-processing methods are required to exploit this data and to visualize it to enable a meaningful interpretation by the scientist.

The development of such analysis methods is one of the main goals addressed by the present work. Various techniques have been developed in the past to identify individual atoms in a simulation that are part of crystal defects such as dislocations and grain boundaries. Their level of sophistication ranges from very simple (e.g. coordination number, atomic excess energy [21]) to elaborate (e.g. common neighbor analysis [72], centro-symmetry parameter [83], Ackland's bond-angle method [4]). These methods are more or less well suited for a visualization of the defect structures by masking out all other regular crystalline atoms which occlude the area of interest. None of these methods, however, is capable of determining the type of a crystal defect (dislocation, vacancy, grain boundary etc.) or any quantitative higher-level information like the Burgers vector of a dislocation. Loosely speaking, we are stuck in the atomistic picture of the crystalline material, which is essentially an 'overloaded' description if we want to understand deformation processes on larger scales.

Some primitive attempts have been made to characterize dislocations in atomistic simulations, for instance, by analyzing the elastic strain field induced by a dislocation, which, in principle, allows to determine its Burgers vector [65]. Vo et al. [191] devised a post mortem method that approximately yields the total plastic slip produced by dislocations, but gives no information on the types and numbers of dislocations involved. Thus, the available existing techniques are clearly unsatisfactory, and in chapter 4 we will develop methods for extracting dislocation lines and other crystal defects in a fully automated way, greatly enhancing the value of atomistic simulations of crystal plasticity.

In general, powerful visualization techniques for simulation data play a key role in materials modeling, in particular since the simulated systems constantly become larger and more complex. The task of visualization software is to translate the raw data generated by a numerical simulation model into a meaningful graphical representation to enable an interpretation by the scientist. During the last decade, several efforts have led to the development of extensive data analysis and visualization software packages like ParaView [88] and VisIt [40], which can process arbitrary scalar and vector fields defined on 2D and 3D structured and unstructured meshes. Since

these package have mainly been designed for the processing of continuum-based simulations (e.g. finite element methods), most researchers resort to specialized tools like RasMol [149], AtomEye [103], or Vmd [75] when it comes to the visualization of atomistic simulations. The capabilities of these existing tools are, however, limited with respect to the available analysis functions and the data size that can be visualized. As part of this work, we have developed a novel analysis and visualization software for atomistic simulation data, providing capabilities that go beyond those of established, but insufficient solutions. This software will be described in some detail in chapter 2 and provides the basis for all following scientific work.

Note that this thesis is divided into three parts following the introductory chapter. Each part begins with a chapter describing the newly developed tools and methodologies that ultimately enabled the scientific investigations presented in the subsequent chapter.

1.2 PLASTICITY OF NANOCRYSTALLINE MATERIALS

In this introductory section we want to give a brief review of the deformation mechanisms that govern the plasticity of nanocrystalline metals according to the current understanding.

Nanocrystalline materials, which have a grain size below 100 nm, are being actively investigated because of unique mechanical properties, which can include increased strength and hardness, improved toughness, reduced elastic modulus and ductility, and other materials properties like enhanced diffusivity. Some of these remarkable mechanical properties of nanocrystalline materials are highly desirable for structural applications. Thus, to optimize the mechanical behavior, it is important to identify its underlying mechanisms. In the following we give an overview of the most important findings on the wide range of mechanisms that can play a role in nanocrystalline metals.

1.2.1 *Non-dislocation based deformation mechanisms*

The Hall–Petch relationship predicts that the yield stress increases with the inverse of the square root of the grain size [35]. This behavior, however, cannot be extrapolated to very small grain sizes. Experimental results on nanocrystalline materials show either a reduced slope, a plateau or even a decrease of the yield stress below a critical grain size (called the *negative* Hall–Petch effect [29]). Yet, there is no clear evidence for the nature of the strength–grain size relationship at grain sizes below $\sim$ 10-15 nm. Even

though a softening below this critical grain size has been oberserved in MD simulations [150, 151], more recent investigations indicate that the strength is controlled not only by the grain size alone, but by a combination of both grain size and degree of grain boundary relaxation [190] – a factor that has been ignored in earlier studies. In summary, the negative Hall–Petch effect is still being debated as there is insufficient reliable data to validate the existence of this effect.

The conventional Hall–Petch relationship is based on the concept of dislocation pile-ups. As the grain size is decreased, the number of dislocations piled up against a grain boundary is reduced, since this number is a function of the distance to the source for a given stress level. Conversely, an increased stress level is required to generate the same number of dislocations at a pile-up. Below a critical grain size, one can no longer use the pile-up concept to explain plastic flow: The number of dislocations at the pile-up is eventually reduced to one, and the multiplying effect on the stress field is lost [136]. A large number of experimental studies and atomistic computer simulations (for reviews see Refs. [124, 35, 209, 207]) confirmed that inside grains of 100 nm or less the development of required dislocation fluxes for plastic flow begins to become severely curtailed. At this crystallite size, conventional dislocation sources based on the Frank-Read mechanisms cannot operate [188] and dislocation glide is impeded by the high density of grain boundaries. Instead, the resulting high stress levels lead to a substantial contribution of grain boundary processes to plasticity, such as grain boundary sliding, grain rotation, diffusional creep, twinning and faulting, grain boundary migration, and intergranular fracture.

Grain boundary sliding is the principal deformation mechanism of superplasticity and has been proposed to be the dominant mechanism in nanocrystalline materials at grain sizes <50 nm. Here, plastic deformation takes place by virtue of a layer of grains being translated with respect to a neighboring layer. Van Swygenhoven et al. [184, 187] found GB sliding to be the primary deformation mechanism in molecular dynamics simulations of nanocrystalline structures. The sliding is facilitated by atomic shuffling and stress-assisted volume migration.

The activation of alternative deformation mechanisms like GB sliding is also confirmed by experimental measurements of strain rate sensitivity, which increases at small grain size [202, 121]. The increased strain rate sensitivity is directly related to a change in the rate controlling mechanisms of plastic deformation through their activation volume [113]. A high strain rate sensitivity is indicative of a smaller activation volume. Conventional fcc metals have a large activation volume, $V \approx (10^2 - 10^3)b^3$, which is associated with dislocations cutting through forest dislocations. On the other hand, the

activation volume for GB diffusion processes is much lower, on the order of the atomic volume, $V \approx (1-10)b^3$.

Grain rotation has been proposed as another deformation mechanism that becomes active at small grain sizes. The rotation is facilitated by the motion of partial disclination dipoles, causing plastic flow accompanied by crystal lattice rotation behind the disclinations [135, 132]. During plastic deformation, two neighboring grains might rotate in a fashion that brings their orientations closer together. This leads to the elimination of the dislocation barrier constituted by the grain boundary between them, now providing an extended path for dislocation motion. Note that this mechanism can actually lead to a softening and localization, which is in agreement with the limited ductility found for many nanocrystalline metals.

Conventional constitutive models for mechanical twinning predict that a decrease in grain size is expected to render deformation twinning more difficult [125]. This is especially the case for metals with high stacking fault energies like Al, which either require extremely high shear stresses or large critical nucleus sizes to enable the formation of twins. Thus, from a theoretical point of view, nanocrystalline metals do not posses the ability of twinning. Surprisingly, several experimental investigations revealed twins in TEM images of nanocrystalline Al after deformation [107]. They followed an earlier prediction of deformation twinning made on the basis of MD simulations of nanocrystalline Al [212]. The experiments confirmed that deformation twins can form via the dynamic overlapping of stacking fault ribbons associated with Shockley partial dislocations emitted from grain boundaries. The experimentally observed deformation twins are, however, not as prevalent as predicted by the MD simulations, which is likely to result from the differences in deformation conditions, in particular the extremely high strain rates applied in MD simulations (see section 1.3.3).

The existing experimental and theoretical results indicate that there is not *the* prevalent deformation mechanism in nc metals. Instead, depending on grain size, temperature, and stress and strain rate different mechanisms may be dominant. Some attempts to summarize these insights on microscopic processes in the form of deformation mechanism maps have been made. Figure 1 shows two such maps with alternative parametrizations (stress and strain rate vs. grain size).

1.2.2 *Dislocations in nanocrystalline metals*

Even though alternative mechanisms like the ones described in the previous section compete with dislocation slip in the nanocrystalline regime, dislocation slip is still a major contributor to plastic flow in most cases. In the

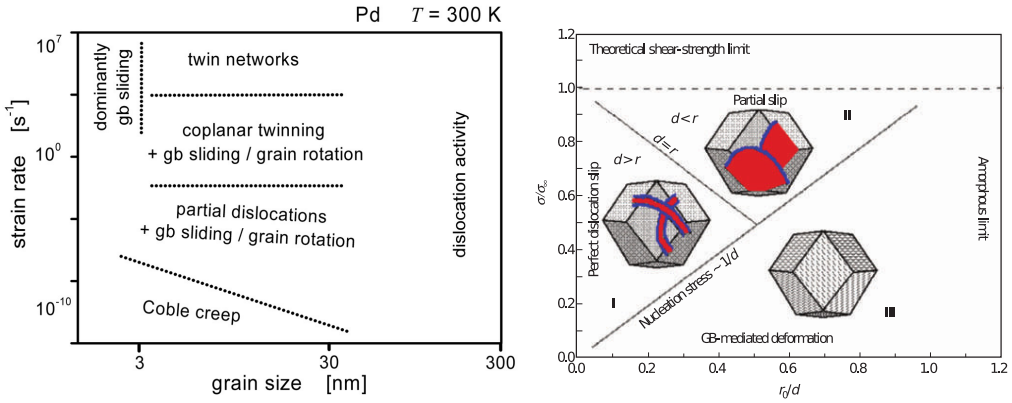

Figure 1: Proposed deformation mechanism maps for nanocrystalline fcc metals. (a) Map from Ref. [207] displays results from experiments as well as MD simulations, which predict a variation of the dominating mechanisms over a wide range of strain rates. (b) The second map from Ref. [215] defines regions in which either complete extended dislocations (region I) or partial dislocations (region II), or no dislocations at all (region III) exist at low-temperatures. The map is expressed in reduced units of stress and inverse grain size. The parameters r_0 (equilibrium dislocation splitting distance) and σ_∞ (resolved shear stress for infinite splitting distance) are functions of the stacking fault energy and the elastic properties of the material.

conventional polycrystalline regime, the material contains a significant density of pre-existing dislocations and, in addition, grain boundary ledges act as sources for dislocations at the onset of plastic deformation [102], which are then further multiplied. In the nanocrystalline regime, however, grain boundaries are virtually free of such ledges, and the mean free path of dislocations is reduced such that dislocation reactions, double cross slip, and other mechanisms of dislocation multiplication are effectively prohibited.

It was shown primarily by means of molecular dynamics simulations that grain boundaries act as sources and sinks for dislocations in nanocrystalline metals [215, 150, 151, 186]. The reduced mean free path of dislocations does not enable work hardening based on processes like cross slip. Thus, the dislocation density remains low throughout the plastic deformation process. Dislocations, which are nucleated at one grain boundary, run almost unimpeded until they encounter the opposing grain boundary, where they are absorbed. The predicted stresses to nucleate a dislocation loop with a small radius on the order of the grain size are quite high. The actual global stress at which dislocations are emitted from a GB can, however, actually be

considerably lower because of the stress concentration effect from adjacent GBs.

Some experiments indicate that many grain boundaries in nc metals are in non-equilibrium, that is, they contain a large number of GB dislocations [73]. One could assume that such non-equilibrium GBs are ready candidates for emission of dislocations into the grain interiors. Contrary to this picture, nanocrystalline GBs have been reported to be not as different from the ones in conventional polycrystals as initially suspected, apart from an increased triple junction density. Early reports of GBs being an amorphous layer of considerable thickness have not been confirmed and could be due to incomplete densification during synthesis. The stacking fault ribbon width (separation distance between Shockley partials) in nanocrystalline metals with high stacking faults energies is larger than in the respective coarse-grained counterparts [7, 105]. In nc metals with low stacking fault energies, the emission of trailing partials from the grain boundaries can be severely limited. This is why deformation twins and stacking faults across grains were found ubiquitous in such materials [106].

MD simulations of nanocrystalline fcc metals have shown that dislocation emission always happens by nucleation of Shockley partials from the grain boundaries. Depending on the magnitude of the aforementioned stacking fault energy, a trailing partial might or might not follow it. It was emphasized by Van Swygenhoven and co-workers, however, that the entire generalized planar fault energy curve (GPFE) [223] must be taken into consideration, and it was proposed that the ratio of the unstable and intrinsic stacking fault energies is more appropriate to describe the observed dislocation activity in nanocrystalline samples. If this ratio is close to unity, full dislocations are anticipated during the deformation process; conversely, if this ratio is high, extended partial dislocations are expected within the nanocrystalline grains.

Furthermore, nucleation of dislocations in nc metals is influenced by two factors: the resolved shear stress of the corresponding slip system and the structure of the GB. For example, the discrete lattice dislocations that constitute a low-angle grain boundary can become mobile at a certain strain level and the grain boundary disappears [51]. A similar behavior has been reported for grain boundaries having a configuration close to the coherent twin configuration [58, 12]. For these vicinal twin boundaries, relatively low stresses are required for the GB to emit dislocations, which ultimately let the GB evolve further to the favorable coherent twin configuration [51]. The mechanisms of dislocation nucleation and absorption have been studied in various MD simulations using a bicrystal geometry, showing that the local GB structure determines the preferred dislocation nucleation and dislocation absorption sites in the GBs [175, 162]. In particular it was found that the dissociated interface structural units in certain GBs play a strong role

in the dislocation nucleation process, serving as the nucleation points for dislocations [163].

After nucleation, the propagation of a dislocation segment along the grain boundaries is hindered by a pinning–depinning mechanism influenced by the relative orientation between the Burgers vector and the ledge geometry of the grain boundary [186]. In a recent paper, however, Van Swygenhoven and co-workers report dislocation cross-slip during dislocation propagation suggesting that the observed lack of strain hardening in constant strain rate MD simulations might be due to the ability of a screw dislocation segment to bypass pinning sites [11] on the GB. Detailed temporal analysis of these atomic processes revealed that the cross-slip process is initiated at the intersection between the dislocation segment and the GB. In a more quantitative analysis of the critical resolved shear stresses associated with dislocation activity, it was found that dislocation propagation constitutes the rate-limiting plastic process in finite temperature MD simulations [12].

Vo et al. [191] have quantified the respective contributions of dislocation glide and non-dislocation based deformation mechanisms to the total plastic slip in MD simulations of nanocrystalline Cu. They conclude that dislocations significantly contribute to plastic deformation of nanocrystalline materials for grain sizes as small as 5 nm. Up to 50% of net strain is produced by dislocation glide. Given the extremely high strain rate of $10^8\,\mathrm{s}^{-1}$ used in the simulation, this result cannot, however, directly be carried over to experiments.

1.3 METHODS

1.3.1 *Molecular dynamics*

At the nanometer scale conventional continuum concepts are no longer valid, and one has to take the discrete nature of the constituting atoms into account. This is the main reason why we use atomistic simulation methods in the present dissertation to study the structure and plasticity of nanostructured materials.

First-principles simulation methods like density functional theory (DFT) [71, 92] solve the electronic many-body problem to calculate the total energy of an atomic system. This quantum-mechanical treatment of electrons allows one to study materials on the atomic scale very accurately. However, there are many physical processes whose natural length and time scales lie outside the domain currently accessible by first-principal methods. This is especially true for those systems studied in the present thesis, which involve several millions of atoms. Access to this scale is afforded by (semi-)empiricial inter-

atomic potentials. An interatomic postential is a relatively simple analytic function that expresses the total potantial energy, E, of a system in terms of the atomic (ion) positions, $\{\boldsymbol{r}_i\}$ (a point in configuration space). The molecular dynamics (MD) method can be used to calculate the trajectories of the simulated particles. This method requires multiple evaluations of the Newtonian forces $\boldsymbol{F}_i = -\partial E/\partial \boldsymbol{r}_i$ acting on individual atoms. Such interatomic potentials are called empricial because they do not involve any quantum-mechanical calculations, although they are often used during the development of the potentials. The potential functions contain fitting parameters, which are adjusted to reproduce selected properties of the material known from experiment and/or first-principles calculations. The underlying assumption is that a potential, which gives accurate energies and forces on configurations points used during the fit, will also give reasonable results for configurations between and beyond those points (transferability property).

Simple empirical potentials like Lennard-Jones and Morse potentials have been used for materials modeling for several decades. They describe the total energy as a sum of pair-wise terms, which, in most cases, is an oversimplification of the atomic bonding. For metallic systems, the presently most widely used potential format is given by the embedded atom method (EAM) [37, 38] and the Finnis-Sinclair (FS) scheme [53]. Although initially derived from different physical approaches, the two potential forms are similar. Here we introduce the notation of the EAM, which postulates the total potential energy of an N atom system as

$$E = \frac{1}{2}\sum_{i}^{N}\sum_{j\neq i}^{N} V_{\alpha_i\beta_j}(r_{ij}) + \sum_{i}^{N} F_{\alpha_i}(\varrho_i), \tag{1.1}$$

where the first term is the sum of pair interactions, $V_{\alpha_i\beta_j}(r_{ij})$ is the pair interaction between atom i (of chemical identity α_i) and atom j (of chemical identity β_j), and F_{α_i} represents the embedding energy of atom i in the host of electron density ϱ_i induced at site i by all other atoms. The host electron density is given by

$$\varrho_i = \sum_{j\neq i}^{N} \rho_{\alpha_j}(r_{ij}), \tag{1.2}$$

where $\rho_{\alpha_j}(r_{ij})$ is the electron density function assigned to atom j. The second term in equation 1.1 represents, in an approximate manner, the many-body interactions responsible for a significant part of bonding in metals. Since the interactions are short-ranged, the functions $V_{\alpha_i\beta_j}(r_{ij})$ and $\rho_{\alpha_j}(r_{ij})$ can be taken as effectively zero beyond some cutoff r_c, which usually includes the first three or four neighbor shells of an atom. This allows to calculate the total energy and atomic forces of large systems efficiently in $\mathcal{O}(N)$ time.

An EAM description of an elemental metal is given by three functions: $V(r)$, $\rho(r)$, and $F(\varrho)$. A binary system A–B is represented by seven functions $V_{AA}(r)$, $V_{AB}(r)$, $V_{BB}(r)$, $\rho_A(r)$, $\rho_B(r)$, $F_A(\varrho)$, and $F_B(\varrho)$. Thus, if potential functions for two metals A and B are available, only the cross-interaction potential $V_{AB}(r)$ is needed for a full description of the binary alloy. In chapter 6 we will introduce an extension to the EAM, which is not restricted to a static choice of the cross potential, but which employs a composition-dependent functional to accurately describe the energetics of the binary alloy over the whole concentration range.

The MD simulations presented in this dissertation have been carried out with the popular simulation code LAMMPS [139], which is freely available. Besides a rich set of potential schemes and simulation control options LAMMPS supports massively-parallel simulations on large computing clusters. The distribution of a simulation to multiple compute nodes is required to enable multi-million atom MD simulations over a physical time scale of nanoseconds.

As discussed above, the selection of a proper interatomic potential is crucial for a realistic MD simulation, since the choice of the potential determines all properties of the simulated material, ranging from the interaction of single atoms to the activation energy of deformation processes as well as the macroscopic stress-strain behavior. Table 1 lists basic properties of several existing EAM type potentials for Pd found in the literature and gives a comparison with experimental values and first-principles calculations.

For the present simulations of Pd, we have employed the 1986 Foiles potential [55] and the 2001 Hoyt–Foiles [56] potential. The 1986 Foiles potential is a traditional choice that has been used for several studies of nc Pd structures in the past [213, 211, 66, 67, 82]. Due to its unnaturally low stacking fault energy, however, it is not well suited for simulations of plastic deformation, which strongly depends on the characteristics of partial dislocations and stacking faults. Hence, we use this potential in chapter 3 to model equilibrium structures, which are subjected to a simulated x-ray diffraction analysis, only. For modeling plasticity of nanostructured Pd, we rely to the newer Hoyt–Foiles potential, which shows the best agreement with first-principle calculations of stable and unstable stacking fault energies (Figure 36 in chapter 5 gives the full generalized stacking fault energy curve for this potential). Moreover, it does not suffer from a spurious underestimation of the surface energy, like for example the Von Sydow potential [193], which leads to an early rupture of the material in simulated tensile tests.

Potential type Author	Expt.	Theory / First-principles	TB-SMA [193] (von Sydow)	EAM [55] (Foiles)	TB-SMA [137] (Papanicolaou)	EAM [56] (Hoyt/Foiles)	TB-SMA [30] (Cleri/Rosato)	FS [167] (Sutton/Chen)
a_0 (Å)	3.89 [87] [17]	3.90 [174] 3.88 [196]	3.90 [193]	3.89 [55]	3.844 [137]	3.89 [56]	3.887 [30]	3.89 [167]
E_{coh} (eV/atom)	3.89 [87]	3.37 [174] 4.63 [196]	3.37 [193]	3.91 [38]	3.90	3.91 [56]	3.94 [30]	3.94 [167]
C_{11} (GPa)	234.1 [159] 224 [17]	232 [196]	292	218 [55]	258 [137]	239 [56]	232 [30]	248 [167]
C_{12} (GPa)	176.1 [159] 173 [17]	196 [196]	189	184 [55]	199 [137]	174 [56]	178 [30]	176 [167]
C_{44} (GPa)	71.2 [159] 71.6 [17]	60 [196]	124	65 [55]	75 [137]	66 [56]	73 [30]	93 [167]
B (GPa)	181 [87] 187 [17]	215 [174] 208 [196]	223 [193]	195 [55]	219 [137]	196	196 [30]	200 [167]
T_{melt} (K)	1825 [54]		1596	1390 [54]				
$E_{f,\mathrm{vac}}$ (eV)	1.4 [153]	1.70 [120]	1.20	1.44 [55]	0.96 [137]	1.58 [56]	0.96	
$\Delta V_{\mathrm{vac}}/\Omega$			-0.14	-0.39	-0.23		-0.25	
γ_{isf} (mJ/m^2)	180 ± 40 [44]	186 [64]	180 [193]	15	0	184	0	
γ_{esf} (mJ/m^2)		178 [64]	180 [193]					
γ_{twb} (mJ/m^2)		89 [64]	90 [193]					
γ_{us} (mJ/m^2)		265 [10]	322	130	160	213	142	
$E_{(111)}$ (mJ/m^2)		1640 [123]	833	1220 [55]	740 [137]	1925	732	
$E_{(100)}$ (mJ/m^2)		1860 [123]	950	1370 [55]	860 [137]	1981	847	
$E_{(100)}$ (eV/atom)		0.89 [123] 1.006 [196]						
$E_{(110)}$ (mJ/m^2)		1970 [123]	1034	1490 [55]	930 [137]	2200	914	

Table 1: Materials properties of palladium as derived using several Pd potentials in comparison to experimental data and first-principles calculations. Given are the lattice constant a_0, cohesive energy per atom E_{coh}, elastic moduli C_{ij}, bulk modulus B, melting point T_{melt}, vacancy formation energy $E_{f,\mathrm{vac}}$ and relaxation volume $\Delta V_{\mathrm{vac}}/\Omega$, intrinsic stacking-fault energy γ_{isf}, extrinsic stacking-fault energy γ_{esf}, twin-boundary energy γ_{twb}, unstable-stacking energy γ_{us}, and surface energies $E_{(surf)}$. Source references are given in brackets; values without a reference have been calculated by the author.

1.3.2 *Structure preparation*

Nanocrystalline metals can nowadays be synthesized with experimental techniques in several ways. One can classify the existing approaches into *bottom-up* and *top-down*. In the *bottom-up* approaches the nanostructure is built up by arranging smaller units like nanoparticles or single atoms into a nanocrystalline microstructure. In the *top-down* approaches one starts with a coarse-grained bulk material and breaks down the microstructure into a nanostructure with smaller grains. The most common methods are *inert gas condensation*, *mechanical alloying*, *electrodeposition*, *crystallization from amorphous solids*, and *severe plastic deformation*. One has to bear in mind that the synthesis method can have a direct influence on the mechanical properties of the resulting nanocrystalline material. In general, the average grain size is not sufficient to fully characterize a microstructure. Depending on the synthesis route, the mechanical properties can be masked or distorted by additional characteristics and flaws, as for example porosity, which is very common in *bottom-up* produced microstructures [148]. Such processing flaws are known to be detrimental to the strength of the material and could give an explanation for the large variety of experimental observations described in the literature.

When studying the plasticity of nanocrystalline metals with MD, however, an additional problem arises: One requires virtual model structures for the simulation of deformation experiments at the atomic level. In general, it is inconvenient –and in the vast majority of cases completely impossible– to obtain such structures by simulating the aforementioned, experimental synthesis routes with MD. Although a few such attempts have been made [80, 220], the intrinsic limitations of the MD method (see next section) necessitate the usage of alternative, more direct preparation methods for virtual nanostructures.

At present, the most popular method for preparing nanocrystalline computer samples is the so-called Voronoi method. The name derives from the Voronoi tessellation procedure [194] for decomposing the simulation box into geometric cells, which constitute the individual grains. First, N space points in the simulation box are choosen, the so called Voronoi sites, forming the seeds of the N crystal grains to be created. Based on this set of Voronoi points, the geometric grain cells are constructed according to the Voronoi tessellation method. Each cell around a Voronoi point encompasses, by definition, all points in space being closer to the cell's center site than to any of the other Voronoi points. The Voronoi cells are convex polyhedra bounded by planes located halfway between neighboring Voronoi points, similar to the Wigner-Seitz construction.

The choice of the Voronoi points determines the size and shape of the final grains as well as the number and area of grain boundaries and number of triple junctions etc. It has been shown that a uniform distribution of random points leads to the Poisson-Voronoi grain size distribution [61]. In the case of atomistic simulation this is an acceptable approximation of the log-normal grain size distribution often found in real samples [34] since the number of simulated grains is usually limited to a few hundred. In certain cases, for example in mesoscale simulations, a larger number of grains with a specific size distribution is required. This can be achieved with Monte-Carlo methods, which adjust the location of the Voronoi points such that a more realistic (e.g. log-normal) grain size distribution is reproduced [61]. Similar stochastic approaches can help to tailor the grain shape distribution, the number of triple junction, triple junction dihedral angles, and other topological characteristics of the grain boundary network to specific needs.

In the next step, the grains are filled with atoms on randomly oriented lattices inscribed into the geometric Voronoi cells. Note that the obtained grain boundaries are initially very far from equilibrium having a high-energy state. Thus, the aim of a final relaxation or annealing step is to equilibrate the atomic configurations in the grain boundaries. In general, it is not possible to fully equilibrate these artificial GBs due to the limited time scale of the MD method ($\approx 1\,\mathrm{ns}$). That is, the state of the virtual GBs might still differ from the one of experimental GBs, which are themselves only a manifestation of a meta-stable state in a one-component system.

1.3.3 *Studying mechanical behavior*

For studying the deformation processes in nanocrystalline structures, we perform strain-controlled tensile tests (chapters 5 and 7). During such a simulation, the cubic simulation cell is continuously stretched in one dimension (z-axis) at a constant engineering strain rate while its dimensions in the other two directions are adjusted such that the pressure components p_{xx} and p_{yy} are zero (uniaxial stress state). This relaxation is performed with the help of Berendsen's barostat method [9].

At the nanocrystalline level, several deformation mechanisms are active, as discussed in section 1.2.1. Since MD directly models each and every individual atom, it directly incorporates the atomic degrees of freedom necessary to describe this multitude of processes in a realistic way. While MD is very attractive, it is not without its own limitations. Especially the time and length scales of processes that can be modeled with this method are limited. The trajectories of atoms are calculated in MD using an explicit time integration algorithm that imposes a stability limit on the maximum time

step, which has to be a fraction of the period of thermal atomic vibrations (a few femtoseconds). This limits the achievable physical time scale, which can be accessed within a reasonable computation time. All current MD-based deformation simulations are therefore performed at extremely high strain rates ($10^7\,s^{-1}$ and higher), to advance into the plastic strain regime. One has to bear this difference in mind when comparing simulated experiments with real experiments, which are performed at much lower strain rates (around $10^{-4}\,s^{-1}$ [46]). The usage of high strain rates in MD simulations implies that the contribution of thermally activated processes is considerably reduced, and one can expect higher yield and flow stresses than in experiments in such simulations.

Note that in some instances one wants to study equilibrium properties of a materials system. But reaching the stable equilibrium state by following the normal kinetics of the system can take arbitrarily long times. In such cases we will resort to other simulation methods like the Metropolis Monte-Carlo technique, which is described in chapter 6 in some detail. The atomistic description of a crystalline material requires a large number of particles, even for smallest sample sizes. Even though modern massively-parallel computers can handle millions or even billions of atoms in MD simulations [3], this limits the maximum sample or representative volume size, which can be investigated. Of course, if the sample size is limited, the maximum feature size (for instance the grain size of nanocrystalline materials) is restricted as well. In the present dissertation periodic boundary conditions are employed in all simulations to model bulk-like structures, which are only tens of

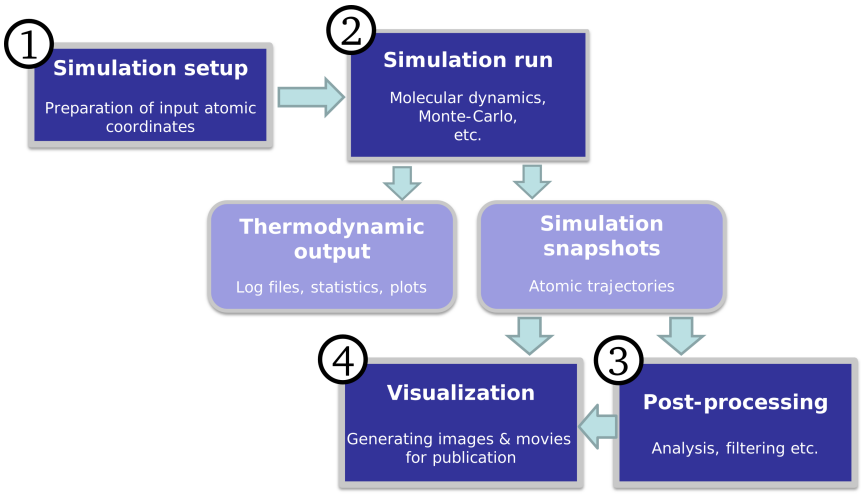

Figure 2: Typical workflow of atomistic simulations in materials modeling. The individual steps are discussed in the text.

nanometers in size. But the periodic boundary conditions let atoms on one side of the simulation cell interact with atoms on the opposite side, effectively eliminating the effect of free surfaces.

In spite of the aforementioned limitations, MD has provided invaluable insights into the details of plastic deformation processes at the atomic scale, which could not have been obtained with experimental measurements alone. During the last years MD has become one of the main tools for studying the properties of nanostructured materials and its predictions are leading our understanding of these materials.

Figure 2 summarizes the typical steps involved in a MD simulation. The input preparation (1) and the simulation step (2) have already been discussed in sections 1.3.1 and 1.3.2. The analysis (3) and visualization (4) of simulation snapshots are major subjects of this dissertation (chapters 2 and 4). One basic analysis method used throughout the present work is the common neighbor analysis (CNA) [72]. It provides a means to identify atoms belonging to crystal defects (dislocations, stacking faults, grain boundaries, etc.) by comparing the interconnectivity of bonds between nearest neighbors to known patterns, which are characteristic for atoms in the perfect lattice (see figure 28 on page 83 for an example).

Part II

CHARACTERIZATION OF NANOCRYSTALLINE STRUCTURES

2

OVITO - VISUALIZATION AND ANALYSIS SOFTWARE FOR ATOMISTIC SIMULATION DATA

2.1 MOTIVATION

Molecular dynamics, molecular statics and Monte-Carlo based simulations are standard methods for materials modeling with atomic scale resolution. Such atomistic simulations yield temporal-spatial information on three-dimensional atomic configurations and/or atom trajectories, which have to be analyzed in order to gain scientific insights into a physical system.

Thus, powerful visualization techniques play a key role, moreover since the simulated systems become larger and more complex. The task of visualization software is to translate the raw atomic coordinates generated by the simulation code into a meaningful graphical representation to enable an interpretation by the scientist. In many cases, sophisticated analysis techniques (see chapter 4) can help to extract more essential information from the atomistic system. Again, it is the task of visualization software to produce a meaningful depiction of this derived data.

Existing software packages suffer from several restrictions: Either they are limited to displaying atomistic data only (e.g. RasMol [149] and AtomEye [103]), that is, they do not provide any analysis functions giving insight into the processes of interest, or they are not powerful enough to handle larger datasets with millions of atoms (e.g. VMD [75]). For this reason, the development of a new visualization and analysis software was a precondition to enable the modeling efforts presented in this thesis, and –at the same time– contributes a valuable tool to the materials modeling community.

2.2 INTRODUCTION

The aim of this chapter is to introduce this new, freely available visualization software called Ovito. Being a single integrated application, it covers both the analysis and the visualization of large-scale atomistic datasets produced by molecular dynamics/statics and Monte-Carlo simulation codes. Its name is an acronym for *Open Visualization Tool*, emphasizing that this software has been designed with flexibility and extensibility in mind. The capabilities of Ovito go beyond those of established visualization software packages [149, 103, 75, 195].

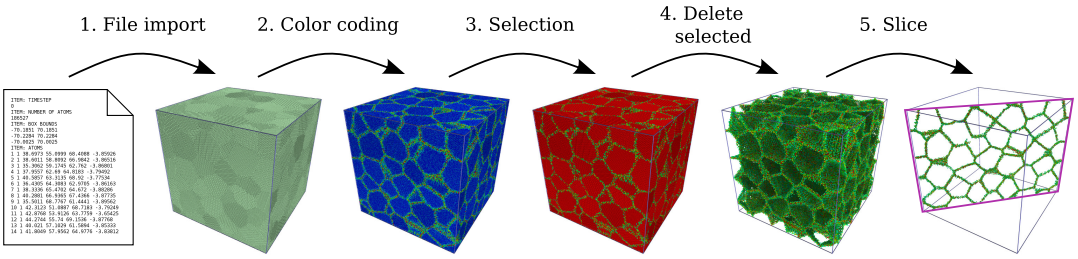

Figure 3: Illustration of the processing pipeline architecture of the OVITO visualization software. The labeled arrows denote the individual processing steps that are applied to the atomic data "flowing" through the processing pipeline. The images depict the intermediate states. The final data state is shown on screen, exported to a new data file, or fed into an external renderer such as POV-RAY [138] for publication-quality image output.

2.3 PROCESSING PIPELINE CONCEPT

User demands on visualization tools go far beyond just displaying a large number of spheres representing atoms in space. State-of-the art visualization packages should be flexible enough – and easy-to-use at the same time – to support the scientist in extracting the desired information from the simulation data in an interactive manner. As one of the first freely available programs, OVITO employs the powerful *data processing pipeline* concept to achieve this goal. The underlying idea is as follows: From a pool of available visualization and analysis functions (building blocks) the user builds up a sequence of processing steps, which is applied to the atomistic input data. Each processing step in this sequence modifies the data coming from the previous step. The result of this processing pipeline is finally shown on the screen. Figure 3 illustrates how a typical processing pipeline to visualize the grain boundaries of a nanocrystalline microstructure could look like in OVITO.

In contrast to a classical work-flow, the pipeline concept allows to alter the sequence of operations at any time, i.e., OVITO works in a *non-destructive* way with the input data. The user can change the parameters, the order of the processing steps, or the input data whenever needed and the system will immediately re-evaluate the processing steps and update the display in realtime. Through intelligent data caching and parallelization techniques, this all happens with a minimum usage of memory and processing resources.

The design of OVITO's data model allows the user to associate an arbitrary number of data fields with each atom. These fields include, for instance, the atomic coordinates, types, velocities, energies etc. The various processing steps introduced above operate on these data fields and/or calculate new

fields on output. Moreover, the user can – based on mathematical expressions – define custom scalar, vector or tensor data fields for each atom. In the current version, OVITO provides functions for the following tasks:

- Coloring atoms based on their type, selection state or any other per-atom value stored in the input file or computed in the processing pipeline
- Transformation of atoms and the simulation cell
- Visualization and calculation of displacement vectors from the differences of two states of the system
- Interactive slicing and cutting of atomic structures
- Display of periodic images and wrapping of atoms at periodic boundaries
- Selection of atoms based on user-definable criteria
- Calculation and display of atomic bonds
- Ambient lighting calculation and shading of atoms [171] for improved visualization of three-dimensional atomic structures
- Sophisticated analysis functions including
  - Common neighbor analysis [72]
  - Ackland-Jones analysis [4]
  - Cluster analysis
  - Coordination number calculation
  - Calculation of intrinsic and extrinsic atomic-level strain tensors (chapter 3 and Ref. [157])

2.4 ADDITIONAL FEATURES

Nowadays powerful graphics cards with high-performance 3d rendering capabilities have become available at low prices. Since this trend towards cheap graphics hardware is expected to continue, OVITO employs hardware-accelerated rendering based on the OpenGL standard to display a large number of atoms in realtime. Even with an entry-level graphics card, OVITO is able to display several millions of atoms smoothly by using state-of-the-art rendering techniques such as shader-programs directly executed on the processor of the graphics card (GPU).

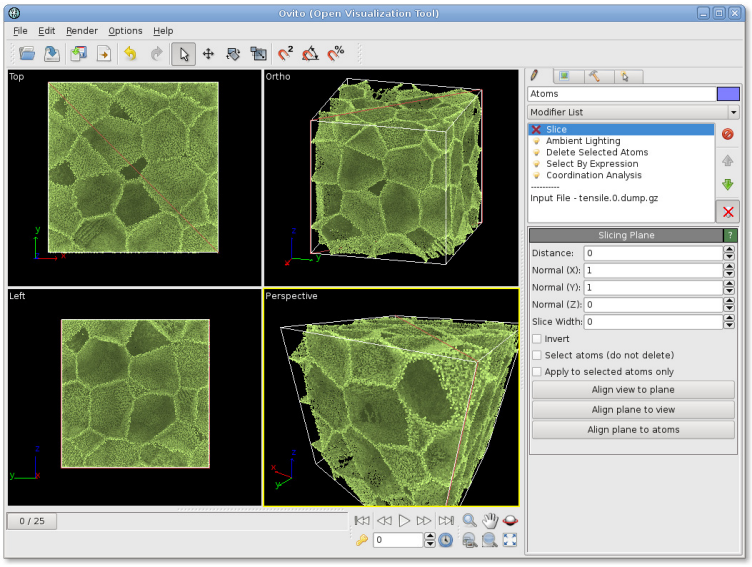

Figure 4: Screenshot of the main window of OVITO. The window is divided into four viewports, each displaying the atomic structure from different viewing directions. The panel on the right lets the user build up the processing pipeline and set the modification parameters.

OVITO can handle multi-timestep data files, making it possible to visualize a system's evolution with time. Every user operation can be undone, and almost every parameter can be animated, making it even possible to create fly-through movie animations of the atomic structures. Furthermore, OVITO is able display three-dimensional polygonal data and geometric shapes, allowing the user to enrich the atomic data with additional visual aids. For publication of simulation results, OVITO can produce high-quality output images, movies and POV-RAY scene files [138].

OVITO has been developed as a platform independent software that runs on all major operating systems, including Microsoft Windows and Linux. Figure 4 shows a screenshot of the application's main window. The program package has been designed with extensibility in mind, since it cannot be assumed that the requirements of each and every user can be met in the first place. Therefore the plug-in based architecture of OVITO enables the users to easily extend the software to their individual needs. Almost every aspect of OVITO can be extended by writing a small plug-in that seamlessly integrates into the program without making any changes to the core OVITO code base.

Data input and output is also part of the plug-in architecture. That is, the user can add import (and export) capabilities for the file format of his or her favorite atomistic simulation package to OVITO. In the current version, OVITO comes with import and export functions for the popular XYZ format

[1] and several file formats used by the simulation packages LAMMPS [139], IMD [164], and VASP [93].

OVITO provides a rich graphical user interface that allows the user to view and analyze his or her simulation results interactively. In addition to an interactive visualization, it is often necessary to process many simulation files in a row (batch processing). Therefore OVITO features a scripting interface based on the Python language [182]. Most of OVITO's functions can be invoked from Python scripts, which are run either within the graphical user interface or from the console. Automated loading, batch processing, and saving of simulation files allow to integrate OVITO into a user's custom tool chain.

2.5 CASE STUDY

In this section, some of OVITO's capabilities are demonstrated with a case study. Let us assume we want to study the microscopic deformation mechanisms in a nanocrystalline, face-centered cubic material. To this end, we have performed a molecular dynamics simulation of a tensile test experiment. The three-dimensional model structure being deformed is made up of 54 grains with an average size of 15 nm in a cubic simulation box with periodic boundary conditions. The simulated specimen is shown in figure 5a and contains approximately 6.2 million atoms, a system size that is handled by OVITO without difficulty on a standard PC. During the MD simulation the atomic positions have been periodically dumped to a sequence of output files.

The first thing to do is to make the grain boundaries of the bulk structure visible, as they play a crucial role for the plasticity of nanocrystalline materials. This can be achieved by performing a coordination analysis that determines the number of nearest neighbors of each atom. In the face-centered cubic structure, fully-coordinated lattice atoms in the interior of the grains have exactly 12 nearest neighbors. Atoms, in contrast, that form the grain boundaries are usually mis-coordinated, that is, their coordination number deviates from 12, which gives a simple criterion for filtering out grain boundary atoms.

To this end, the *Coordination Analysis* operator is applied to the input data. This operator takes one parameter, the nearest-neighbor cutoff distance, and calculates the number of bonds of each atom. The results are stored in a new integer data field named *Coordination*. All fully-coordinated atoms are now deleted by first selecting them with the *Select by Expression* operator. This operator takes a Boolean expression that is evaluated for each atom. This expression is set to be "Coordination==12". Then, all selected atoms

are removed by the *Delete Selected Atoms* operator. Note, that the atoms are not lost if this operator is applied. The delete operator only removes them from the final state of the system shown on the screen. We have the freedom to deactivate the delete operator again or to change any parameter of the preceding operators. OVITO will always re-evaluate the processing pipeline if needed.

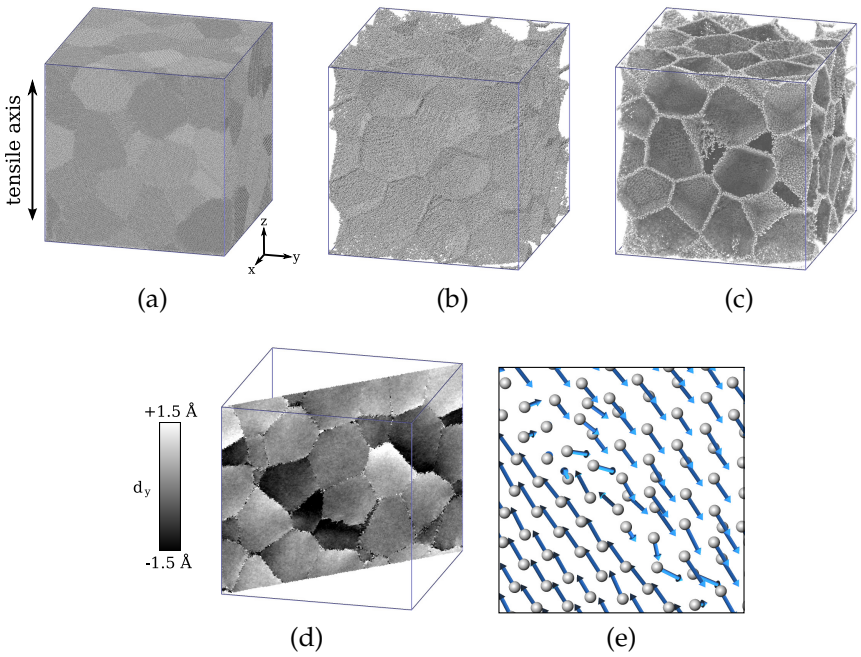

Figure 5: Case study of the analysis of a nanocrystalline structure at 3% tensile strain. The different stages of the study are discussed in the text.

Figure 5b shows the current state of the system after bulk crystalline atoms have been removed. The remaining mis-coordinated atoms form a grain boundary structure, but it is hardly visible due to the identical coloring of all atoms. This is a common visualization problem found for three-dimensional atomic structures. OVITO provides a remedy: The *Ambient Lighting* operator performs a lighting simulation to calculate a shading value for each atom, which makes the three-dimensional structure more apparent. Figure 5c displays the shaded grain boundaries. The screenshot (figure 4) shows OVITO's user interface at this point of the case study. The current operator sequence is displayed in the upper right part of the main window.

Next, we take a closer look at *grain boundary sliding*, a plastic deformation mechanism that is found in nanocrystalline materials in addition to classical dislocation glide. When grain boundary sliding occurs, whole grains slide over each other to accommodate the macroscopic strain imposed on the

sample. The sliding of complete grains at, say, 3% tensile strain, can be made visible by calculating the displacement vectors of each atom. A displacement vector is the difference between the current deformed position of an atom and its initial position in the unstrained state. The *Calculate Displacements* operator performs this calculation by taking the differences between two atomic data files. The displacements calculated by the operator are stored for each atom in a new vector data field named *Displacement*. Since we are only interested in the relative motion of neighboring grains, and not in displacements caused by the overall macroscopic strain, we first have to remove the macroscopic strain from the simulation box before calculating the displacement vectors. This is done by scaling the deformed simulation box, including all atomic positions, back to its initial shape using the *Affine Transformation* operator. Its key parameter is a 3 x 3 transformation matrix that is applied to all atomic positions.

The calculated displacement vectors are now ready for visualization. A first option is to color each atom according to one component of its displacement vector. If the vectors in one grain all point in the same direction, and in a neighboring grain they all point in some other direction, then sliding must have occurred at the grain boundary and will appear as a sharp contrast in the coloring of atoms. This can be seen in figure 5d where atoms have been shaded according to the Y component of the displacement vectors (tensile axis was Z). Here, the *Slice* operator was used also to cut out a slice from the structure, followed by the *Color Coding* operator, which assigns colors (or shades of gray) to each atom based on the values of an arbitrary atomic data field.

Alternatively, OVITO can directly visualize the displacement vectors as arrows. Figure 5e displays a close-up view of a grain boundary with arrows indicating the relative motion of atoms in adjacent grains.

2.6 AVAILABILITY

To make OVITO available to as many researchers as possible, it has been released as open source software under the GNU General Public License. Thus, OVITO can be used free of charge, everyone can contribute to the software, extend it to his own needs, and share newly developed plug-ins with other users. The C++ source code and binary packages of OVITO can be downloaded from the website *http://www.ovito.org/*.

2.7 SUMMARY

OVITO (The Open Visualization Tool) is a newly developed 3D visualization software designed for post-processing atomistic data obtained from molecular dynamics or Monte-Carlo simulations. Unique analysis, editing, and animation functions are integrated into its easy-to-use graphical user interface. The software consists of more than 110,000 lines of code and is easily extendable through a plug-in interface. It has been made available free of charge to satisfy the needs of the materials modeling community. Since its publication in late 2009, OVITO has been adopted by several researchers from all over the world. Most results presented in this thesis have been obtained with the analysis functions of OVITO, and most of the pictures have been created with this software. Furthermore, it served as a platform for the development of novel computational techniques like the dislocation analysis presented in chapter 4 and the lattice strain analysis, which is the subject of the following chapter.

3 MICROSTRAIN FIELDS IN NANOCRYSTALLINE METALS

3.1 INTRODUCTION

Diffraction techniques are widely used to characterize the microstructure and the defect structure of modern nanomaterials. While the relevant approaches have been known for many decades [89, 201, 97], not all details are well understood as yet. A prominent example is the nature and origin of the nonuniformity in the atomic displacement fields that give rise to what is known as microstrain broadening of powder diffraction lines. Microstrain broadening is ubiquitous at small grain size. It is most prominent in nanocrystalline materials with grain size, D, of around 30 nm and below. Here, irrespective of the synthesis route, the (root-mean-square) magnitude of the microstrain reaches values of up to 1% [110, 180]. This is much higher than in coarse-grained materials even if they have been heavily deformed. Materials with ultrafine grain size (D around 100-300 nm) also exhibit considerable microstrain, which is usually related to strain fields from dislocations [181]. Dislocations, however, appear not to control the microstrain broadening at the smaller grain sizes. In fact, simulated diffraction data of computer-generated samples without lattice dislocations were found to exhibit quantitatively the same microstrain broadening as experimental data [118]. This highlights conceivable alternative sources of microstrain at small grain size, for instance (i) strain fields due to stress concentrations at the many triple junctions, (ii) displacement fields near grain boundaries, and (iii) strain caused by compatibility constraints [205]. The main purpose of the following work is to elucidate the relative importance of these various sources of microstrain.

From a theoretical point of view, it has been established that the effect of atomic scale structural disorder on the powder diffraction pattern depends on the range of correlation of the atomic displacements from the periodic crystal lattice sites [97]. A change in the mean lattice parameter – corresponding to displacements with correlation length comparable to the crystal size – gives rise to a shift in the Bragg reflection positions. By contrast, more localized atomic displacements give rise to broadening or to a reduction in the area of Bragg reflections. Reflection broadening results if the amplitude of the displacement decays more slowly with distance, r, than $r^{-3/2}$. By contrast, displacements fields decaying as r^{-2} or faster lead to a Debye-Waller type

reduction in reflection area and an enhanced diffuse background. Finally, the discontinuous disruption of the lattice structure at grain boundaries implies that the distribution of interatomic spacings between pairs of atoms located in different crystallites does not contribute to the Bragg reflection intensity at all. Thus, obtaining information on the atomic disorder at grain boundaries in nanomaterials from diffraction data will typically require the computation of pair distribution functions by Fourier analysis of the full interference function [110].

Enhanced Debye-Waller factors at small grain size have been observed in some studies of nanocrystalline metals, based on direct analysis of x-ray diffraction patterns [45], the analysis of near-neighbor spacings in pair distribution functions [110], and on extended x-ray adsorption fine structure (EXAFS) data [16]. Yet, because of the comparative ease with which x-ray reflection broadening data can be obtained and analyzed, the data base for microstrain is much more extensive.

Virtual x-ray scattering experiments study diffraction patterns from computer-generated atomic configurations with the desired (e.g., nanocrystalline) microstructure, computed so as to include all relevant features of the experiment [117, 118, 41, 19]. Full atomic-scale structure information can thus be compared to the results of diffraction data analysis. Derlet et. al [41] infer a correlation between the diffraction features of deformed nanocrystalline samples and the presence of dislocations, whereas Markmann et al. find no evidence for such a correlation in as-prepared nanocrystalline samples [118].

Here, we study the origin of x-ray microstrain broadening in nanocrystalline Pd, generated via molecular dynamics (MD) simulation, by combining the virtual diffraction approach with a direct analysis of the atomic displacement fields. In doing so, we introduce a new method for calculating atomic level strain, which allows us to address the following questions:

(i) Does the microstrain inferred from the x-ray data analysis reflect real atomic disorder, or is it merely an artefact originating from the scattering data analysis?

(ii) What is the microscopic nature and origin of the displacement fields that cause the reflection broadening?

3.2 PROCEDURES

3.2.1 *Molecular dynamics simulation*

The MD-generated nanocrystalline samples studied here were obtained starting out with the atomic positions of the relaxed nanocrystalline Pd samples in Ref. [213]. The 16 grains in the simulation unit cell are bcc Wigner-

Seitz cells inscribed with fcc Pd crystal lattices. The grain size, specified as the equivalent-volume sphere diameter, assumed values of 4.6, 6.9, 9.2, 13.8 and 18.4 nm. Atomic coordinates of the original samples had been obtained by MD relaxation at 600 K using Foiles' EAM-potential for Pd [55]. A careful analysis of the structures confirmed that the grains are completely free of lattice dislocations. As will be discussed below, the analysis of atomic level strain is greatly simplified when thermal vibrations are removed. To this end, the structures were quenched to 0 K by firstly using a temperature controlled MD run (including volume relaxation) and subsequently using a conjugate gradient (CG) static minimization technique [140].

3.2.2 *Analysis of atomic level strain*

3.2.2.1 *Describing local material deformation*

The deformation gradient tensor $\mathbf{F}$ of continuum mechanics describes the local deformation in a point of a material. In the present context it serves as link between atomic level lattice deformations and the macroscopic strain measure. As will be described in the next paragraph, we start from calculating a per-atom deformation gradient for each lattice site in the microstructure. In order to obtain the maximum spatial resolution for the atomic deformation measure, we take only the atomic positions of nearest neighbors into account, i.e. only the first neighbor shell of the central atom determines its local deformation tensor. As mentioned above, thermal displacements have to be removed for such an analysis as they would show up as random local deformations in an instantaneous snapshot of the system.

Palladium has a face-centered cubic structure, but the analysis method presented here can easily be adapted to other crystal structures. In an fcc lattice the first neighbor shell comprises 12 atoms at a distance of $a_0/\sqrt{2}$ with a_0 being the equilibrium lattice constant. In an imaginary, axis-aligned, and $\langle 100 \rangle$ oriented reference lattice, the vectors connecting the nearest neighbor atoms with the central atom compose the $a_0/\sqrt{2} \cdot \langle 110 \rangle$ vector family, denoted by the set $\{\boldsymbol{X}_i\}$, $i = 1...12$.

Similarly, each fcc atom in the *deformed* crystal lattice is surrounded by 12 nearest neighbor atoms whose relative positions are given by the vectors $\{\boldsymbol{x}_j\}$, $j = 1...12$. It must be noted that the order of neighbor atoms in the deformed configuration is random in general. Therefore calculating the deformation gradient at an atomic site is a two-step process: (I) Every single neighbor atom j in the deformed state is assigned to a counterpart in the reference configuration, resulting in a remapping of the indices $j \rightarrow i$. (II) The deformation gradient $\mathbf{F}$ is then determined by a least-square fit such

that it transforms the reference vectors to the deformed vectors as exactly as possible, i.e.

$$\mathbf{F}\boldsymbol{X}_i \approx \boldsymbol{x}_i \quad \forall \quad i. \tag{3.1}$$

In other words the linear least square fit determines the 9 matrix elements of $\mathbf{F}$ such that the residual

$$\Pi = \sum_{i=1}^{12} |\mathbf{F}\boldsymbol{X}_i - \boldsymbol{x}_i|^2 \tag{3.2}$$

reaches its minimum. Note that the calculated $\mathbf{F}$ includes information on the affine part of the local lattice deformation and the absolute rotation of the crystal lattice. That is, our approach does not require any *a priori* knowledge of the crystallite orientations or the atomic displacement vectors as opposed to other atomic strain calculation methods [131, 101]. The described procedure has been implemented into our visualization and analysis software OVITO (section 2).

The procedure is only applied to those atoms in the sample that are of fcc-type according to the common neighbor analysis (CNA) method [72]. As nearest neighbor criterion for the CNA a cutoff radius $R_{cna} = 0.5 \cdot a_0 \cdot (1 + 1/\sqrt{2})$ is chosen, which lies halfway between the first and second neighbor shell. Our measure for the deformation gradient is ill-defined for all other atoms, and in particular for the grain boundary regions. These atoms are excluded from our analysis.

The lattice parameter of the reference material serves as the only input parameter for the analysis described before. Since the variation of the mean lattice parameter with grain size is negligebly small relative to the typical strain amplitude, we used the lattice parameter of the single crystal, which is a_0 =3.890 nm for the Foiles Pd-potential.

3.2.2.2 *Atomic strain measures*

In order to make a comparison with experimental microstrain data, a scalar measure of the local deformation tensor $\mathbf{F}$ is desirable. As the state of strain is, in general, anisotropic, adopting a hydrostatic strain measure – as in Ref. [41] – is not useful here. Instead, each of the three principal strains contributes to the peak broadening in a powder diffractogram. Therefore a (non-uniform) shear without volume change or corresponding pressure does contribute to peak broadening. We therefore introduce two different measures of deformation that will be used in our analysis.

The (Green) strain tensor, $\mathbf{E}$, is related to the deformation gradient via $\mathbf{E} = \frac{1}{2}\left(\mathbf{F}^T\mathbf{F} - \mathbf{1}\right)$. The three eigenvalues $\epsilon_1, \epsilon_2, \epsilon_3$ of the symmetric tensor $\mathbf{E}$ specify the relative variation $\Delta a/a_0$ of the lattice parameter in the principal

directions of the deformation. This set of three strain values represents our first measure for deformation. Since no preferred orientation can be specified, each of them is equally significant as a measure for the local strain. Therefore, the basis of our evaluation of the distribution of atomic level strain is the data set containing each of the three principal strain values for every single fcc-type atom, $3N$ strain values for a sample containing N lattice atoms.

Our second measure of local strain is chosen with an eye on visualizing the spatial variation of the lattice distortion, for instance in cross sections of the MD samples. Here, we find it useful to account for all principal values of the local strain in a single scalar parameter. Our measure for the *atomic distortion magnitude* is here calculated for each bulk atom according to

$$\delta = \left(\frac{\epsilon_1^2 + \epsilon_2^2 + \epsilon_3^2}{3} \right)^{1/2} \tag{3.3}$$

with ϵ_1, ϵ_2, ϵ_3 as defined above.

3.2.3 *Virtual diffractograms*

3.2.3.1 *Computation*

The computation of virtual x-ray powder diffractograms follows the procedures described in detail in Ref. [118]. In short, the autocorrelation function is calculated by counting all interatomic distances in the MD simulation cell. A sine transform yields the interference function. By multiplying with the atomic form factor and taking into account experimental features such as the K_α doublet, the polarisation and the absorption, x-ray diffraction patterns are calculated.

3.2.3.2 *Analysis*

The virtual diffractograms are analyzed adhering to the same procedures used for experimental powder diffraction data. Fits with Pseudo-Voigt functions supply full width at half maximum (FWHM) and integral breadth for each reflection, for Miller indices up to (333). A variant of the Williamson-Hall analysis is then applied to estimate the grain size and the microstrain, separately (see Ref. [118] for details).

In comparison to the integral breadths, the FWHM provide more robust data; in particular, they are less sensitive to contributions from the background intensity [96]. When analyzing broad peaks, as it is done here for Bragg reflections of microstructures with grain sizes of only about 10 nm, this carries even more weight. Therefore, all results shown here are obtained from the analysis of FWHM, not integral breadth data.

In the most simple conceptual picture, the microstrain line broadening in powder diffraction can be understood in terms of a set of microdomains with a distribution of lattice parameters. The line shape then follows from the lattice parameter distribution. In the absence of information on the functional form of the distribution, the following assumptions have been used [165]:

1. all local strain values are evenly distributed within an interval $[-\epsilon, +\epsilon]$ with ϵ being the global microstrain measure; or Âă
2. the local strain values follow a Gaussian distribution with ϵ, the root-mean-square of the distribution, taken as the global microstrain measure.

Based on one of these assumptions, the global microstrain value, ϵ, can be derived from the measured broadening of multiple diffraction peaks [165, 89]. Since we aim at comparison between real-space atomic level strain measures and the strain evaluated by x-ray analysis, we use the second of the two above assumptions, which is presumably the more realistic distribution function.

3.3 RESULTS

3.3.1 *Microstrain from virtual diffractograms*

The average grain sizes and microstrains as obtained from virtual diffractograms are essentially the same as in Ref. [118], where samples at 300 K were considered. Since in the present work samples are cooled to 0 K temperature, both parameters are slightly smaller as compared to the data given in the previous study. The dependence of microstrain on grain size is in very good quantitative agreement with experimental results for nanocrystalline metals. Figure 6 shows the virtual diffraction data for the microstrain as function of the (true) grain size of the present samples. We now inspect the atomistic strain distribution in comparison.

3.3.2 *Direct analysis of atomic level strain*

We shall first discuss the mean value of the atomic level strain ϵ. This value connects to the mean pressure within the crystallites. Thereby, it relates not to the microstrain but rather to a possible shift in the mean lattice parameter. The computation – by direct analysis of the atom coordinates – yields mean strains ranging from 0.01% to 0.05%. This agrees with the virtual diffraction measurements, which do not resolve a significant variation of the mean lattice parameter. The overall mean strain is therefore insignificant compared

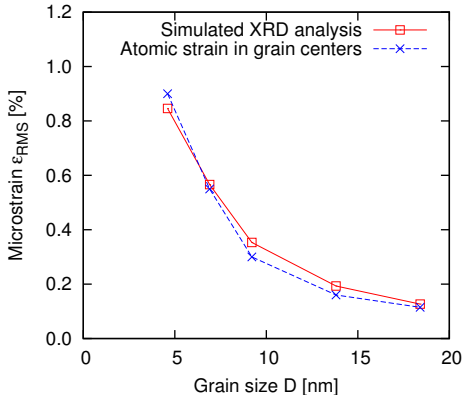

Figure 6: Microstrain in nanocrystalline samples as a function of grain size. The microstrain has been measured in two ways: (1) By means of a simulated x-ray diffraction analysis and (2) by direct calculation of the distortion from the atomic strain tensor in the center of the grains.

to the width of the local strain distribution as computed from diffraction and – as will become apparent below – from the atom coordinates.

Figure 7 shows the overall distribution of the values of the atomic level strain, ϵ, for samples with different grain sizes. For all samples we find a narrow central peak, a plateau at moderate strain values, and broad wings. Furthermore, the distribution widens with decreasing grain size.

Also shown in figure 7 are the local strain distributions inferred from the (virtual) x-ray microstrain measure. The graphs refer to both box-shaped and Gaussian distribution, as discussed in section 3.2.3.2. While the trend of increasing microstrain with decreasing grain size is confirmed, it is seen that the diffraction-based distributions consistently and significantly underestimate the breadth of the local strain distribution as computed from the atomistic data. This is not surprising, since the atomistic measure of microstrain lacks information on the correlation range of strain fields that determines whether the signature of distortion in diffraction is line broadening or line enhancement of the Debye-Waller parameter. To explore this issue we shall inspect maps of distortion in cross-sections of a given sample.

Figure 8a shows a map of distortion, δ, in a cross-section of a computer-generated sample ($D = 9.2\,\mathrm{nm}$). The map illustrates that the distortion is not uniformly distributed throughout the grains. Instead, most of the distortion arises from highly strained fringes around the grain boundaries.

For comparison, a measure of the atomic level stresses in the same part of the microstructure is shown in figure 8b. Atoms have here been colored according to the hydrostatic component of the atomic level stress tensor which was calculated from the interatomic forces. Even though the spatial distribution of the stress fields looks similiar to the strain fields in figure 8a, it must be noted that the relation between strains and stresses is highly nontrivial and nonlinear in the distorted grain boundary regions.

In order to examine the spatial microstrain distribution more quantitatively, the average distortion has been computed as a function of the distance, d_{GB},

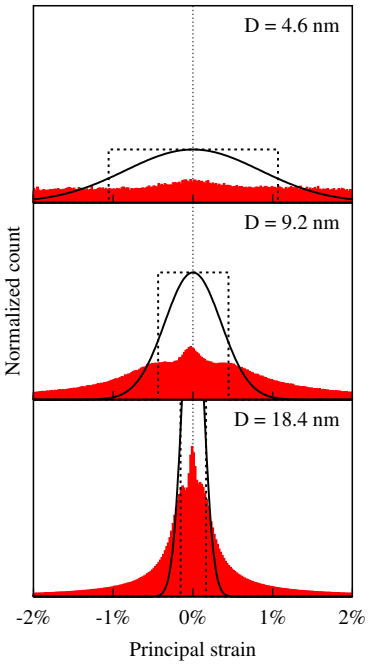

Figure 7: Overall distribution of the atomic strain values, ϵ, in the bulk material, excluding the grain boundaries, as derived from the real space analysis method. The distribution is shown for three sample structures with different grain sizes; all histograms are normalized. Box and Gaussian curves indicate the strain value distribution as it is normally assumed in the XRD analysis theory. The mean of all distributions is very close to zero, thus the mean lattice constant is not changed in the nanocrystalline material. This result is confirmed by the virtual diffraction calculations for the same structures.

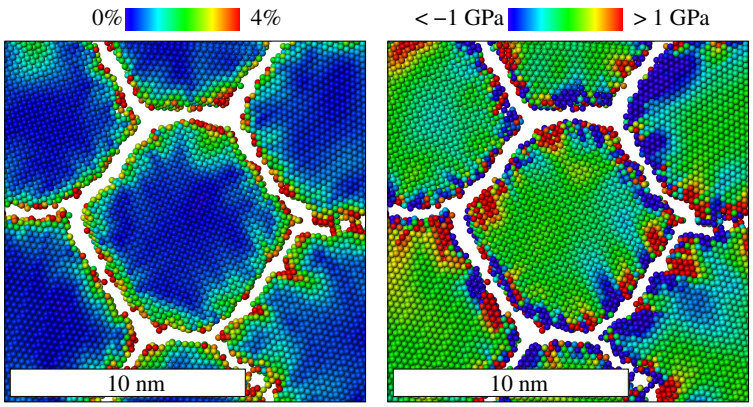

(a) Strain fields (b) Stress fields

Figure 8: Cross section of one of the nanocrystalline samples ($D = 9.2\,\mathrm{nm}$) showing the strain and stress fields in a typical grain. Only atoms in fcc configuration are shown. (a) atoms are colored according to their local distortion value δ (Eqn. 3.3); (b) atoms are colored according to their local hydrostatic stress component (positive stress means compression).

from the grain boundaries. In the following, the average distortion value $\overline{\delta}(d_{\mathrm{GB}})$ is defined as the mean of the distortions δ of all bulk atoms within a distance of $[d_{GB} - \Delta, d_{GB} + \Delta]$ to the nearest grain boundary. This requires to identify the closest grain boundary atom of every fcc-type bulk atom. In doing so, all non-fcc atoms are considered grain boundary atoms except the atoms adjacent to vacancies. For classification of the distances the bin size $\Delta = 0.025\,\mathrm{nm}$ has been used. Figure 9 displays the spatial distribution of distortions computed for samples of different grain size. The graphs end where d_{GB} reaches the largest possible distance from the grain boundaries. This maximum distance is usually less than half of the grain size because the grain shape is not perfectly spherical. Additionally, not all grains in each of the model structures have exactly the same size. The distortion values at the large distance tails of the curves constitute poor averages, representing only a few atoms in only the largest grains. This explains the scatter in the data corresponding to the last 0.5 nm in d_{GB}.

The data of figure 9 confirms that the distortion is very large near the grain boundaries, with strain values of more than 4%. Note that the strain level within the first 1.5 nm distance from the grain boundaries is nearly independent of the grain size. It is also seen that the strain decays rapidly towards the grain centers. Remarkably, even for the largest D the distortion does not drop to zero in the grain center. Instead, for the larger D samples, the graphs of distortion level off and reach nearly constant values, which are smaller for samples with larger grain size. Even more remarkable is the finding that this constant value agrees closely with the x-ray microstrain value of the respective sample, as indicated in the figure. As a counter-check we have included the data for $\overline{\delta}$ in the grain centers in the graph of x-ray microstrain versus grain size, figure 6 above. The comparison underlines the excellent agreement between the directly obtained distortion values in the grain centers and the x-ray results. Thereby, it also suggests that the x-ray microstrain is not sensitive to the local lattice distortion in the immediate vicinity of the grain boundaries.

The notion that the x-ray microstrain is governed by distortion in the grain interior rather than at grain boundaries is verified by the following procedure: A typical grain is isolated, here from the sample with $D = 18.4\,\mathrm{nm}$. Then the grain is subjected to the virtual diffraction data analysis, and the results are noted. After removing all atoms within a certain distance form the grain boundary, the procedure is repeated, while no atomic relaxation is performed at any point of this analysis. Figure 10 shows the results of this experiment, which confirm the previous observations: The diffraction microstrain value remains essentially constant, irrespective of whether or not the highly distorted grain boundary layer is taken into account. As a consistency check we verified that the diffraction grain size is reduced with

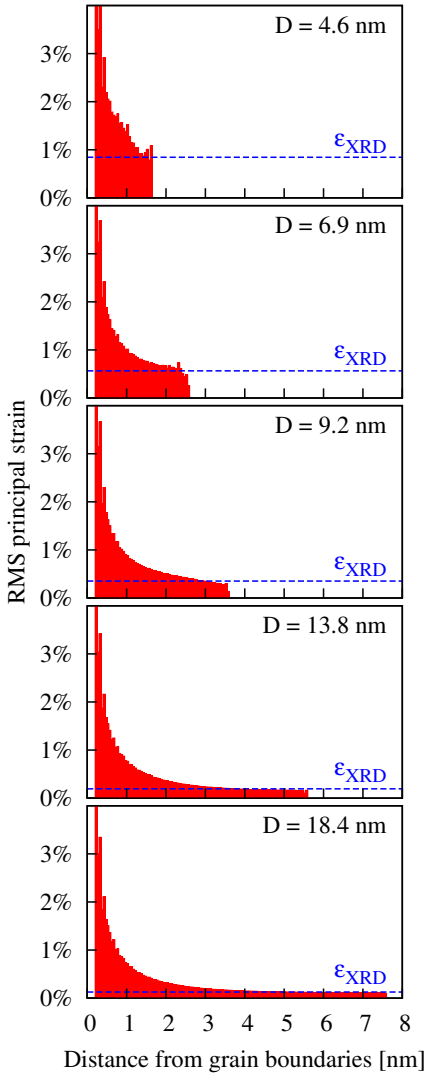

Figure 9: Average distortion $\overline{\delta}$ as a function of distance d_{GB} from the nearest grain boundary for five microstructures with different grain size D. High strain magnitudes are observed close to the grain boundaries, decaying towards the grain centers. Horizontal lines indicate the overall microstrain content obtained independently from simulated XRD measurements.

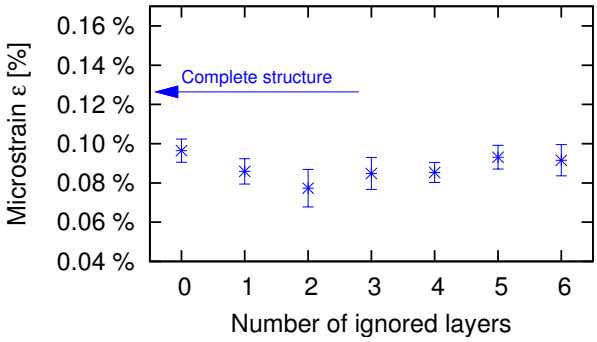

Figure 10: Measurements of intrinsic microstrain of a single grain using the virtual XRD method. The size of the isolated grain is successively reduced by peeling off atomic layers from the surface. The arrow indicates the measured value for the complete microstructure including all grains.

every atomic layer taken off the grain. To repeat, the result implies that the diffraction microstrain is not sensitive to the strain fields in the immediate vicinity of the grain boundaries.

3.4 DISCUSSION

We have studied nonuniform displacement fields within the crystal lattice regions of computer-generated nanocrystalline Pd by two independent techniques: The first emulates the procedures in the Williamson-Hall-type analysis of Bragg reflection line broadening in experimental x-ray powder diffraction data analysis by means of a virtual diffraction experiment. The second technique analyzes the local strain atom by atom, based on the atomic position coordinates. The microstrain computed in the virtual diffraction data analysis had previously been shown to agree quantitatively with experiments on nanocrystalline fcc metals prepared by various techniques [118]. Our analysis supplies the following results: The root-mean-square strain, averaged over all crystal atoms, is much larger than the diffraction microstrain. The value of the former is dominated by the large distortion in narrow fringes near the grain boundary plane; the magnitude of this local distortion at grain boundaries is essentially independent of the grain size. The distortion decays rapidly with distance from the boundary, and its mean value in the center of the grains is in excellent agreement with the x-ray microstrain. We shall now discuss the implications of these observations.

We start out by advertising the significant effect of the grain boundaries in nanocrystalline metals on the atomic displacements from the crystal lattice. In the crystal lattice regions near boundaries, the local displacements from the

lattice are much larger than the thermal displacements at room temperature, which exhibit a RMS amplitude of roughly 1 % of the interatomic spacing [110, 16]. This large deviation from crystalline order may be significant for the materials properties, for instance for the propensity for dislocation nucleation in plastic deformation. Even though experimental diffraction data testify to an unusually large microstrain in nanocrystalline metals, the diffraction microstrain is inappropriate to reveal this local lattice distortion near grain boundaries, which is even larger.

The failure of the diffraction microstrain data to detect local strain may be traced back to the correlation length argument exposed by Krivoglaz [97]: A slower than $r^{-3/2}$ decay of the displacement self correlation function is required for the displacements to manifest themselves in Bragg reflection broadening. It is therefore noteworthy that, within dislocation models of grain boundaries, the strain field decays exponentially with distance from the boundary plane (see, for instance, Ref. [166]). This suggests that the local disorder will manifest itself in an enhanced Debye-Waller parameter rather than in line broadening and apparent microstrain. Conversely, diffraction line broadening is poorly adopted to probe the strain fields from intrinsic grain boundary dislocations.

The finding that diffraction microstrain is representative of lattice strain in the interior of the crystallites far from the grain boundaries, points to an open question in understanding nanocrystalline metals: Which factors govern the magnitude of the intrinsic stresses and strains within grains in a polycrystal with very small grain size? As exposed in the introduction, the microstrain in severely deformed metals with grain size around 100 nm and above can be related to their lattice dislocation density [208, 178, 179]. After a careful check, the presence of lattice dislocations in the present samples can be ruled out. Thus, we conclude that attempts to infer a dislocation density from the microstrain value are bound to fail for nanocystalline samples with grain size as small as the present ones. By contrast, our results do not exclude extrinsic grain boundary dislocations as the origin of microstrain: Since such defects do not form periodic arrays, their strain fields are not exponentially screened, and can extend throughout the grains. The study, however, does not provide obvious evidence for the presence of extrinsic grain boundary dislocations. Equally compatible with our results are two alternative explanations, which relate the microstrain to intrinsic aspects of the microstructure of nanocrystalline solids: The first relates to strain fields from triple lines. These may be understood within the context of disclination models of nanocrystalline materials, and their range is expected to be comparable to the grain size [145].

The second intrinsic property of nanocrystalline materials is the strain resulting from compatibility constraints on the packing of crystalline objects.

Since the crystalline nature implies that the crystal dimensions are quantized via their integer number of lattice planes, elastic strains of the grains are required for a space-filling polycrystalline tessellation. It has been noted [205] that the required RMS strain values are in close agreement with those of diffraction microstrain, which in turn agree with the RMS strain found by our direct analysis in the centers of the present samples.

In conclusion, our study shows that atomic displacements which result inherently from the reduction of the grain size of a polycrystalline solid to the scale of 20 nm or below can be separated into (at least) two distinct types, with qualitatively different consequences for the scattering pattern. Local displacements near the grain boundaries are correlated over shorter distances, and they do not significantly affect the broadening of the Bragg reflections that underlies experimental diffraction microstrain data. This broadening arises, instead, from long-range correlated displacement fields that extend throughout the grains, and the microstrain value inferred from it provides a quantitative measure for the distortion far from the grain boundaries. The origin of this distortion is not understood. Our results do confirm, however, that large microstrain values can be obtained even when there are no lattice defects besides grain boundaries. This suggests that diffraction-based strategies for inferring the dislocation density in ultrafine-grained metals may not transfer well to truly nanocrystalline materials.

3.5 SUMMARY

The origin of microstrain broadening in x-ray diffraction patterns of nanocrystalline metals was investigated by comparing data obtained from virtual diffractograms and from direct analysis of computer-generated samples. A new method was introduced that allows to calculate the local deformation gradient for each lattice site in the microstructure from atomic coordinates obtained by molecular dynamics simulations. Our results reveal that microstrain broadening in undeformed samples cannot be attributed to lattice dislocations or strain fields near grain boundaries. The broadening arises, instead, from long-range correlated displacement fields that extend throughout the grains. The microstrain therefore provides a quantitative measure for distortions far from grain boundaries. This suggests that diffraction-based strategies for inferring the dislocation density in ultrafine-grained metals do not necessarily apply to nanocrystalline materials.

Part III

DISLOCATIONS IN NANOTWINNED METALS

4 DISLOCATION DETECTION METHODS

4.1 INTRODUCTION

Dislocations are line defects governing the mechanical properties of many crystalline materials. They make crystalline materials deform plastically at stresses well below the ideal shear strength of the defect-free crystal structure. Accordingly, materials can be strengthened by impeding the formation and motion of dislocations through obstacles, including solutes, precipitates and other dislocations acting as pinning points [68].

A detailed understanding of fundamental deformation processes carried by dislocations requires atomic scale resolution. That is why macroscopic and mesoscale modeling techniques like continuum-based theories [161] and discrete dislocation dynamics (DD) [22] cannot be applied in cases where the details of interatomic interactions in the dislocation cores or the nucleation of dislocations play an important role. At this point, *atomistic* simulation techniques like molecular dynamics (MD) are the methods of choice, since they directly capture the physics stemming from the discreteness of the atomic arrangements [143, 22].

Modern computers allow to simulate the trajectories of millions or even billions [3] of interacting atoms by simply integrating Newton's equations of motion (see section 1.3.1). The real challenge, however, is to process the vast amount of output data in order to identify physically important processes, like the formation and motion of defects that can occur in complex three-dimensional topologies.

Various techniques have been developed in the past to identify individual atoms in a simulation that are part of crystal defects. Their level of sophistication ranges from very simple (e.g. coordination number, atomic excess energy [21]) to elaborate (e.g. common neighbor analysis [72], centro-symmetry parameter [83], Ackland's bond-angle method [4]). These methods are more or less well suited for a visualization of the defect structures. None of these methods, however, is capable of determining the type of a crystal defect (dislocation, vacancy, grain boundary etc.) or any quantitative higher-level information like the Burgers vector of a dislocation.

Recently, a new scheme for measuring the macroscopic plastic slip due to dislocation activity in fcc materials has been described by Vo et al. [191], which is based on a slip vector analysis [224]. This method can be used to

determine the (approximate) total slip a crystalline material has undergone, but is not able to yield specific information on individual dislocation lines, e.g. their instantaneous shapes and lengths or the topology of the network they form.

Hartley and Mishin [65] have shown how the Nye tensor field can be derived from the discrete lattice distortions produced by an atomistically modeled dislocation. Then, by integrating the Nye tensor field over a certain area enclosing the dislocation core, they determined the Burgers vector of the dislocation with a good approximation. This approach, however, is far from a practical implementation that is able to deal with arbitrary dislocation configurations, line shapes and dislocation junctions.

The goal of the present work is to extend the existing atom-based analysis techniques towards a fully-automated detection and extraction of complete dislocation networks in crystalline materials. In this chapter we describe two newly developed methods that allow to detect dislocation lines in atomistic simulation data, to determine their Burgers vectors, and to transform them into a one-dimensional line representation in a fully automated way. The first method, the *on-the-fly dislocation detection algorithm* (ODDA), is designed for large-scale massively-parallel MD simulations of dislocation-based crystal plasticity. It performs an on-the-fly analysis of the atomic configurations during an MD simulation and can handle systems of arbitrary size. In the second part of this chapter we describe an alternative method, the *dislocation extraction algorithm* (DXA), that was designed to exactly capture the topology of a dislocation network, to resolve dislocation junctions with atomic scale resolution, and to extract other (non-dislocation) crystal defects from atomistic simulations.

4.2 ON-THE-FLY DISLOCATION DETECTION ALGORITHM (ODDA)

We start out from the most fundamental dislocation detection method, the *Burgers circuit test* [74], and apply it in the vicinity of atoms that are part of crystal defects. If the circuit encloses a dislocation, this yields two pieces of information: the Burgers vector of the dislocation and a rough estimate of its location in the crystal. Of course, there exists an almost infinite number of possible paths around each dislocation, all yielding the same Burgers vector. Therefore, we have to find the *shortest* Burgers circuit, because only it will give the most precise information on the core's location. Given this shortest circuit, its center of mass can be taken as an approximate point on the one-dimensional dislocation line. Several Burgers circuits on parallel crystal planes yield a chain of points along the core, from which we can eventually reconstruct a continuous line through the crystal. This curve is

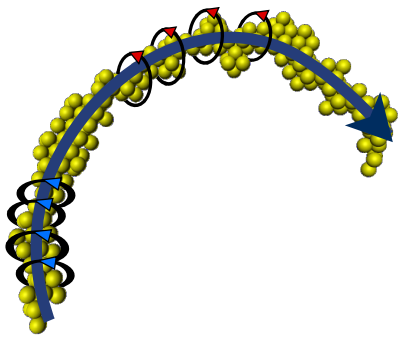

Figure 11: Schematic illustration of the dislocation detection method. A sequence of short Burgers circuits is traced around the dislocation core (yellow atoms) on adjacent crystal planes. The orientations of the planar Burgers circuits have been varied to cut the dislocation core irrespective of its local line direction. Each Burgers circuit yields one point on the dislocation line (the circuit's center of mass). Finally, these points are connected to a continuous one-dimensional line.

the desired higher-order representation of the dislocation. Figure 11 displays an illustration of this scheme.

What might sound like a trivial task turns out to be a very challenging algorithmic problem, because the following issues need to be addressed:

- The analysis should be able to deal with polycrystalline microstructures consisting of crystallites (grains) with different lattice orientations (which we don't know).
- A method needs to be developed that allows to identify the shortest Burgers circuit from a large number of equivalent circuits. Only then, we can exactly *locate* a dislocation in the crystal.
- Perfect, partial and twinning dislocations have to be distinguished.
- Going around a twinning dislocation, the Burgers circuit passes through the coherent twin boundary, at which the crystal orientation changes. Thus, the reference crystal for the Burgers test is no longer the perfect lattice, but instead a bicrystal containing a perfect twin boundary (see figure 12).
- Each Burgers circuit can yield only a single space point along the dislocation core. A method is required to reconstruct a continuous line from this set of initially independent dislocation points.
- Dislocation lines often form a dense network, and the algorithm must be able to deal with nodal points where three or more dislocation segments meet.
- For practical reasons, the algorithm has to be numerically efficient and should scale reasonably with increasing system sizes. Ideally,

the detection of dislocations should be performed on the fly during a running simulation.

In the following, a novel analysis method for atomistic simulations is presented that meets all requirements mentioned before. In contrast to the slip vector based approach discussed above, this analysis method operates solely on instantaneous snapshots of the atomic coordinates. That is, it is independent of the history of the crystal and can deal with successive dislocations moving on intersecting slip planes.

This section is organized as follows: In sub-section 4.2.1, the methodology and the principal processing steps employed for the extraction of dislocation lines are described. This main part is followed by a discussion of the limitations and the performance of the algorithm. We also demonstrate the capabilities with several examples in sub-section 4.2.4, and possible future applications of the new method are pointed out in the outlook section of this thesis (chapter 7.5).

4.2.1 *Description of the algorithm*

In the following, the principal processing step of the ODDA are described. Where appropriate, specific implementation details are given.

Step I: Local crystal structure analysis

In the initial step, the common neighbor analysis (CNA) method [72] is used to assign a local crystallinity class to each atom. Since the current version of the dislocation detection method is aiming at dislocations in face-centered cubic materials, it is sufficient to discriminate between fcc, hcp and disordered atoms. The third class comprises atoms that do not belong to any of the first two classes. The correct identification of crystalline fcc atoms is required to map them to lattice sites in a perfect reference lattice, performed in step II. The disordered atoms indicate the presence of crystal lattice defects. In addition to dislocations, this includes all sorts of defects like vacancies, grain boundaries, or free surfaces. Nevertheless, the early identification of disordered atoms gives a first hint on where potentially dislocation cores are located and narrows down the regions to be covered by the Burgers circuit search carried out in step V.

The identification of hcp atoms is necessary to locate twin boundaries and stacking faults found inbetween leading and trailing partials. An additional in-depth analysis of these atoms is performed in step III.

We favor the common neighbor analysis over other methods like the centro-symmetry parameter [83] or the bond-angle analysis of Ackland and Jones

[4] because of its strict criteria for the identification of fcc and hcp atoms. In step II, the nearest neighbors of crystalline atoms will have to be mapped to a reference lattice. For this reason, the number of neighbors must be exactly 12 for each fcc and hcp atom, and it must be ensured that the mapping is not ambiguous.

Step II: Orientation calculation and cluster analysis

In the context of our algorithm, a Burgers circuit is a closed path over nearest neighbor bonds in the dislocated crystal. While traversing such a path, the same sequence of steps must be made in a dislocation-free reference lattice to calculate the Burgers vector. To this end, we need to determine the corresponding lattice vector in the imaginary reference crystal for each nearest-neighbor bond in the dislocated crystal.

The CNA already guarantees that every atom identified as fcc has exactly 12 nearest neighbors in the dislocated crystal. That is, we only have to map each neighbor to one of the 12 lattice vectors, $\frac{1}{2}[110]$, $\frac{1}{2}[\bar{1}10]$ etc. The dislocated crystal, however, has an arbitrary lattice orientation and the mapping to the reference lattice is not unique due to the cubic crystal symmetry.

On a per-atom basis, we express the orientation relationship between the dislocated lattice and the imaginary reference lattice as an atomistic deformation gradient tensor that we determine for each lattice site. Let $\Delta\boldsymbol{x}^{(k)} = \boldsymbol{x}^{(k)} - \boldsymbol{x}$ denote the bond vector in world space pointing from an fcc atom at position $\boldsymbol{x}$ to its neighbor atoms $k = 1...12$. Accordingly, let $\Delta\boldsymbol{X}^{(k)}$ denote the corresponding nearest-neighbor vectors in Bravais lattice space. Then a deformation gradient tensor, $\mathbf{F}$, can be defined that transforms Bravais lattice vectors to world space vectors:

$$\mathbf{F}\Delta\boldsymbol{X}^{(k)} = \Delta\boldsymbol{x}^{(k)} \quad \forall \quad k. \tag{4.1}$$

The tensor $\mathbf{F}$ is determined for each atomic site using a linear least-square fit:

$$\mathbf{F} = \mathbf{W} * \mathbf{V}^{-1} \tag{4.2}$$

with

$$W_{ij} \equiv \sum_{k}^{12} x_i^{(k)} X_j^{(k)} \quad \text{and} \quad V_{ij} \equiv \sum_{k}^{12} X_i^{(k)} X_j^{(k)} \tag{4.3}$$

Equation 4.2 leads to an approximate deformation tensor that describes the local lattice orientation and elastic strain in the vicinity of the atomic site in an optimal sense. Our procedure is similar to the one described in [222], with

the extension that an initial state of the atomistic system is not required for the calculation. Instead, we always assume the perfect, axis-aligned crystal lattice to be the reference state. This makes our analysis independent of the history of the dislocated crystal and we can simply process arbitrary snapshots of the dislocated crystal without the need to explicitly define its initial, dislocation-free state.

Due to the space group symmetries of the fcc lattice, the transformation from the reference lattice to the rotated lattice is not unique. At least we have to make sure that, when calculating the atomic **F** tensors, they are all aligned to the same orientation. This can best be done by starting the calculation at an arbitrary atom and then recursively processing all its neighbors, their respective neighbors, and so on, until no more crystalline atoms can be reached. All atoms processed so far form a *cluster* (grain) of connected crystalline atoms, all having a similar local lattice orientation. More grains are found by repeatedly invoking the algorithm for remaining crystalline atoms that have not been visited yet.

Note that the deformation gradient calculated here is not evaluated with respect to lattice deformations (as it was done in chapter 3). It will only serve as an efficient way to translate atom-to-atom steps on the reference lattice to corresponding steps in world space and vice versa later in the Burgers circuit test. Thus, we only use the rotational information contained in the tensor to determine the orientation of the crystal with respect to an imaginary, axis-aligned reference lattice.

Step III: Identification of stacking faults and twin boundaries

Intrinsic stacking faults (ISF) and coherent twin boundaries (TB) are important planar defects in fcc crystals. The detection of Shockley partial dislocations requires the correct identification of ISFs, which are connected to Shockley partials. Thus, a Burgers circuit enclosing a single Shockley partial has to pass through its adjacent ISF once. Coherent twin boundaries, in contrast, are glide planes for so-called twinning dislocations. A Burgers circuit enclosing a twinning partial must therefore pass through the TB at least twice.

Both types of planar defects are formed by layers of hexagonal close packed (hcp) atoms parallel to a $\{111\}$ plane of the fcc matrix. A single layer of hcp atoms is characteristic for a TB (see figure 12), whereas a double layer is a well-defined criterion for an ISF (see figure 13 for an example).

The CNA did already identify all atoms with a local hcp coordination structure. The goal of this algorithm step is to classify these hcp atoms according to the planar defect they form (that is, ISF, TB, or none of both).

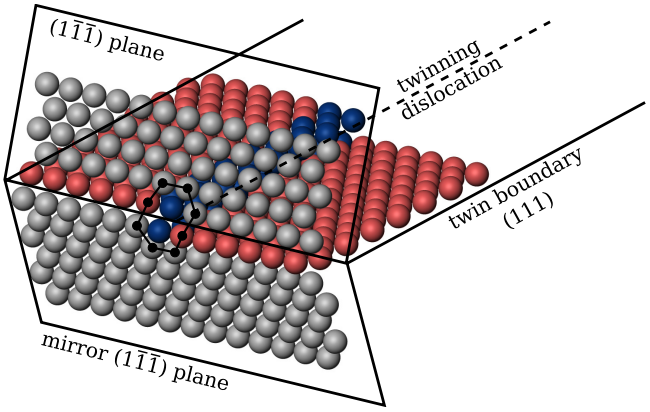

Figure 12: A twinning partial dislocation gliding on a coherent twin boundary. The dislocation core is formed by disordered atoms (dark blue). The twin boundary, formed by red atoms with hcp coordination, is parallel to the (111) plane shared by both crystal lattices above and below the boundary. Two atomic fcc layers in the $(1\overline{11})$ planes of the matrix and twinned crystal above and below the twin boundary are also shown (gray atoms). The Burgers circuit is traced around the dislocation core in these two planes.

This is achieved by first identifying the basal plane of each hcp atom, that is, we determine the six nearest neighbors in the $\{111\}$ plane perpendicular to the hcp c-axis. Then, the CNA structure types of the remaining six neighbors above and below the basal plane are examined. In the case of an ISF we have a double layer of hcp atoms, thus, three atoms on one side of the basal plane are also of the hcp type. In contrast, for a TB we find only fcc type atoms on both sides of the boundary plane.

The classification of hcp atoms as being either part of ISFs or TBs is a necessary prerequisite for the dislocation analysis. But it also provides valuable information with a physical meaning: It enables us to measure the stacking fault density and twin boundary density in the crystal separately. To our knowledge, previous simulation studies always relied on the raw number of hcp atoms to estimate the *total* area of planar faults in fcc crystals.

Step IV: Identification of atoms close to dislocation cores

As described above, we are only interested in Burgers circuits that are tightly wrapped around dislocation cores to determine their location as exact as possible. Thus, it would not make sense to trace any Burgers circuits through bulk crystalline material far away from the disordered cores. To avoid this

from the start, we stick to fcc atoms that are direct neighbors of disordered atoms when tracing the circuits.

This rule speeds up the Burgers circuit search considerably. By excluding crystalline atoms from the search procedure that are completely surrounded by other crystalline atoms, the number of possible circuits through the crystal is reduced to a manageable set. To further refine this approach, we determine for each of the four $\{111\}$ planes separately whether an fcc atom is adjacent to a disordered atom in that plane.

Step V: Burgers circuit search

This processing step is the heart of the dislocation detection algorithm. It determines the actual Burgers vectors of dislocations. The search is performed independently for each $\{111\}$ plane, i.e., only planar Burgers circuits are traced, and this, in turn, is repeated for each crystal cluster identified in step II. One exception from this rule are twin boundaries: Here, the Burgers circuit traversal switches to the mirror $\{111\}$ plane in a well-defined manner when it crosses the twin boundary, i.e., the resulting Burgers circuits are non-planar. Performing the search on at least three different sets of lattice planes (here, we use the four $\{111\}$ in the fcc crystal) is necessary to ensure that all dislocations, irrespective of their orientation, are found.

The Burgers circuit search is a two-step process. During the first phase, a nearest-neighbor graph is generated from all crystalline atoms surrounding the defect core. In the second phase, all *elementary circuits* in this nearest-neighbor graph are determined, and it is checked for each circuit found whether it is closed when being translated to the perfect reference lattice, i.e., this is the actual Burgers test.

Generation of the nearest-neighbor graph:

For each $\{111\}$ crystal plane, we generate a planar graph from crystalline atoms surrounding the defect cores. Such a *nearest-neighbor graph* is an abstract representation of the atomic adjacencies in the crystal. Each graph node represents one atom, and each edge between nodes indicates that the two corresponding atoms are nearest neighbors in the crystal. We include only atoms in the graph that are: (1) all in the same crystal plane and (2) are a nearest neighbor of at least one disordered atom (see last step). The generation of this graph is described next.

For any given $\{111\}$ plane, the algorithm starts at an arbitrary crystalline atom in that plane being adjacent to a crystal defect and assigns it the lattice coordinates $(0, 0, 0)$. From here, the algorithm visits all neighboring atoms in a recursive manner using a *breadth-first* search scheme. Every time a step

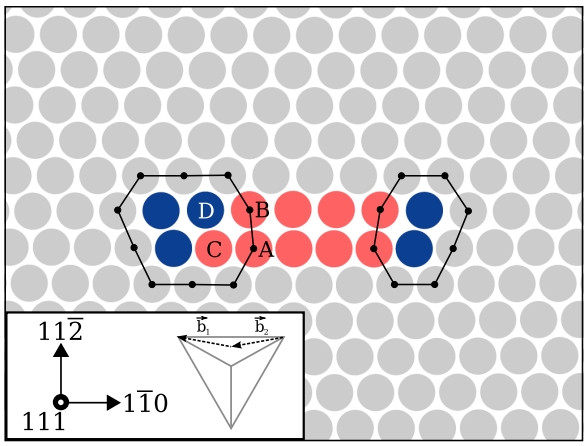

Figure 13: A dissociated dislocation ($a/2[\bar{1}10](1\bar{1}\bar{1}$)) consisting of two Shockley partials and an intrinsic stacking fault (ISF). Only a single layer of atoms, parallel to the (111) plane, is shown. Disordered atoms, as identified by the common neighbor analysis, are shown in dark blue. Stacking fault atoms with hcp coordination are shown in red. They form a double layer, which is characteristic for an ISF. The disordered atoms form the cores of the two dislocation lines. Their respective Burgers vectors are determined by tracing Burgers circuits around the cores in the (111) plane as indicated by the two paths. The step from site A to site B corresponds to a partial ($\boldsymbol{b}_1 = a/6[\bar{1}12]$) vector in the perfect reference lattice. Going from site C to the opposite layer is not possible because the passage is blocked by atom D not being identified as an hcp atom. And since atoms C and B are not direct nearest neighbors the tracing algorithm needs to extend the Burgers circuit to site A, where it can be continued from site B on to the other side of the stacking fault.

to a new atom is made, it is translated into a corresponding vector in the perfect reference lattice. This gives us the new lattice coordinates, which we assign to the new atom. One by one, all atoms are mapped to the reference lattice while being added to the nearest-neighbor graph. At some point, the recursive algorithm will eventually arrive at an atom that has already been visited before. If the newly calculated lattice coordinates differ from the previous coordinates already stored with the atom then a non-closing Burgers circuit has been found. In this case, the breadth-first search stops at the current atom, but the search is continued at all other atomic sites that are still on the search stack. The algorithm comes to an end if no more atoms can be added to the graph.

During this circuit search phase, a few additional traversal rules are required to ensure that only planar Burgers circuits are generated and ISFs and

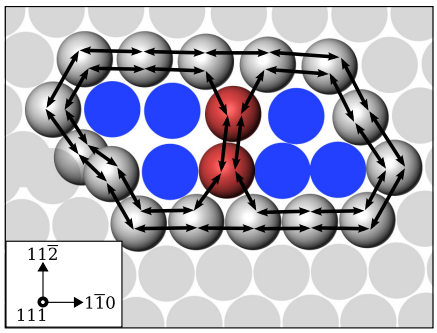

Figure 14: Cross-section of a dislocation in an fcc crystal that dissociated into two Shockley partials. The two dislocation cores (dark blue atoms) are separated by only two hcp atoms (red) that form a very narrow stacking fault. A nearest-neighbor graph has been generated from all atoms that are direct neighbors of the disordered core atoms. As indicated by the arrows the graph contains three elementary circuits, each yielding a different non-null Burgers vector.

TBs are correctly traversed. These rules control the stepping from an atom to one of its neighbors and are based on the classification of both atoms:

FCC $\rightarrow$ FCC This move is performed only if the destination atom is located in the current $\{111\}$ plane to ensure the generation of planar Burgers circuits.

FCC $\rightarrow$ HCP (ONLY ISF AND TB ATOMS) Accepted only if the hcp atom is in the current $\{111\}$ plane.

HCP $\rightarrow$ FCC Accepted only if the fcc atom is in the current $\{111\}$ plane.

ISF ATOM $\rightarrow$ HCP Accepted only if the destination atom is in the opposite hcp layer of the ISF (this move corresponds to a $a/6$ $<112>$ lattice vector). Steps parallel to the hcp basal plane are not allowed with the exception of the destination atom belonging to another ISF (not parallel to the ISF of the source atom).

TB ATOM $\rightarrow$ HCP Never allowed.

These rules are to guarantee that we build a planar nearest-neighbor graph that contains all possible paths around a crystal defect. If two dislocation cores are very close to each other then it might happen that the nearest-neighbor graph encloses both cores (see figure 14), that is, the graph will contain multiple Burgers circuits with different Burgers vectors. This issue will be resolved in the following step.

Enumeration of elementary circuits:

Based on the nearest-neighbor graph obtained in the last step, we use a backtracking algorithm [172] to enumerate all its *elementary circuits*. An elementary circuit is defined as a sequence of adjacent atoms that contains no atom twice with the exception that its first and last vertices are identical. We then calculate the Burgers vector of each elementary circuit by summing up all lattice vectors contained in the atom-to-atom path. A non-null Burgers vector indicates that the circuit encloses a dislocation core.

Unless a dislocation is embedded in an infinite crystal, the presented algorithm will always generate two Burgers circuits enclosing that dislocation: One that is tightly wrapped around the core and a second one that runs along the outer boundaries of the crystal. This is illustrated by the schematic crystal in figure 15. The outer Burgers circuit is a consequence of the CNA's inability to distinguish surface atoms from dislocation core atoms. The Burgers search algorithm simply tries to generate a circuit around all types of non-perfect atoms, not knowing whether the circuit encloses the defect or the other way around.

Both Burgers circuits in figure 15 are equivalent. But we are, of course, only interested in the circuit that is tightly wrapped around the dislocation core. All others can be sorted out by applying the following criterion: A Burgers circuit is considered too wide if its planar projection encloses at least one fcc atom not being part of the path itself. To determine whether there is such an atom, all in-plane fcc nearest neighbors of all atoms forming the circuit are tested. A planar point-in-polygon test [63] is used to check whether an atom (projected onto the circuit plane) is located inside or outside of the polygonal path. Point-in-polygon tests, however, are expensive (the total computational cost scales quadratically with the length of the circuit). That is why we use an additional criterion for early rejection of Burgers circuits that are unlikely to be tight circuits: If the length of the circuit (measured by the number of atoms) exceeds a threshold of 20 atoms then the circuit is skipped right away.

For each detected and accepted Burgers circuit, a co-called *dislocation point* with the following information fields is recorded:

- The Burgers vector in world space as well as in local lattice space.
- The center of mass of the circuit. It represents a point on the dislocation line (see figure 18b).
- The normal vector of the Burgers circuit plane. It is required to establish a unique relationship between the Burgers vector and the line direction vector computed later.

It is not necessary to store the full circuit paths.

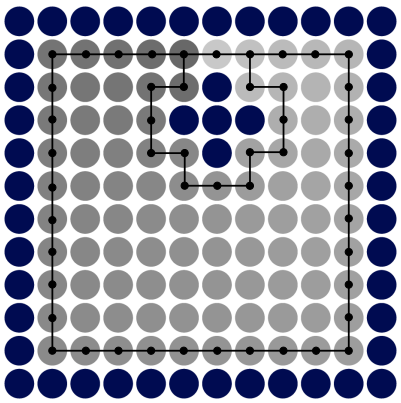

Figure 15: Schematic cross-section of a screw dislocation close to the surface of a square-shaped crystal. The line direction is perpendicular to the image plane and the crystal is bounded by free surfaces. Disordered atoms (belonging to the dislocation core and the surfaces) are shown in dark blue whereas bulk crystalline atoms are shaded in gray to indicate the elastic displacements around the screw dislocation. The two Burgers circuits found by the detection algorithm have been sketched in. Only the short circuit tightly wrapped around the five core atoms gives exact information on the location of the dislocation line. The outer path along the surfaces must be rejected as described in the text.

Step VI: Tracing of dislocation lines

The dislocation points recorded in the last step form a so-called *point cloud*, i.e., an unstructured set of points in space. Several techniques have been developed in the research field of computer graphics for reconstructing higher-dimensional geometric objects from such point clouds [109, 108, 216, 199]. They are able to construct continuous lines from unordered and disturbed point sets, but are also rather complex, hard to implement, or pose special requirements on the input point sets. Therefore, we decided to develop our own simple scheme to connect the dislocation points with a continuous line.

First, we divide the set of dislocation points into subsets of points with equal Burgers vector (ignoring the sign), since only points with the same Burgers vector can form one continuous dislocation segment. Then, starting at an arbitrary dislocation point, a local line tangent is estimated from the distribution of nearby points within a cutoff radius. This line tangent is computed from a *principal component analysis* (PCA) [79] of the local point cloud, i.e., from the major axis of an ellipsoid that is fitted to the nearby points.

Given the starting point and the tangent vector, the complete line can be found by integrating the tangent vector along the line. During the integration, the local tangent vector is constantly updated by recomputing the PCA for

the surrounding point cloud. The integration stops when no more new points are within the cutoff radius and the line end has been reached. Finally, the procedure is repeated in the reverse direction to find the opposite end of the dislocation line.

Step VII: Removal of extra dislocation lines

If two dislocation lines are close to each other, it can happen that three Burgers circuits are found: the two Burgers circuits enclosing each of the dislocation lines and a third circuits that encloses both dislocations. This frequently happens in some fcc materials when the two Shockley partials of a dissociated dislocation almost touch each other (see figure 14). We filter out the unwanted third dislocation segment by searching for pairs of dislocation segments in its vicinity. If a pair of two opposite dislocation segments can be found and their Burgers vector sum equals the Burgers vector of the central segment then the central segment can safely be removed.

Step VIII: Joining dislocation lines

Dislocation lines usually form a network, and the Burgers vector is conserved along the individual line segments. When several dislocations merge at a node, the sum of their Burgers vectors must be zero. This so-called Burgers vector conservation rule can be used to reconstruct the nodal points, which the basic Burgers search algorithm presented so far cannot deliver by itself.

The goal of this last processing step is to find all sets of dislocation line ends that (i) are within a given threshold distance to each other and (ii) whose Burgers vector sum is zero. We use a binary tree approach to solve this algorithmic problem efficiently. The line ends form the leafs of the binary tree. A parent node is created for each pair of points being closer to each other than a given threshold distance. Higher levels in the hierarchy are formed by merging more and more adjacent tree nodes. With each binary tree node the sum of the Burgers vectors of its children is stored. Tree nodes with a null Burgers vector are candidates for nodal points. A distance sum criterion is used to rank those candidate nodal points that are connected to the same dislocation line ends. The candidate point for which the distance sum is smallest, is finally taken as an actual nodal point. Additional line segments are then created to connect each line end to this nodal point.

4.2.2 *Limitations*

The Burgers definition of dislocations is independent of the underlying crystal structure accommodating them. To some extent, however, the circuit tracing part of the detection algorithm must be tailored to the structure of the host crystal containing the dislocations. Our current implementation of the algorithm is targeted at face-centered cubic materials. But in principal, the method can be extended towards other crystal structures by adapting those parts of the algorithm concerned with generating paths through the crystal lattice and mapping atomic positions to reference lattice sites.

Since the Burgers circuits generated by our algorithm are always planar (i.e., they run in a continuous crystal plane), only dislocation defects up to a certain Burgers vector length can be detected. Loosely said, the two dangling ends of a planar Burgers circuit will no longer find each other when the screw component of the Burgers vector perpendicular to the {111} plane exceeds two lattice plane spacings. Thus, exotic defects with an exceptionally large Burgers vector (e.g. several equally signed dislocations in one place with overlapping cores) remain undetected. Such defects are usually extended in all three spatial directions and representing them with a single one-dimensional line is questionable in any case.

4.2.3 *Implementation and performance*

We have integrated the detection algorithm described above into the molecular dynamics code LAMMPS [139]. Thus, the tracing of dislocation lines is done on the fly during a molecular dynamics simulation. To enable large-scale simulations, we parallelized the algorithm based on the spatial decomposition technique used by LAMMPS itself. The performance of our implementation allows us to analyze the dislocation structures at a high temporal resolution. To give an example: For a 70 million atom simulation (figure 17) containing a dense network of several thousands of dislocation segments, the MD simulation time (excluding any file output) increases by only 15% when the Burgers vector analysis (including the common neighbor analysis) is being performed every 50 timesteps. As an additional advantage, the amount of data storage required for the dislocation structure is more than a thousand times smaller than the corresponding fully atomistic simulation output, if it would be written at the same time intervals.

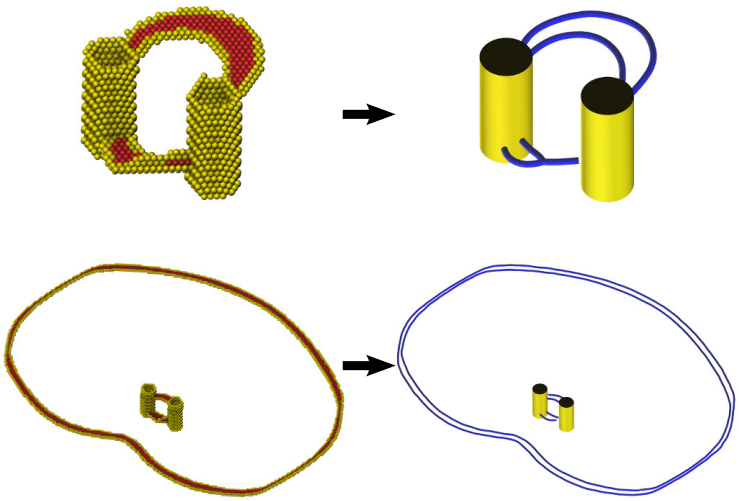

Figure 16: Molecular dynamics simulation of a Frank-Read dislocation source in fcc aluminum. The dislocation lines have been pinned by two cylindrical pores. The upper row of images shows an early state of the Frank-Read source. The lower two images show the source after it has generated a single dislocation loop. The atomistic system (left images) is displayed in comparison with the analysis output, the vectorized dislocation lines (right images).

4.2.4 *Examples*

To demonstrate the capabilities of the ODDA, we have performed two molecular dynamics simulations that involve dislocation activity.

As a first simple example, we applied the ODDA to the simulation of a single Frank-Read dislocation source in Al (modeled with an EAM potential [49]) as shown in figure 16. The simulation setup is similar to the one described in Ref. [39], except for the fact that the dislocations have been pinned more effectively by two cylindrical pores. The dislocation detection algorithm exactly tracks the dislocation lines as they bow out and recombine to form a closed loop.

To demonstrate the ability to extract large networks of dislocations, we performed a large-scale failure simulation of a cracked single crystal, following the example of the first one-billion atom MD simulation by Abraham et al. [3]. We reduced the simulation size to 70 million atoms for this demonstration, though, the dislocation detection algorithm can scale to larger systems. Figure 17 shows a sequence of snapshots of this MD simulation. The rapid nucleation of dislocations at the notches eventually leads to a very dense network of dislocations after the two loop fronts interpenetrate (figure 18).

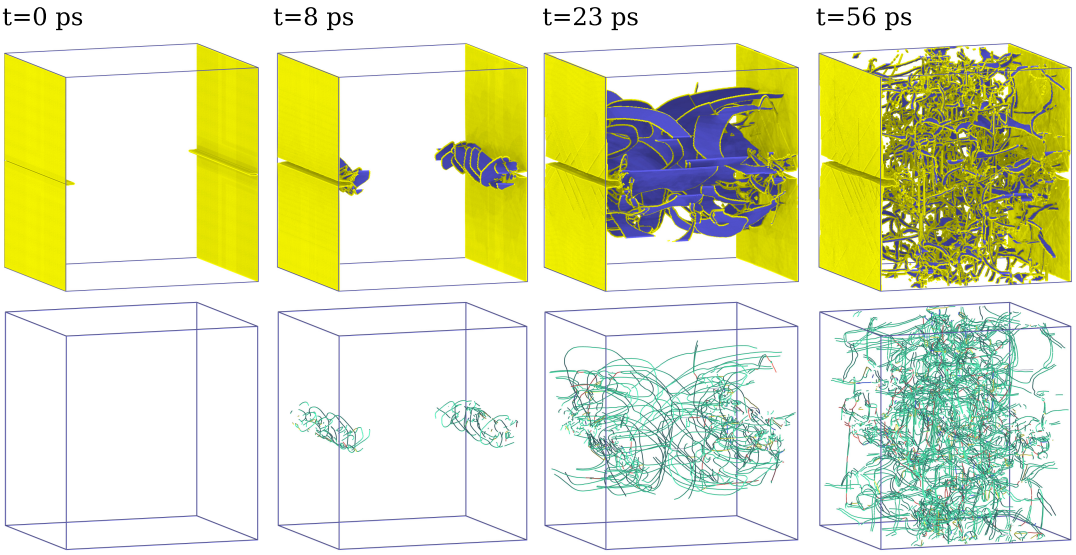

Figure 17: Large-scale simulation of the failure of a cracked fcc aluminum single crystal under tension. The system contains 70 million atoms. The setup is similiar to the one-billion atom failure simulation described in [3]. Two notches on opposing surfaces have been introduced to generate dislocations loops expanding into the bulk. A tensile strain of 4% was applied in the vertical direction to initiate the dislocation nucleation. Upper images show the disturbed atoms of the atomistic system. Lower pictures display the extracted dislocation lines. Line colors denote different Burgers vector families. The dislocation analysis was performed on-the-fly every 50 timesteps during the MD simulation. A quantitative analysis of the resulting dislocation network is presented in figure 19.

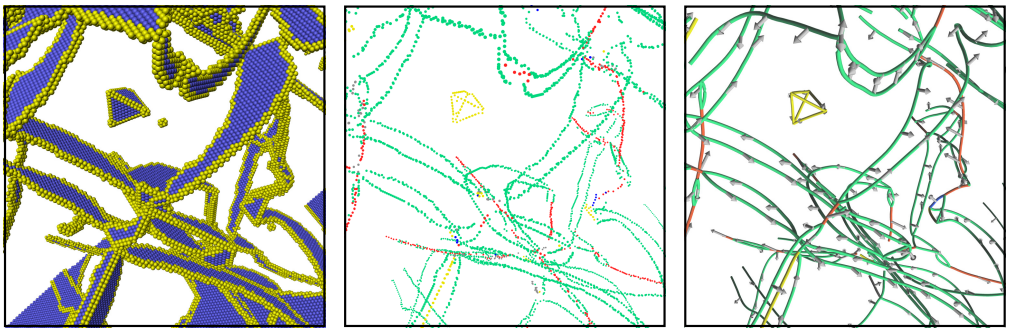

(a) (b) (c)

Figure 18: Close-up view of the dislocation network found in the simulation shown in figure 17. (a) Atomistic system with fcc atoms removed. The yellow, disordered atoms form dislocation cores, blue hcp atoms form stacking faults. (b) Intermediate analysis state. Each dot represents the center of mass of a Burgers circuit traced around the dislocation cores. Dot colors indicate Burgers vector family (perfect dislocations [red], partial dislocations [green], stair-rod dislocations [yellow]). (c) Final analysis results. Gray arrows depict Burgers vectors in world space (exaggerated magnitudes).

With the help of the dislocation analysis technique, it is not only possible to visualize the complex dislocation reactions observed in the simulation, but also to asses these processes in a quantitative way. Figure 19 shows the measured total dislocation line length in the system, from which the dislocation density can be directly derived. Interestingly, the dislocation density does not increase monotonously in this simulation, which is probably due to a delayed straightening or annealing of dislocations at the surfaces.

4.3 DISLOCATION EXTRACTION ALGORITHM (DXA)

In the previous section, we have described the *on-the-fly dislocation detection algorithm* (ODDA). Among the various processing steps of the ODDA, tracing of short Burgers circuits around dislocation cores is the most important. In essence, the algorithm constructs a massive number of independent Burgers circuits around crystal defects and uses them to determine the Burgers vector and the location of dislocation segments. In the last two processing steps, these circuits are sorted by their Burgers vector and connected by one-dimensional line segments, which are finally joined to form a network.

The last two steps of the ODDA, however, can become unreliable in the case of complex and dense dislocation networks. The Burgers circuit search yields a large number of unordered space points with associated Burgers

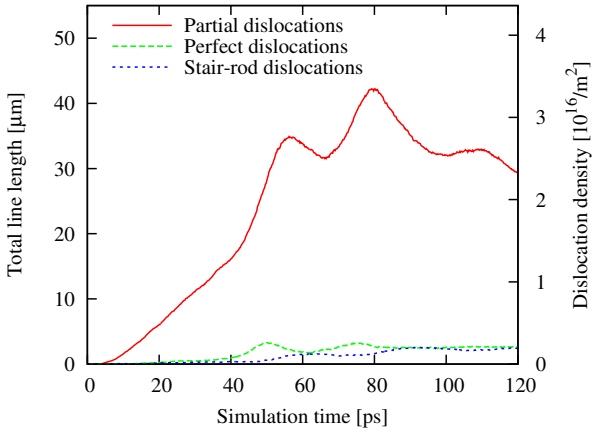

Figure 19: Quantitative analysis of the overall dislocation density for the simulation shown in figure 17. Not only can the total dislocation content in the system be measured, but even the contributions of different dislocation types can be distinguished with the dislocation analysis method.

vectors. It is virtually impossible to make the reconstruction of the line network from this incoherent point set sufficiently reliable to ensure that the topology of the atomistic dislocation network is preserved in all cases. If, for example, the density of obtained points is too sparse to construct a continuous line connecting these points, spurious dangling dislocations ending within a crystallite can occur in the output, which violate the Burgers vector conservation law [68]. This problem plays a minor role if average quantities like the total dislocation density are of interest, but it can render an investigation of details of a complex and dense dislocation network difficult.

In this section, we therefore propose an alternative algorithm, which follows a simple, but rigorous idea illustrated in figure 20. We directly translate the 'topological network' of disordered atoms into a network of connected dislocation segments, thereby preserving the true connectivity of crystal defects and the dislocation network down to the atomic level. The output provided by this algorithm is a network of one-dimensional dislocation lines, which entirely conforms to the Burgers vector conservation law. Moreover, the second algorithm delivers a geometric description of all other crystal defects besides the dislocations lines (e.g. grain boundaries, surfaces, pores etc.), which is very useful for visualization purposes and other applications. The basic algorithm requires only a single control parameter, making its usage extremely simple. We note however, that the alternative method is computationally more demanding than the one-the-fly detection algorithm, mainly because it cannot be easily parallelized.

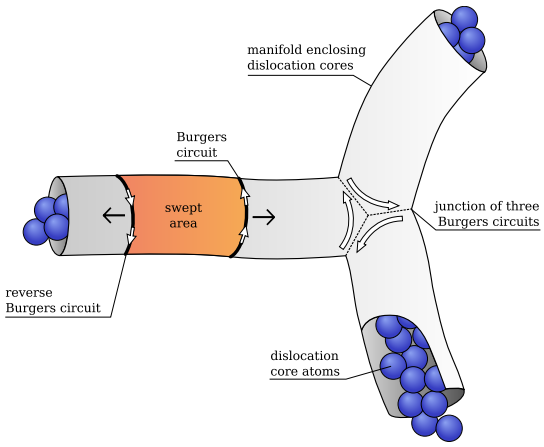

Figure 20: Schematic illustration of the *dislocation extraction algorithm* (DXA). First a manifold surface enclosing the dislocation cores is constructed. Then elastic 'Burgers circuit bands' are swept over the manifold along each dislocation segment. Finally dislocation junctions are generated where multiple Burgers circuits meet.

4.3.1 *Dislocation network extraction*

The *dislocation extraction algorithm* (DXA) consists of three principal steps:

1. The common neighbor analysis (CNA) method [72] is applied to identify crystalline atoms. We call the remaining atoms 'disordered atoms'.

2. A closed, orientable, two-dimensional manifold is constructed that separates the crystalline atoms from the disordered ones.

3. For each dislocation segment, an arbitrary Burgers circuit path is found on the manifold enclosing the segment. This closed circuit is moved in both directions to the two opposing ends of the dislocation segment (figure 20). While the circuit is advanced in each direction, a one-dimensional line representing the dislocation segment is constructed.

We describe these three steps in the following sections in more detail.

Note that we present an implementation of the DXA for fcc crystals. Its adaption to other crystal structures should require only minor modifications. In fact, most parts of the algorithm are independent of the crystal structure.

4.3.2 *Analysis of crystalline atoms*

During the first stage, fcc and hcp atoms (the 'crystalline' atoms) are identified using the common neighbor analysis (CNA) method (figure 21a). Note

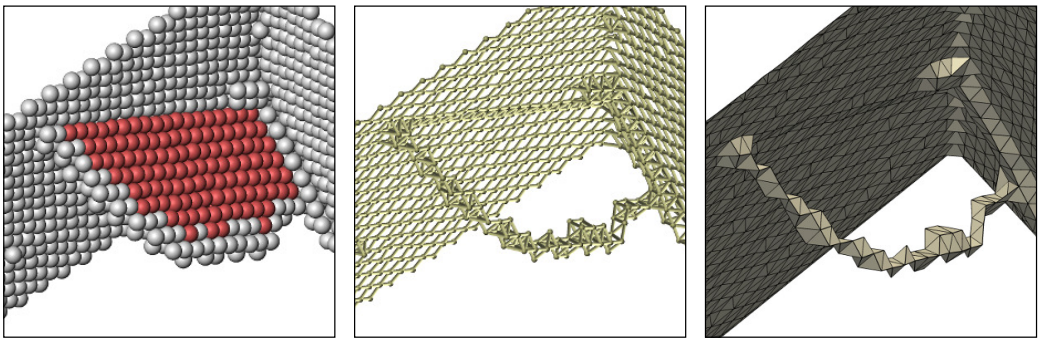

(a) (b) (c)

Figure 21: The three pictures show the construction of the interface mesh around crystal defects. (a) Atomistic input data after the common neighbor analysis has been applied. Grey atoms are 'disordered', red atoms are hcp-coordinated stacking fault atoms. The picture shows a Shockley partial dislocation being nucleated from two outer surfaces of the crystal. (b) The nearest neighbor bonds connecting disordered atoms. (c) The final interface mesh that covers all crystal defects.

that the identification of hcp atoms is required in an fcc crystal to properly account for stacking faults, coherent twin faults, and partial dislocations. By using a recursive walk algorithm over nearest neighbors, the crystalline atoms are decomposed into disjoint sets (crystallite clusters). In each crystallite cluster, a well-defined crystal lattice orientation is established: To this end, an arbitrary seed atom is picked and its 12 nearest neighbors are mapped to corresponding lattice vectors in an imaginary reference crystal. Then the procedure is repeated for the nearest neighbors that are crystalline as well, now ensuring that the chosen crystal orientation is aligned with the orientation of the first atom. Subsequently, the second neighbor shell is processed, and so forth, until corresponding lattice vectors are assigned to all nearest-neighbor bonds in the cluster.

In principal, we are now in the position to trace Burgers circuits through the crystal: Each step from a crystalline atom to one of its neighbors can be directly translated into a step in the imaginary reference crystal. If we construct a closed path through the real crystal, we could calculate its Burgers vector by adding up the corresponding lattice vectors for each traversed bond. The construction of a good Burgers circuit is, however, a non-trivial task that we will address in the following sections.

For the time being, we point out a feature of the CNA, which we will make use of: The CNA classifies each atom as either being crystalline (having fcc or hcp coordination) or as disordered. At the interface between crystalline

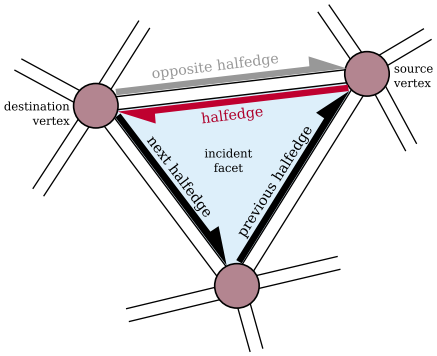

Figure 22: The halfedge data structure used to store the triangulated defect surface (the interface mesh).

and non-crystalline regions, however, there exists a layer of atoms, which are classified as 'disordered' by the CNA, but which are positioned on well-defined lattice sites. We name these atoms 'interface atoms' and they can be characterized as having at least one crystalline atom among their nearest neighbors (figure 21b).

4.3.3 *The interface mesh*

The second step of the DXA is to construct a surface (two-dimensional manifold) that separates the crystalline atoms from the disordered atoms. More precisely, a triangulation of the manifold is generated that consists of triangle facets and vertices, which are constituted by the interface atoms introduced above.

The triangulation of the interface manifold is stored as a *halfedge* structure [203, 116]. This combinatorial data structure consists of (i) vertices, (ii) halfedges, and (iii) facets. The following list describes the relationships between these entities, which are schematically depicted in figure 22.

1. Triangular facets are defined by a circular sequence of three connected halfedges.

2. A halfedge is defined by a source vertex and a destination vertex. Each halfedge is associated with exactly one incident facet, which it borders.

3. Each halfedge has an opposite halfedge that points from its destination vertex to its source vertex. Consequently, the opposite halfedge of the opposite halfedge is the halfedge itself.

4. Each vertex is associated with all its outgoing halfedges.

Vertices are constituted by 'interface atoms', which are at the surface of crystal defects. Halfedges are constituted by neighbor bonds between these interface atoms. And since interface atoms are located on well-defined lattice positions, as discussed above, we can assign a lattice vector from the imaginary reference crystal to each halfedge.

The constructed triangulation of the enclosing defect surface, the so-called interface mesh, satisfies two mathematical properties: It is closed and orientable. The interface mesh encloses dislocation cores as well as all other crystal defects including the free surfaces of the crystal (see figure 21c). Note that for outer crystal surfaces the interface mesh is oriented inward if we define the fully coordinated crystalline atoms to be on the positive side of the interface mesh.

4.3.4 *Elastic Burgers circuits*

By using a breath-first search algorithm, a closed circuit is constructed on the interface mesh that has a non-zero Burgers vector. The search is limited to a small recursive depth and is invoked at each vertex until a valid Burgers circuit is found. In this context, a Burgers circuit consists of a circular sequence of connected halfedges and encloses a dislocation segment.

The well-known Burgers vector conservation law states that the Burgers vector cannot change along a dislocation segment, and that the dislocation segment must either end in a dislocation junction or at an outer surface of the crystal. Note that a dislocation segment may also end at an inner surface of the crystal (e.g. a pore). But then, in a topological sense, the pore has to be considered part of the dislocation network as well. The sum of the Burgers vectors of all incident dislocation segments of the pore must add up to zero.

The interface mesh constructed in the previous step satisfies exactly these topological rules. Having constructed a first Burgers circuit on the interface mesh, one can consider this circuit as a closed rubber band around the dislocation core. We can now start to move this band along the tube-shaped interface mesh (figure 23a). Note that as long as we keep the elastic band closed, it will always enclose the same dislocation segment and the corresponding Burgers vector never changes, no matter how far we move it on the manifold. The elastic Burgers circuit is advanced facet by facet in the positive direction prescribed by the sense of the circular path. A second elastic Burgers circuit with reverse sense and reverse Burgers vector is generated at the same start position to sweep the dislocation segment in the opposite direction.

What happens when an elastic Burgers circuit band reaches the end of a dislocation segment? If the segment ends in a dislocation junction then the

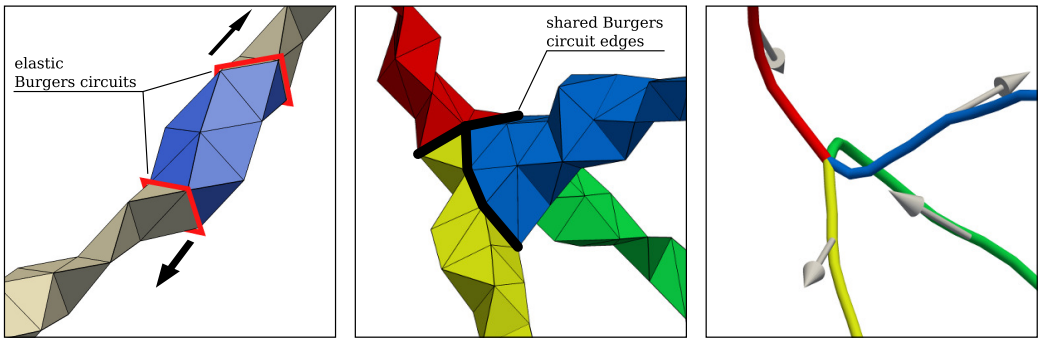

(a) (b) (c)

Figure 23: (a) Close-up view of the interface mesh enclosing a Shockley partial dislocation. The two Burgers circuits are advanced, facet by facet, in opposite directions to sweep the dislocation segment. (b) Interface mesh of a 4-segment junction. (c) The lines and Burgers vectors generated to represent the junction.

closed elastic band cannot overcome the furcation of the interface mesh. It is tied to its primary dislocation segment for topological reasons. We impose a maximum length on the elastic band to prevent it from being overstretched, that is, the Burgers circuit is no longer advanced as soon as this maximum length is reached. If the dislocation segments ends in an outer crystal surface, then the same principle applies: If the elastic band would be made extremely expandable, then it would wander along the outer surfaces indefinitely, still having the same Burgers vector of the primary dislocation it started from. That is why we impose an upper limit (on the order of 10 halfedges) on the length of elastic Burgers circuits to make them stop when the enclosed crystal defect widens from a thin dislocation core to an extended defect like a surface or a grain boundary.

4.3.5 *Transition to a network of one-dimensional lines*

The diameter of a typical dislocation core fluctuates along the dislocation line and the Burgers circuit has to stretch at the bulky points. On the other hand, we always ensure that the circuit is as short as possible (the 'elasticity' of the rubber band). A one-dimensional line representation of the dislocation segment is obtained by recording the current center of mass of the Burgers circuit every time the circuit is advanced by one step.

During the advancement phase, it is made sure that Burgers circuits do not interpenetrate other circuits from different dislocation segments. Dislocation junctions are then found by looking for Burgers circuits that touch each other

(figure 23b). If three or more circuits run into each other at a dislocation junction then we can connect the corresponding one-dimensional lines in the output (figure 23c). The way we constructed the elastic Burgers circuits ensures that Burgers vector conservation is automatically fulfilled at each junction. And if a Burgers circuit meets the reverse circuit of the same segment then we have found a closed dislocation loop.

4.3.6 *Extraction of other crystal defects*

Since we have imposed the maximum Burgers circuit length criterion, we will likely end up with some parts of the interface mesh that have not been swept by a Burgers circuit. These are the extended crystal defects, which we would not want to be represented by one-dimensional dislocation lines. Note that some of these defects, which include surfaces, grain boundaries, vacancies etc., still might have a non-zero Burgers vector associated with them.

The triangle facets of the interface mesh, which have not been swept, are taken as is. They can be used to visualize the extended crystal defects in addition to the extracted one-dimensional dislocation curves. In fact, the interface mesh method turns out to be very useful, even for the case of a completely dislocation-free crystal. It provides a good way of obtaining a volumetric representation of crystal defects, and could be used for analyses that are not feasible in the atomistic picture.

4.3.7 *Examples*

For a demonstration, we have applied the dislocation extraction algorithm to a quasi-static nanoindentation simulation and a large-scale MD simulation of nanocrystalline Pd. The nanoindentation simulation shown in figure 24a was performed with a quasicontinuum simulation method [47]. We analyzed a snapshot of the indented aluminum singlecrystal taken directly after the nucleation of dislocation loops underneath the spherical indentor. Note that since this is a zero-temperature simulation, the generated defect structure exhibits a high degree of rotational symmetry. Figure 24b displays the generated interface mesh for this atomistic snapshot. Regions of the interface mesh, which have been swept by elastic Burgers circuits, are colored according to their Burgers vector. Each of the colors corresponds to one of the 12 Shockley partial vectors of the fcc crystal lattice. The third image, figure 24c, shows the final results of the dislocation analysis. The arrows depict the directions of the Burgers vectors. Their signs appear to be arbitrary, but they are, of course, fixed with respect to the line directions. Note how several

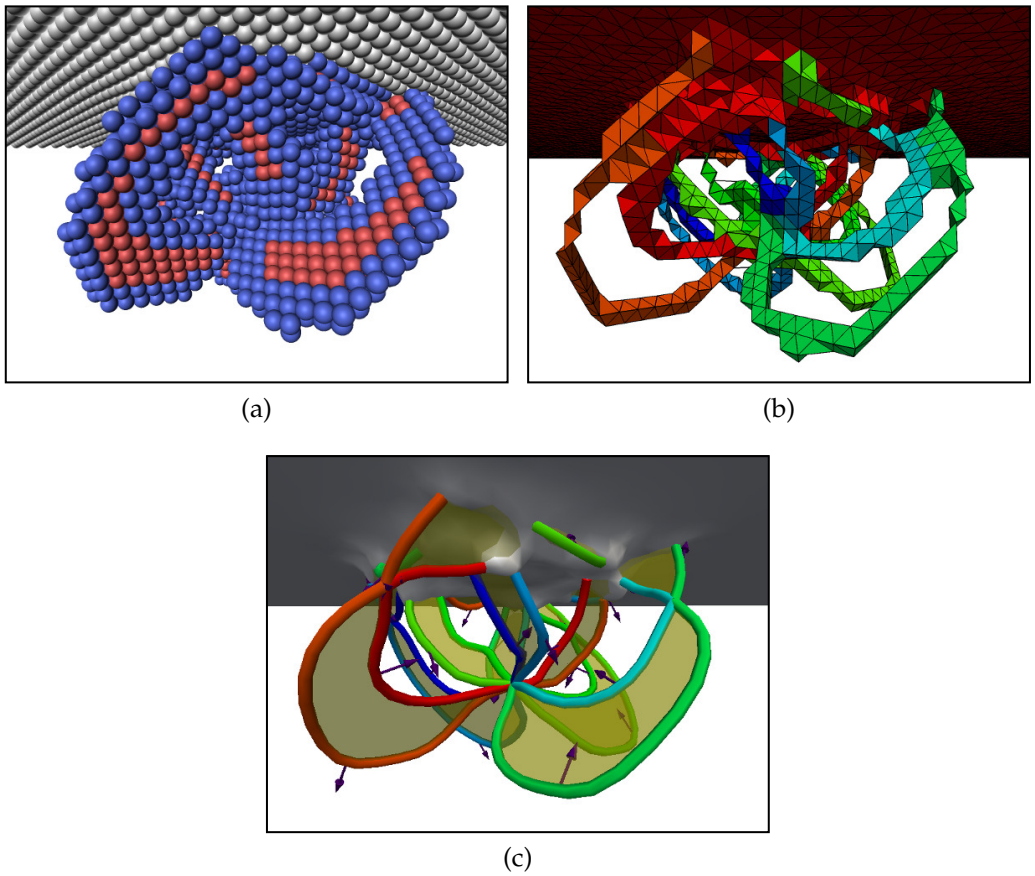

Figure 24: Analysis of the plastic region below a nanoindentor in singlecrystalline Al. (a) The atomistic snapshot. (b) The interface mesh covering all crystal defects. (c) The derived dislocation lines and their Burgers vectors.

dislocation segments join in a 'super node' in the central region below the indentor. This example demonstrates that the generated line representation of dislocations is certainly more valuable and expressive than the original atomistic description.

The nanocrystalline bulk structure of the second example (figure 25a) has been prepared with the Voronoi tessellation method and consists of 54 grains with an average size of 15 nm. We deformed the sample in a simulated uniaxial tensile test and observed dislocation activity (figure 25b). Since the grains have random lattice orientations, one can find several low-angle and vicinal twin boundaries (figure 25c) in the polycrystal. These vicinal twin boundaries consist of a planar layer of hcp atoms, which is interrupted by an array of discrete dislocations. These geometrically necessary dislocations accomodate the deviation from the perfect twin configuration.

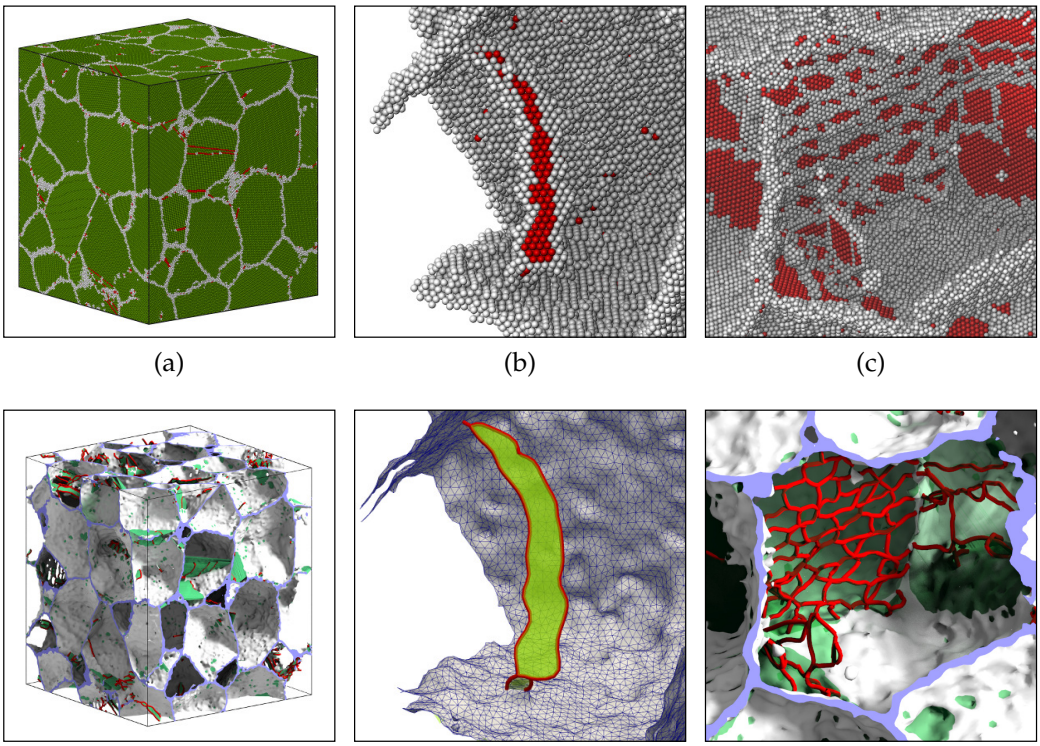

Figure 25: Analysis of a nanocrystalline Pd structure obtained from MD simulation. (a) The full atomistic system with marked grain boundary atoms. (b) Close-up view of a slightly dissociated dislocation in the interior of a grain. (c) A vicinal twin boundary (hcp atoms forming coherent twin planes have been marked red). (d–f) The extracted dislocation lines (red), stacking fault and twin boundary planes (semi-transparent green), and the smoothed interface mesh (gray), which covers all other crystal defects.

The DXA converts all general grain boundaries in the microstructure into a polyhedral representation, which is visualized in figure 25d. Note that the planar dislocation network of the vincinal twin boundary is correctly resolved by the algorithm (figure 25f). The coherent twin boundary regions and stacking faults constituted by hcp atoms are automatically converted into polygons (see next section), which are included in the visualization as semi-transparent planes.

The snapshot shown in figure 25 comprises 6.3 million atoms and contains approx. 2400 dislocation segments and 700 junctions. The generation of the interface mesh and the dislocation analysis take less than 60 seconds on a 2.6 GHz Intel i7 CPU. This is on the same order as the mandatory

neighbor list building and the common neighbor analysis (89 and 12 sec., both parallelized).

4.3.8 *Additional remarks*

We want to make a few additional remarks, which are helpful for a deeper understanding of the presented method:

Resolution parameter

In addition to the cutoff radius used for the CNA, the maximum Burgers circuit length is the only control parameter of the presented algorithm. It specifies the maximum lateral extension a crystal defect may have such that it is resolved as a one-dimensional dislocation line by the algorithm. On one hand, one would want to use a high value for this parameter to capture as many dislocations as possible. On the other hand, this parameter acts like a tolerance value: A large tolerance comes only with sacrificing resolution, especially in the longitudinal dislocation direction and at dislocation junctions. Note that this is a natural trade-off, which we are bound to, and which is directly reflected by this parameter.

Dealing with twinned crystals

The crystallite clusters constructed in section 4.3.2 comprise all connected crystalline (fcc/hcp) atoms. For the case of a twinned crystal, this implies that a cluster contains both the matrix and the twinned region as well as the layer of hcp atoms constituting the coherent twin boundary. This enables the detection of twinning dislocations, which are located in the twin boundary plane (see for example figure 25c). The Burgers circuit is traced from the matrix crystal into the twin and back into the matrix to enclose such twinning dislocations. Note that neighbor bonds in the twin crystal correspond to fractional lattice vectors in the imaginary reference crystal, which is always taken as a perfect cubic crystal without a twin boundary.

Disclinations

The lattice orientation of a crystallite cluster is not unique if disclinations [145] are present in the crystal. We find disclinations to be a very common feature of computer-generated nanocrystalline structures. Usually they occur if several grains are interconnected by small crystalline 'bridges', such that a closed circuit can be traced through several grains enclosing one or more triple junctions. Since the presence of disclinations precludes the usage of the

Burgers circuit concept (the Burgers vector becomes dependent on the exact path through the crystal), one has to 'conceal' the disclinations by splitting up such a 'super' crystallite into multiple isolated clusters, each encompassing only a single grain.

Thermal displacements

The DXA can be applied to snapshots of finite temperature MD simulations. The algorithm is not sensitive to thermal vibrations of atoms, but the CNA is. Hence, the same restrictions apply as for the CNA, which becomes unreliable at elevated temperatures close to the melting point. Usually, one can, however, effectively eliminate the random thermal displacements of atoms in an instantaneous snapshot by performing a time averaging of the atomic positions, or by applying a few iterations of a static minimization technique like conjugate gradients (CG).

Stacking fault planes

To extract stacking fault planes, which play an important role in fcc materials, we examine the outer contour of contiguous planes of hcp atoms. Since stacking faults can only be bordered by disordered atoms, the contour must pass along the interface mesh. As discussed above, the interface mesh is divided into regions which have been swept by elastic Burgers circuits as well as untouched regions. The swept regions have been converted into dislocation lines, which we can associate with the incident stacking fault. In a final step, the planar stacking fault contour polygon, which is now bordered by dislocation line segments and halfedges of the interface mesh, is tessellated into triangles for visualization (see the stacking fault ribbon between the two Shockley partials in figure 25e for an example).

Smoothing

For visualization purposes, we smooth the crystal defect surface as well as the dislocation lines using a volume preserving algorithm [173].

4.4 SUMMARY

Two novel analysis methods for atomistic simulations were introduced that provide the complete information on the dislocation topology contained in a snapshot of the simulated system. The *on-the-fly dislocation detection algorithm* (ODDA) is derived from the original definition of dislocations: the Burgers circuit test. By applying sophisticated pre- and post-processing

steps, a large number of Burgers circuits is used to identify and locate dislocation lines and to determine their Burgers vectors. The inspection and classification of dislocations – a laborious task usually done by hand in the past – can now be performed automatically on the fly, even for large-scale simulations containing a huge number of dislocations. Complex dislocation structures that involve dislocation junctions, partial dislocations and twinning dislocations can be identified without difficulty. The resulting vectorized representation of the dislocation lines allows to derive quantitative data from a simulation with high time-resolution, for instance the dislocation density.

When it comes to the analysis of dense and complex dislocation structures, for example close to a grain boundary, the *dislocation extraction algorithm* (DXA) is the method of choice. The network of one-dimensional continuous dislocation lines generated by the DXA is guaranteed to have the same topology as the real dislocation network. In particular, it always conforms to the Burgers vector conservation rule. Perfect as well as partial dislocations are resolved with atomic-scale precision. All other crystal defects (grain boundaries, surfaces, etc.), which cannot be represented by dislocation lines, are converted into a polyhedral volume representation by the algorithm. This volume representation is ideal for visualization purposes, even for applications which do not involve dislocations. Planar defects constituted by hcp atoms, like stacking fault and coherent twin boundaries, are converted into contour polygons. In summary, the DXA provides a simple-to-use and robust method to analyze and visualize atomistic simulations of crystal plasticity.

It is anticipated that these new methods can open a multitude of new possibilities for atomistic simulations of crystal plasticity. Some future applications are discussed in the outlook section of this dissertation.

5

NANOTWINNED FCC METALS: STRENGTHENING VS. SOFTENING MECHANISMS

5.1 INTRODUCTION

Experimental studies show that nanoscale growth twins in ultrafine Cu can significantly improve mechanical properties as compared to twin-free samples. In tensile tests and nanoindentation experiments, nanotwinned samples with various twin densities exhibit higher yield strength, tensile strength, and hardness as well as ductility [113, 36, 112]. The observed increase in strength with decreasing twin boundary distance is comparable to that found for conventional grain size refinement. That is, nanoscale twin boundaries seem to impart as much strengthening as conventional high-angle grain boundaries (GB) by blocking dislocation motion [113, 111] and exhibit a Hall-Petch (HP) type behavior. In contrast to nanocrystalline Cu with general GBs, however, nanotwinned Cu does not lose its tensile ductility when refined to the nanometer regime. In addition, twin boundaries usually exhibit much higher mechanical and thermal stability, and less electric resistivity in comparison to other grain boundaries [114, 111].

The recent experimental work on nanotwinned Cu [218, 112, 141, 111, 115, 158, 36, 69, 70, 113, 200] is accompanied by a series of molecular dynamics (MD) studies that investigate the effect of twin boundaries on the deformation behavior [59, 57, 104, 210, 98, 154, 155, 24, 78, 77, 221]. The aim of these simulations is to understand the atomistic mechanisms that give nanotwinned materials their unique properties. In general, the strengthening effect of nanolayered structures is understood to be the result of restricting dislocation motion from one layer to the next [166]. That is, twin boundaries are conventionally ascribed the role of barriers for dislocation motion. In MD simulations, however, slip transfer of dislocations across twin boundaries is observed under certain circumstances [210, 78, 77]. Nevertheless, the macroscopic strengthening effect of nanotwins in Cu has been found in all published simulation studies.

With only a very few exceptions [59, 57, 98], most work on the effect of growth twins on the mechanical properties of metals have been performed in Cu. Frøseth et al. [59, 57], however, have reported that nanotwinned Al exhibits enhanced plasticity in constant-stress simulations compared to its twin-free counterpart. This result suggests that other nanotwinned face-

centered cubic (fcc) materials might not show the strengthening effect found for Cu. Jin et al. [78, 77] studied the interaction of single dislocations with a twin boundary in Cu, Ni, and Al. They found several possible reactions, being dependent on the material's energy barriers, type of dislocation, and loading condition. For nanotwinned Pd, however, Kulkarni et al. [98] predict a performance based on simulated indentation studies that is very similar to Cu.

Experimental measurements indicate high densities of stacking faults and Shockley partials associated with the TBs in nanotwinned Cu [112] after deformation. In addition, a large number of debris was found in transmission electron microscopy (TEM) studies of deformed nanotwinned metals [113, 36]. Because of their design, previous computer simulations did not allow for direct comparison of these quantities with experiment, and efficient technologies to exactly measure such defect densities in large-scale atomistic simulations did not even exist. Furthermore, previous MD computer studies that investigated the strengthening effect of nanotwins used almost exclusively columnar, quasi two-dimensional simulation geometries based on periodic boundary conditions. In addition to a very small number of grains, this implies a reduction of available slip systems as well as degrees of freedom for grain boundary configurations. In fact, Frøseth et al. [59] have demonstrated that a two-dimensional simulation geometry can misleadingly promote mechanisms like deformation twinning in Al, which are superseded by other mechanisms when using a more realistic, fully three-dimensional simulation setup. Particularly, in regard to dislocation nucleation, a fully three-dimensional microstructure is crucial for accurately describing inhomogeneous stress-concentrations at nucleation sites, enabling the formation of curved dislocation segments, and to not preclude a multitude of possible reactions observed for dislocations on multiple slip systems.

In view of these results, the aim of the present study is to accurately compare the behavior of both nanotwinned Cu and Pd under realistic conditions and to assess whether the strengthening effect of twins observed in Cu is a general phenomenon present in all fcc metals. We use large-scale MD simulations of nanotwinned and twin-free, Cu and Pd polycrystals to address this issue. The fully three-dimensional model structures used in the present study consist of a statistically significant number of grains and grain boundaries. This allows for the formation of non-parallel dislocations lines and the inclusion of grain boundaries with both tilt and twist components in the microstructure without constraining the nucleation of dislocations [59]. We employ the newly developed dislocation and stacking fault analysis techniques presented in the previous chapter. This allows us to extract the true dislocation, stacking fault, and twin boundary densities as functions of

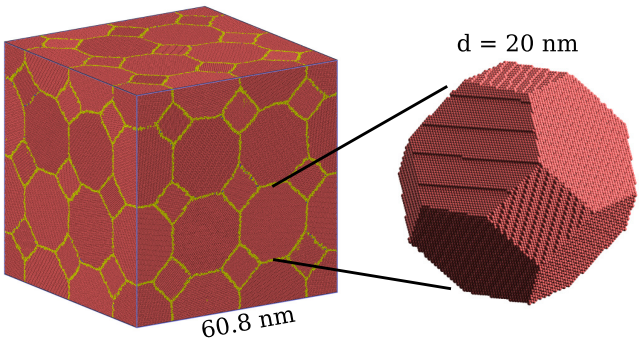

Figure 26: Nanocrystalline model structure used for MD simulations. The cubic simulation box contains 54 grains of the same size, having the same regular shape but different lattice orientations. The system contains approximately 15 million atoms and periodic boundary conditions were applied in all three spatial directions. Atoms in the grain boundaries have been marked with a yellow color.

strain from MD simulations and to directly compare them with experimental measurements.

5.2 METHODS

5.2.1 *Simulation procedure*

The Voronoi tessellation method was used to prepare three-dimensional, nanocrystalline model structures containing 54 grains with a size of 20 nm. This relatively large grain size reduces the contribution of GB mechanisms like grain rotation and grain sliding to plasticity, which begin to dominate over dislocation glide at smaller grain sizes [191, 151]. The Voronoi points were positioned on a body-centered cubic (bcc) superlattice, resulting in grains that have the shape of a truncated octahedron as shown in figure 26. Experimental structures often exhibit a log-normal grain size distribution. Here, we used a single grain size and shape to enable a better comparison between different grain and twin orientations and different fcc materials, leaving all other preparation parameters the same. Periodic boundary conditions were applied in all three spatial directions to model a bulk-like structure without free surfaces.

When defining the grain lattice orientations, we explicitly excluded low-angle grain boundaries and boundaries close to the $\Sigma 3$ twin configuration. In fact, the lattice orientation of each grain was repeatedly drawn from an isotropic random distribution until all grain boundaries in the structure

satisfied two requirements: All grain boundary misorientation angles were larger than 12 degrees and all as-prepared grain boundaries deviated from the twin configuration by more than 12 degrees. Both constraints are necessary to avoid the coalescence of neighboring grains and the formation of coherent twin boundaries due to grain rotation during the annealing phase described below.

In addition to the conventional nanocrystalline sample, which serves as a reference, the nanotwinned structure was prepared by introducing arrays of parallel twin planes with 4 nm spacing into each grain (see figure 28a). This twin spacing was found by Li et al. [104] to be the twin lamella thickness of maximum strength. Finally, we derived Cu structures from the Pd samples by rescaling the atomic coordinates by the ratio of the lattice constants, a_{Cu}/a_{Pd}, thereby preserving grain boundary misorientations and other topological features. This procedure results in a slightly reduced grain size (18.6 nm) in the Cu samples, but at the same time, it ensures an equal number of atoms (and number of dislocation nucleation sites) in both structures. This enables a direct comparison of the microscopic dislocation processes in both fcc materials. Note that the crystallite size in all samples is too small to support conventional dislocation multiplication by Frank-Read mechanisms.

As shown by Vo et al. [189], annealing of the samples at elevated temperatures is crucial for equilibrating grain boundaries in computer-generated polycrystals. Therefore all structures were annealed at 600 K for 400 ps before being quenched to 300 K, at which all deformation experiments were performed. All structures prepared in this way contained only general, high-angle grain boundaries in addition to the growth twin arrays and were free of lattice dislocations.

MD simulations were performed with the molecular dynamics code LAMMPS [139]. The atomic interactions were modeled with embedded-atom method (EAM) potentials for palladium [56] and copper [129], which correctly predict the experimental stacking fault energies of the materials (see figure 36). We used Berendsen's thermostat and barostat [9] to control temperature and relax the simulation cell size.

A strain-controlled, uniaxial tensile test at a constant engineering strain rate of $10^8\,s^{-1}$ up to 10% strain was conducted with each of the four samples. This corresponds to a simulation time of 1 ns. During such a straining simulation, the box length is constantly increased in the tensile direction, while the box size is allowed to relax in the two other directions.

5.2.2 *Analysis techniques*

To visualize crystal defects (dislocations, stacking faults, grain boundaries, etc.), we employ the common neighbor analysis (CNA) method [72]. The CNA alone, however, cannot distinguish between different types of crystal defects, nor can it determine any of their properties (like the Burgers vector of a dislocation). That is, it can only serve for visualization purposes. To overcome these limitations, we use the on-the-fly dislocation detection algorithm (ODDA) described in the previous chapter to identify and characterize dislocation lines in the MD simulations. The dislocation analysis is performed with a very fine time resolution at intervals of 200 fs to yield the instantaneous line shape and Burgers vector of each dislocation segment in the sample during deformation. It also provides information on the glide system of dislocations and the junctions they form.

In addition, we have implemented a second, novel analysis method to distinguish intrinsic stacking faults (ISF) from coherent twin boundaries (TB). In previous atomistic simulations, such planar defects were usually detected by identifying atoms having an hcp-like coordination, which is characteristic for both ISFs and TBs in fcc metals. Such hcp atoms can easily be extracted with the common neighbor analysis or similar methods alone. However, to distinguish between stacking faults and twin boundaries, an additional topological analysis of the surrounding atoms and crystal orientations is required. We have implemented such an improved analysis algorithm into the MD simulation code to count the respective numbers of atoms forming either ISFs or TBs. This, in turn, allows us to quantify the exact densities of stacking faults and twin boundaries in the material as functions of strain, and to make ISFs and TBs easily distinguishable in the visualization pictures. In the following figures, ISFs are marked red and TBs blue respectively.

Post-processing and visualization of simulation snapshots were performed with OVITO described in section 2.

5.3 RESULTS

The calculated stress-strain curves (figure 27) clearly show that nanotwins strengthen the material in the case of Cu. For Pd, however, there is a clear softening effect due to the presence of twins. This difference if investigated in the following.

Figure 28 shows cross-sections of the nanotwinned samples, revealing crystal defects formed inside the grains. Here, atoms belonging to coherent twin boundaries have been colored blue, intrinsic stacking faults have been marked red.

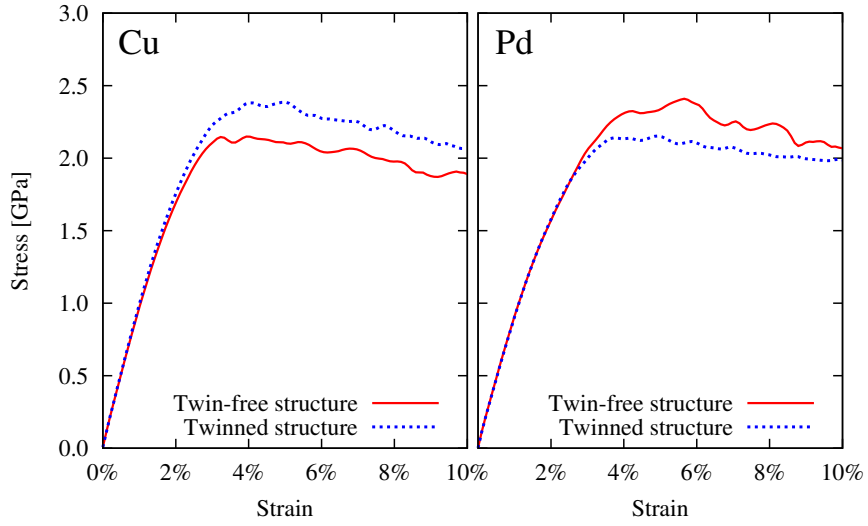

Figure 27: Stress-strain curves obtained for uniaxial tensile deformation of nanocrystalline Cu and Pd. For each element, two different structures were tested: A defect-free microstructure with 20 nm grain size and an identical structure containing growth twins (4 nm spacing). The simulated strain rate was $10^8\,s^{-1}$.

Nanotwinned Cu exhibits a very heterogeneous deformation behavior. Depending on the local grain and twin boundary orientation, we observe a combination of one or more of the following dislocation mechanisms: twin boundary migration, emission of partial or perfect lattice dislocations from the grain boundaries, formation of extrinsic stacking faults, and interaction of partial dislocations with twin boundaries. These processes have been described before for MD simulations of nanotwinned copper [57, 154]. In several grains, we observe dislocation transmission through twin boundaries (see section 5.5). However, the contribution of these transmitted dislocations to the overall plasticity is not significant. The formation of complex, three-dimensional dislocation entanglements can be observed. Partial dislocation segments are strongly curved, and at later stages of the deformation all sets of glide planes become populated in some of the nanotwinned grains.

A few of the randomly oriented grains in the simulated structure contain TBs with a high Schmid factor orientation. Dislocations in these grains are nucleated on slip systems parallel to the twins and no intersection of dislocations with the TB occurs. In contrast to these grains, grains with TBs on low Schmid factor planes show frequent blocking of transverse dislocations at the TBs. Partial dislocation loops, being nucleated from a grain boundary, are confined in between a single twin lamella (see section 5.5).

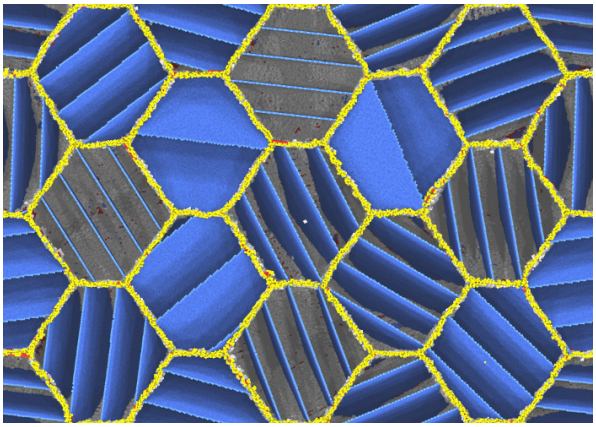

(a) As-prepared nanotwinned structure

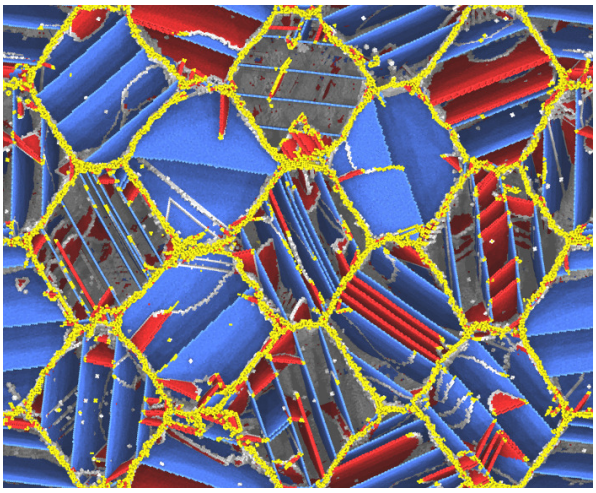

(b) Nanotwinned Cu after 10% strain deformation

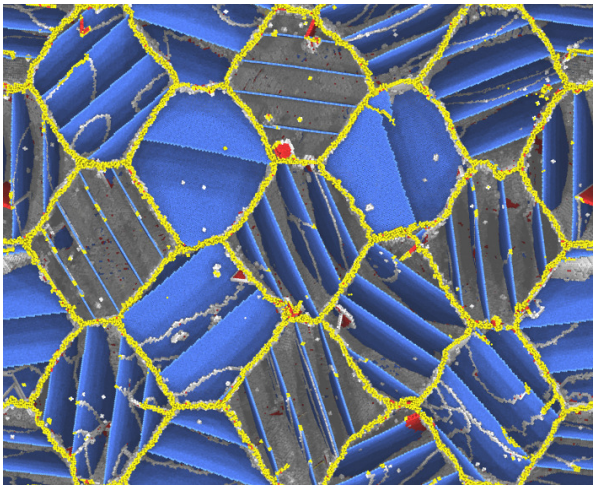

(c) Nanotwinned Pd after 10% strain deformation

Figure 28: Slices through the [110] plane of the simulation box showing the interiors of the nano-twinned grains. Crystal atoms with a perfect fcc environment have been removed in these pictures. (a) The as-prepared structure with regular-spaced twin boundaries in randomly oriented 20 nm grains; (b) Twinned nc-Cu after 10% tensile strain (along vertical axis); (c) Twinned nc-Pd after 10% tensile strain. Stacking faults have been marked red and coherent twin boundaries blue.

In contrast, nanotwinned Pd deforms almost exclusively via twin boundary migration. Irrespective of the local grain and TB orientation, primarily twinning dislocations are nucleated on glide planes parallel and adjacent to TBs. This restriction of dislocations to a single set of glide planes per grain, which mostly have low Schmid factors, demands an increased dislocation activity to reach a certain level of tensile strain. As can be seen in figure 28c, the twinning partials form a two-dimensional network on the twin planes. In several cases, we observe pile-ups of consecutive twinning partials. Even though dislocation slip is restricted to a single set of planes per grain, the polycrystalline microstructure does not fail. Instead, incompatible deformations of the grains are accommodated by GB motion and atomic shuffling in the GBs. In figure 28c, the displaced GB structure is marked with a yellow color.

5.3.1 *Planar fault densities*

We have measured the densities of intrinsic stacking faults and coherent twin boundaries that develop during deformation (third row of figure 29). The conventional nanocrystalline Cu and Pd samples are free of any planar faults in the beginning. The first plot in row three of figure 29 shows, however, that deformation twinning is an active mechanisms in nanocrystalline Cu, which sets in at 3.4% strain: A considerable number of TBs (blue color) is generated during deformation (reaching a density of $0.9 \cdot 10^8\,\mathrm{m}^{-1}$ after 10% strain). Deformation twinning is preceded by stacking fault formation starting at approx. 2% strain. After 10% strain, an ISF density of $0.9 \cdot 10^8\,\mathrm{m}^{-1}$ is reached. In nc-Pd, the generated number of planar faults is much smaller: Only about $0.06 \cdot 10^8\,\mathrm{m}^{-1}$ ISF and TB content is measured after 10% strain. These planar defects are found in slightly dissociated perfect dislocations and debris structures as shown in figure 32b.

The structures with as-prepared growth twins initially contain a TB density of $2.3 \cdot 10^8\,\mathrm{m}^{-1}$, which roughly corresponds to the 4 nm twin lamella spacing. In nanotwinned Cu, this density stays almost constant during deformation, while intrinsic stacking faults are generated by leading partials reaching a density of $0.6 \cdot 10^8\,\mathrm{m}^{-1}$. In nanotwinned Pd, the TB density decreases slightly during deformation as TBs loose coherency when more and more twinning partials are accumulated.

5.3.2 *Dislocation densities*

We employed the newly developed dislocation detection algorithm ODDA to extract all lattice and twin boundary dislocation segments in the MD simula-

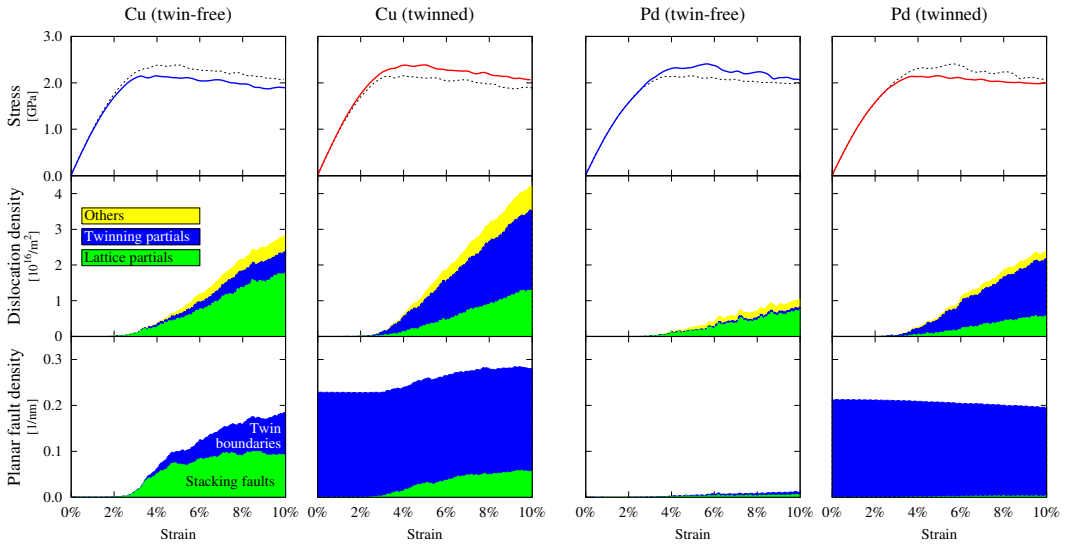

Figure 29: Measured tensile stress (1st row), dislocation density (2nd row), and planar fault density (3rd row) in simulated tensile tests as functions of strain.

tions and to measure their Burgers vector and length. The overall dislocation density can be directly derived from this data. One of the peculiarities of the ODDA is that it detects dislocations forming small-angle GBs and vicinal twin boundaries when a GB dissociates into discrete dislocation cores. Even though we explicitly avoided these types of GBs in our as-prepared structures, structural and angular changes of the GB during the deformation are inevitable. Thus, to suppress the detection of immobile GB dislocations, we excluded a 0.7 nm wide region on each side of the geometric grain boundary planes from our analysis, thereby taking only lattice dislocations in the grain interiors into account.

In case of dissociated $(a/2)\langle 110\rangle$ dislocations, the analysis algorithm yields in most cases the leading and trailing Shockley partials separately. A very small separation distance of one or two times the nearest-neighbor spacing is sufficient to resolve the cores of the two partials (section 4.2.1).

Lattice Shockley partials and twinning partials in fcc crystals have the same $(a/6)\langle 112\rangle$ type of Burgers vector, making them indistinguishable if only this vector is taken into account. However, they play different roles in plastic deformation. The former dislocation type carries conventional dislocation slip, whereas the latter type takes part in twin boundary migration. Thus, to distinguish these two types of partial dislocations, we count the number of crystallites through which a Burgers circuit passes when it is traced around the dislocation core: The core of a lattice Shockley partial is embedded in a single crystallite, whereas a twinning partial has a Burgers vector parallel

to the TB and is adjacent to two crystallites having the characteristic twin configuration.

Figure 29 (second row) shows the measured dislocation densities (averaged over all grains) as functions of tensile strain, ϵ. The total dislocation density, ρ, is split up into contributions from lattice Shockley partials, ρ_{lat}, twinning partials, ρ_{twin}, and other dislocations ($\boldsymbol{b} \neq (a/6)\langle 112\rangle$), ρ_{other}. Beginning at a strain level of $\epsilon = 1.92\%$, the dislocation density in initially twin-free nc-Cu increases almost linearly to ρ=2.8 $\cdot 10^{16}\,\mathrm{m}^{-2}$ after 10% strain. This includes a considerable number of twinning partials, reflecting the generation of deformation twins in nc-Cu. In nc-Pd, the accumulation of dislocations is smaller: Only a density of ρ=1.0 $\cdot 10^{16}\,\mathrm{m}^{-2}$ is reached in this material. Less than 8% of this value are twinning dislocations.

The introduction of growth twins promotes the accumulation of dislocations in both materials. Up to ρ=4.2 $\cdot 10^{16}\,\mathrm{m}^{-2}$ of total dislocation density is reached in nanotwinned Cu after deformation. The density of twinning partial reaches a level of ρ_{twin}=2.2 $\cdot 10^{16}\,\mathrm{m}^{-2}$. In nanotwinned Pd, the measured dislocation density is ρ=2.4 $\cdot 10^{16}\,\mathrm{m}^{-2}$, with ρ_{twin}=1.6 $\cdot 10^{16}\,\mathrm{m}^{-2}$ contributed by twinning dislocations.

5.4 DISLOCATION PLASTICITY IN NANOCRYSTALLINE COPPER AND PALLADIUM

The reference simulations of twin-free, conventional nanocrystalline Cu and Pd provide some interesting insights into the role of grain boundaries as dislocation sources. Figure 30 shows cross-sections of the nanocrystalline samples after deformation.

To study the onset of dislocation plasticity in the nanocrystalline structures, we use the dislocation detection algorithm to monitor all grains in the structure for the nucleation of dislocations. In twin-free Cu, the first leading partial dislocation is nucleated from a GB triple junction at 1.92% tensile strain. The Schmid factor for the corresponding $\{111\}\langle 112\rangle$ slip system is 0.496, which is the 5th largest among all 648 slip systems in the polycrystalline model structure. The nucleation of this first partial is immediately followed by the depinning of an already existing partial in another grain at 2.02% tensile strain. Figure 31 shows this depinning process, with the partial being part of an array of dislocation embryos formed during GB relaxation at the beginning of the simulation. The Schmid factor of the corresponding slip system is only 0.434 (position 63 in the Schmid factor list), exemplifying that the structure of the grain boundary is a very important factor that can greatly enhance dislocation nucleation.

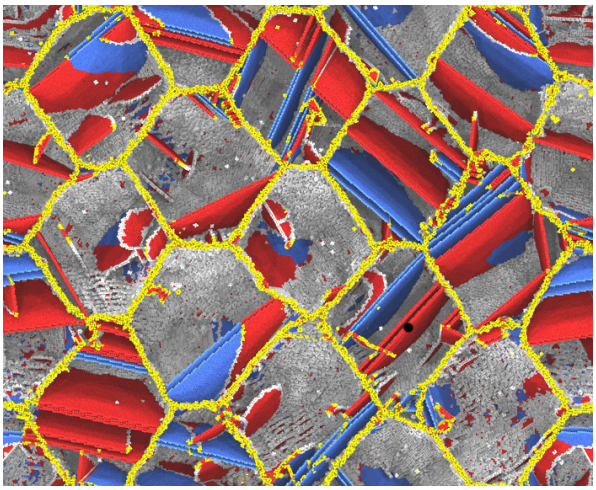

(a) nc-Copper after 10% strain deformation

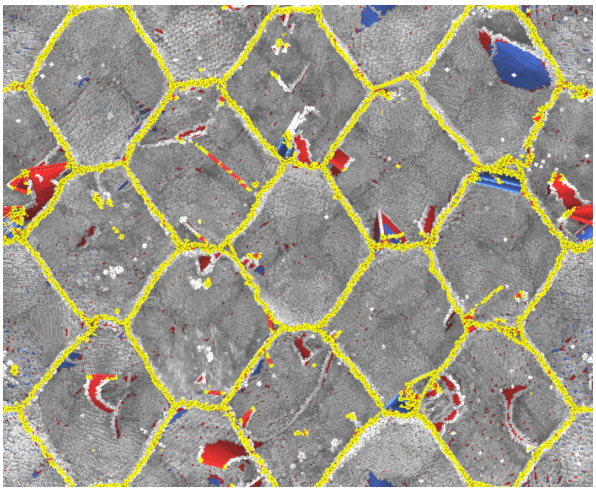

(b) nc-Palladium after 10% strain deformation

Figure 30: Slices through the [110] plane of the simulation box showing the interior of the grains. Crystal atoms with a pefect fcc environment have been removed to reveal grain boundaries, dislocations, and planar faults. (a) Nanocrystalline Cu (20 nm grain size) after 10% tensile strain (along vertical axis); (b) Nanocrystalline Pd after 10% tensile strain. Stacking faults have been marked red and coherent twin boundaries blue.

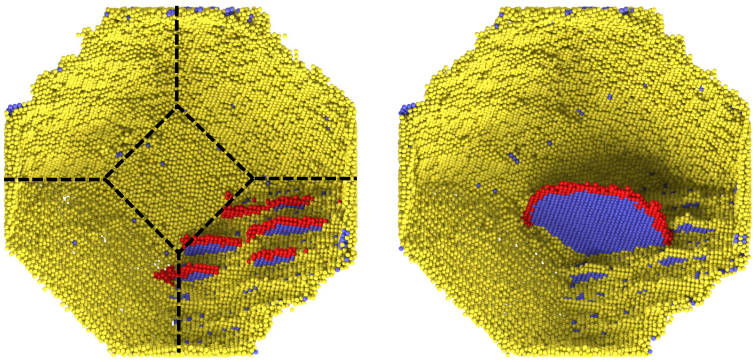

(a) (b)

Figure 31: Two snapshots of a grain boundary as seen from inside the grain. (a) The lower right part of the GB has a particular misorientation angle that results in the formation of an array of dislocation embryos during relaxation of the GB (marked red). Dashed lines denote GB triple junctions. (b) After loading the sample one of these embryos is activated and evolves to a lattice dislocation loop. In both Cu and Pd, this is one of the very first dislocation events, which occurs before other slip systems with higher Schmid factors are activated.

As the deformation proceeds, other grain boundaries begin to emit dislocations as well. The low stacking fault energy of Cu results in a splitting distance larger than the grain size, i.e., stacking faults span whole grains as being evident in figure 30a. We observe frequent generation of deformation twins. That is, intrinsic stacking faults left behind by leading partials are, in some cases, first transformed into extrinsic stacking faults, which then eventually widen to nanosized twin lamellae. This observation is confirmed by the increasing twin boundary density that we measure in the nanocrystalline Cu structure (lower left plot in figure 29). Twin growth proceeds by the emission of twinning dislocations on a parallel crystal plane adjacent to the TB.

In nc-Pd, the first observed dislocation is again the very same pre-existing partial dislocation that was formed during the relaxation of a grain boundary (figure 31) and was present in the Cu sample as well. It unpins at 2.70% strain, and – typical for Pd – is immediately followed by a trailing partial. During incipient dislocation activity, most dislocations reach the opposite grain boundary unobstructedly. Simultaneously, however, Lomer dislocations are nucleated at several grain boundaries and slowly grow into the interior of the grains. Figure 32a exemplarily shows such a dislocation. They act as obstacles to dislocations, and often, complex reactions with other dislocations

can be observed. Such reactions leave behind immobile dislocation debris, which contribute to the measured dislocation density (figure 29) and lead to an accumulation of dislocations in the grain interior (figure 32b).

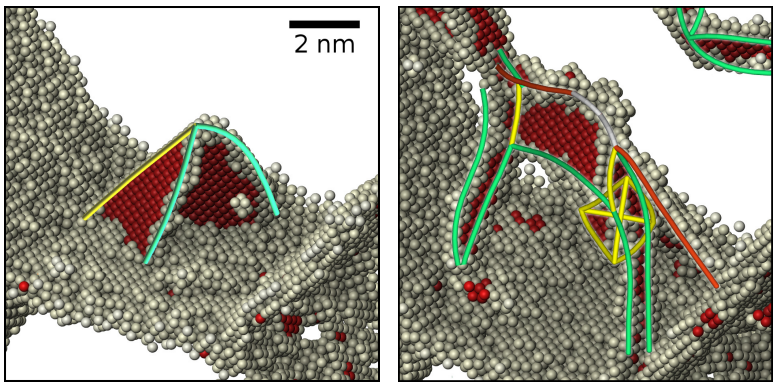

(a) (b)

Figure 32: Lomer dislocation nucleated from a grain boundary in nanocrystalline Pd. The extracted dislocation segments have been superimposed on the atomistic visualization. The left picture shows the stair-rod dislocation (yellow line) and the two stacking faults at an initial stage right after nucleation (at 4.3% strain). The right picture displays the same part of the crystal after 8.3% strain. After grown further, the Lomer dislocation has undergone several reactions with other dislocations and a complex defect structure has formed, including a stacking fault tetrahedron (four yellow lines). Shockley partials are represented by green lines and perfect dislocations by red lines.

5.5 DISLOCATION–TWIN BOUNDARY INTERACTIONS

Experimental reports of simultaneous ultrahigh strength and ductility in nanotwinned metallic systems motivate an in-depth investigation of dislocation–twin boundary interaction mechanisms. Jin et al. [78, 77] and Wu et al. [210] described several such mechanisms in their articles. Twin-mediated dislocation slip events are of particular interest since they are believed to contribute to the high ductility of nanotwinned copper. A second subject of a detailed analysis are the numerous stacking faults ribbons that form inbetween twin boundaries in copper. Figure 28b shows several of these ribbons (for instance in the central grain at the right image border).

We have studied the formation and evolution of one of these ribbons in more detail by using the automated dislocation analysis method. Figure 33a shows a sequence of three atomistic snapshots of a twin lamella, in which

such a stacking fault ribbon forms (blue atoms denote twin boundaries, red atoms denote stacking faults). Note that the time resolution of the atomistic snapshots is limited due to the data size of the 15 million atom system, and is not sufficient to resolve the stacking fault formation. Thus, we switch to the on-the-fly dislocation analysis, which was performed at much shorter time intervals during the simulation. Figure 33b displays snapshots of the extracted dislocation lines from the same perspective. The two gray discs schematically depict the boundaries of the twin lamella, which is surrounded by general grain boundaries. Initially, a leading partial dislocation loop is nucleated from one of these GBs and extends into the grain. Note how the twin boundaries constrain the dislocation loop to a narrow channel resulting in a high line curvature at the tip of the loop. While the loop is still expanding toward the opposite GB, both straight parts of the segment, lying in the twin planes, dissociate into stair-rod dislocations (blue lines) and two additional twinning partials, which glide in the twin boundary planes. The stable stair-rod dislocations now border the stacking fault ribbon (not visible in the visualization). In the present case, the trailing partial is nucleated from the right GB approx. 45 ps after the leading partial. It releases the stair-rod dislocations, and produces another pair of twinning partials gliding in the twin planes. Note how this process, which did not involve dislocation slip *across* twin boundaries, has created four additional dislocation segments *in* the twin boundaries, which potentially contribute to strain hardening.

Figure 34 shows the relative atomic displacements in nanotwinned copper after deformation. The color contrasts in this deformation map reveal continuous lines of plastic slip, which are traces of gliding dislocations. Some grains contain slip traces that pass across twin boundaries. One of these sites is marked with an arrow in figure 34.

We studied the dislocation activity in this region of the nanotwinned structure again by means of the automated dislocation analysis. Figure 35 shows a sequence of snapshots that illustrate this twin-mediated cross-slip of a screw dislocation. Initially, three twinning partials rest in the lower twin boundary. Two of them react (A) to form a perfect screw dislocation (B), which can then glide on a transversal plane toward the upper twin boundary (C). Here, the leading partial is stopped, and the two partials are constricted again to form a perfect dislocation segment (D), which cross-slips into the twinned crystal (E). Finally, at the stacking fault plane, the reverse process occurs, and the dislocation cross-slips into the glide plane again (F), which is parallel to the stacking fault.

We note again that, even though we observe twin-mediated cross-slip of dislocations in our simulations in a few cases, the small number of these events makes it unlikely that they significantly contribute to the overal ductility of the material.

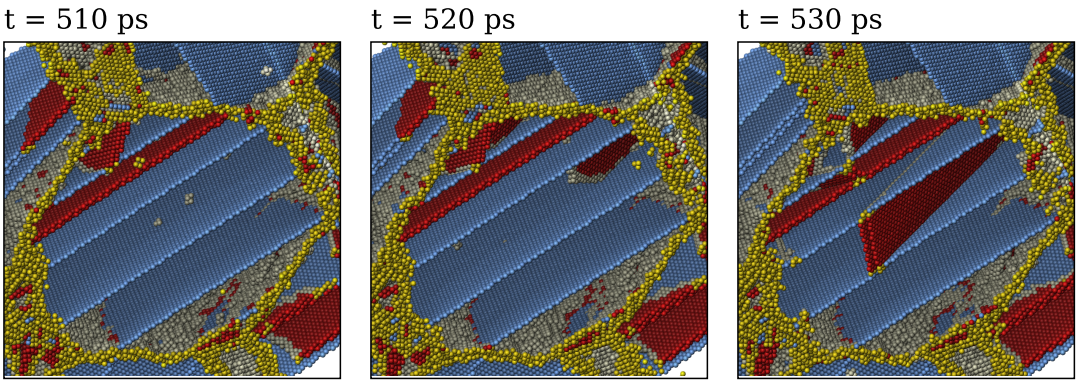

(a)

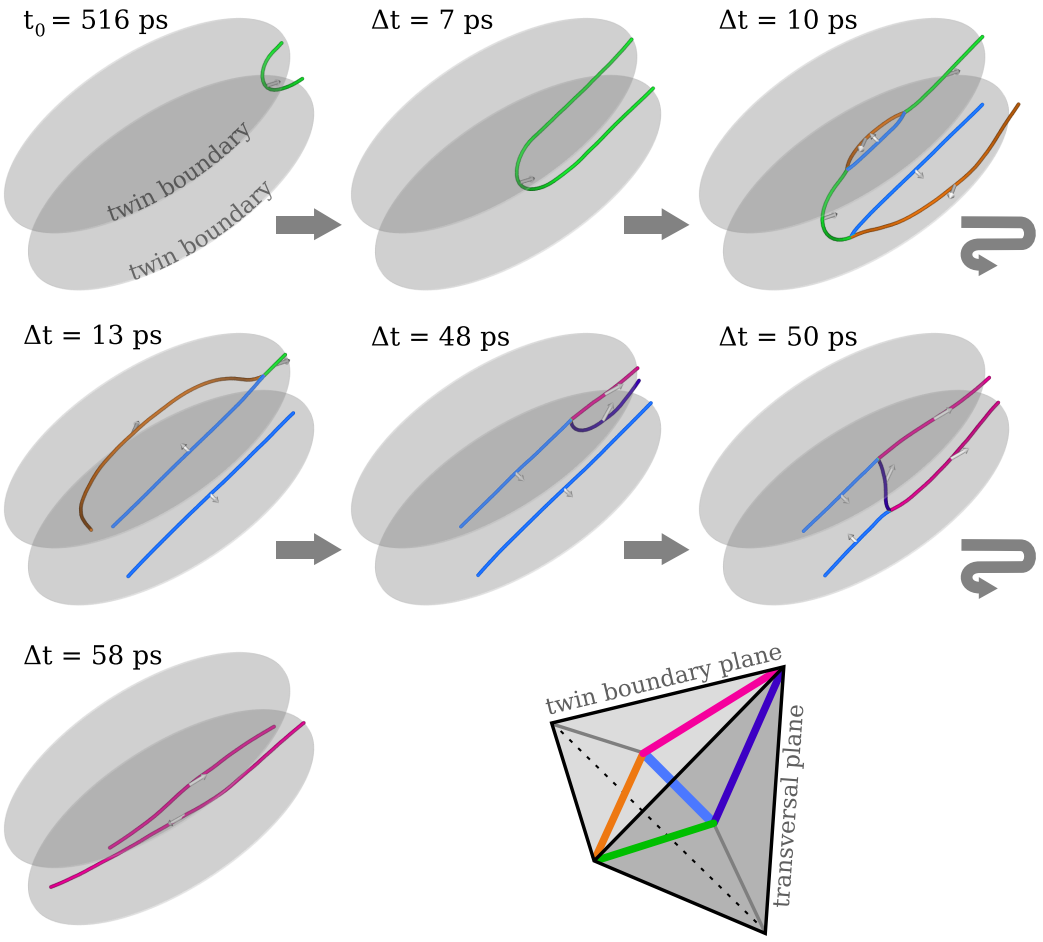

(b)

Figure 33: Formation and dissolving of a stacking fault ribbon in nanotwinned copper. (a) Atomistic snapshots (b) High time-resolution dislocation analysis.

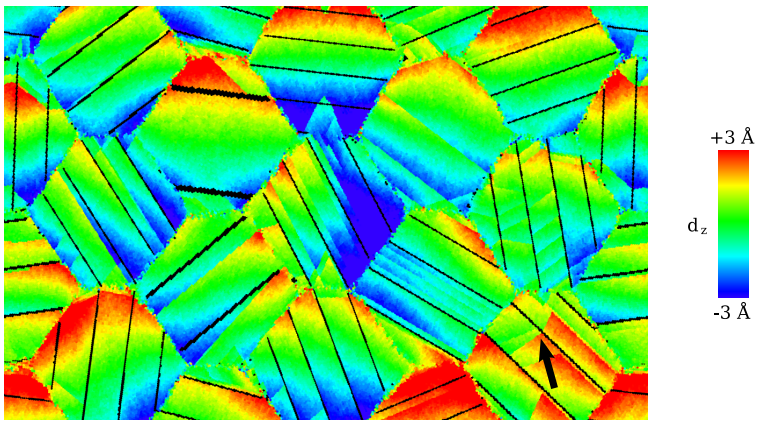

Figure 34: Cross-section of the nanotwinned Cu structure showing the relative atomic displacements after deformation. The relative atomic displacements d_z in the direction of the tensile axis are calculated by subtracting the macroscopic strain from the absolute displacements. Color constrasts originate from both dislocation slip traces and grain boundary sliding. Positions of the as-prepared coherent twin boundaries have been marked with black lines. The arrow points at a twin-mediated dislocation slip event discussed in the text.

5.6 DISCUSSION

From the measured stress-strain curves (figure 27), we find that nanotwins strengthen the material in the case of Cu, whereas they have a softening effect in Pd. As stated in the introduction, twin boundaries can function in two ways: being barriers for dislocation propagation and acting as dislocation sources. The latter effect dominates in nanotwinned Pd, where we observe a 21-fold increase of twinning partials and a 2.6-fold total increase of dislocation density caused by the growth twins. In contrast, the total density of both lattice and twinning partial dislocations in Cu is increased by only 50% due to the twins. The density of lattice partials slightly decreases in both metals when growth twins are present, because loop expansion is blocked by twin boundaries (found for Cu), or because nucleation of twinning partials is more favorable (found for Pd).

To better understand the differences between nanotwinned Cu and Pd, we have calculated the generalized planar fault energy (GPFE) curves for stacking fault formation and twin boundary migration in both metals (figure 36). The relative heights of the energy barriers associated with the nucleation of a lattice partial (being the generator of stacking faults) and a twinning partial (carrying twin boundary migration) can be estimated from these curves. For Cu, both nucleation barriers have a similar height, whereas Pd

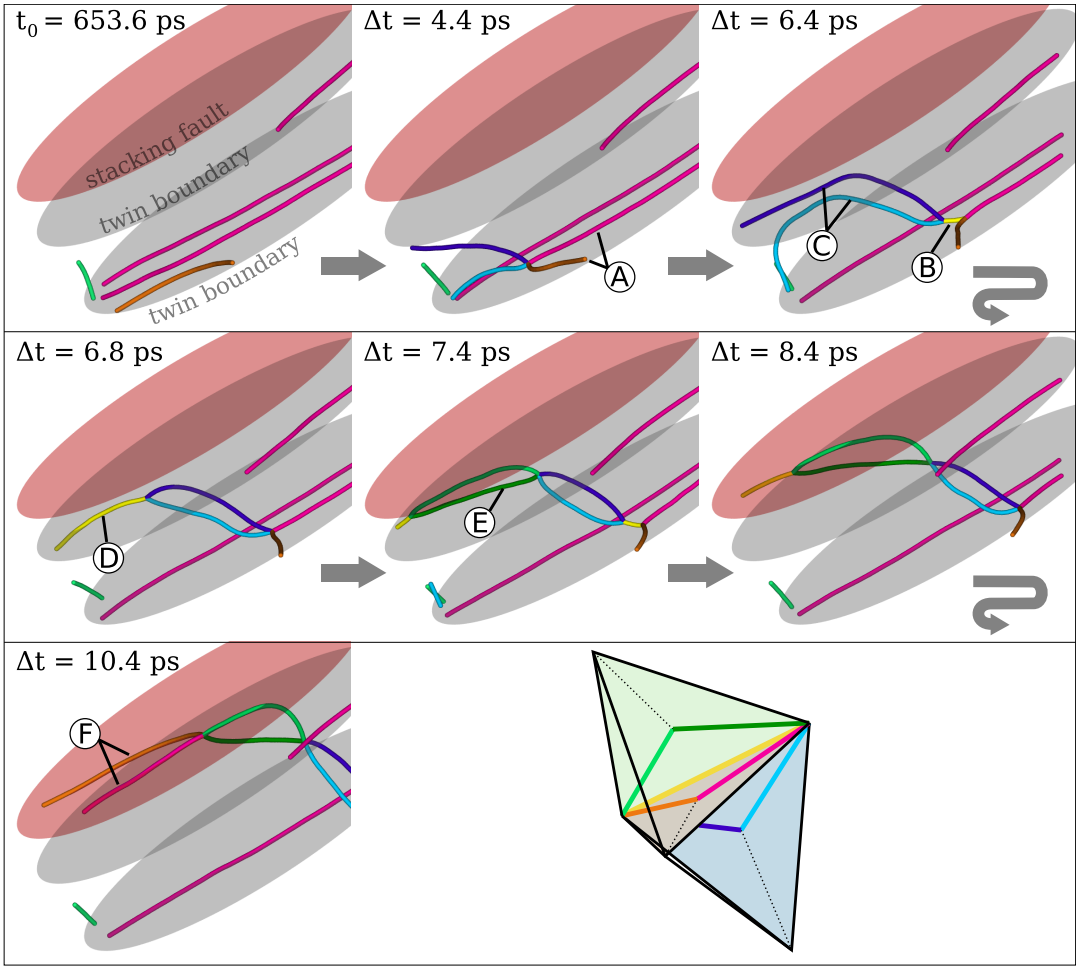

Figure 35: Twin-mediated cross-slip of a screw dislocation (see text). Dislocation lines have been extracted from the MD simulation and have been colored according to their Burgers vectors. The double Thompson tetrahedron depicts the orientation of the glide planes in the matrix (blue plane) and the twinned crystal (green plane).

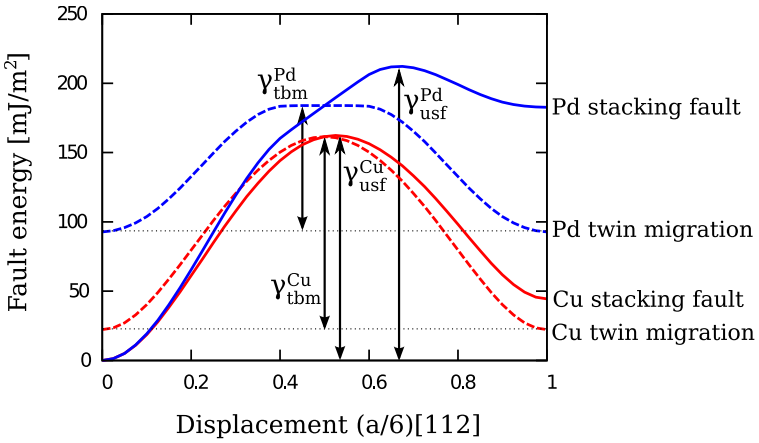

Figure 36: Generalized planar fault energy (GPFE) curves for Cu and Pd. The ratio of unstable stacking fault energy, γ_{usf}, to twin boundary migration energy, γ_{tbm}, is close to unity for Cu. In Pd, twin boundary migration is energetically favored over stacking fault formation.

shows a twin migration energy barrier that is much smaller than the stacking fault nucleation barrier. That is, the nucleation of twinning partials gliding parallel to the twin planes is energetically favored in Pd, and growth twins can no longer act as obstacles to dislocation motion in this case. Frøseth et al. have found a similar behavior for nanotwinned Al and give an in-depth discussion of this effect [59].

Our dislocation analysis algorithm allows us to determine the glide system of each partial dislocation nucleated during deformation. From this data, highly populated glide systems can be identified. Figure 37 displays the density of partial dislocations as a function of Schmid factor in the polycrystal. As expected, in twin-free Cu and Pd, the majority of dislocations occur on slip systems having high Schmid factors. Here, one must pay attention to the fact that the statistical number of available slip systems with a high Schmid factor is much smaller than the number of systems with a low Schmid factor, given a polycrystal with random grain orientations (dashed curve in figure 37). In the presence of growth twins, the difference between Cu and Pd becomes evident: In nanotwinned Cu, most dislocations accumulate on glide systems with a high Schmid factor, irrespective of the orientation of the twins. In nanotwinned Pd, the glide system population is shifted to lower Schmid factors and resembles the statistical orientation distribution of the twin planes.

This evidences that in nanotwinned Pd, the low twin migration barrier dictates the glide planes on which the majority of dislocations is nucleated. That is, the Schmid factor no longer influences the activation of slip systems.

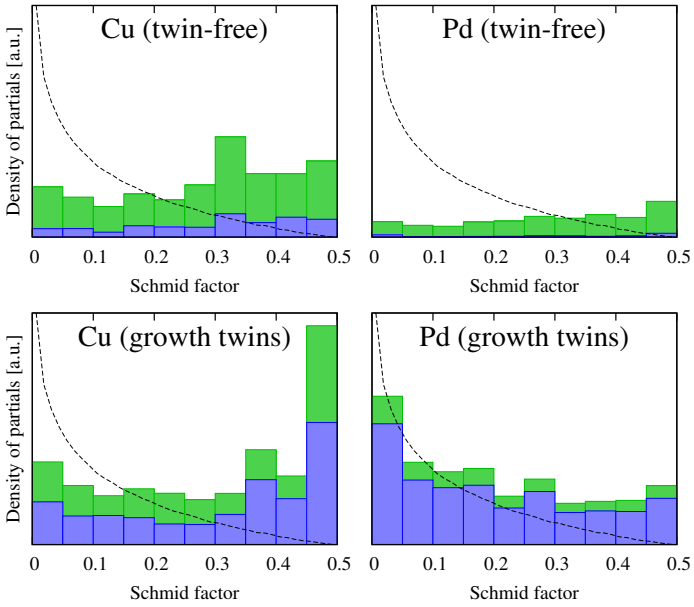

Figure 37: Average content of partial dislocations broken down into Schmid factor levels. These histograms have been generated by determining the Schmid factor of the slip system of each partial dislocation segment in the polycrystal. Blue bars denote contributions of twinning partials. For reference, the dashed curve indicates the number of available slip systems in an fcc polycrystal with random grain orientations.

In nanotwinned Cu, which exhibits a TB migration energy comparable to the stacking fault nucleation barrier, the deformation mode of a grain primarily depends on its relative orientation to the tensile axis. If TBs are parallel to planes with a high Schmid factor, dislocation glide occurs along the TBs and dislocations are not blocked. If, however, the grain orientation promotes dislocation nucleation on transverse glide planes, then TBs act as obstacles and have a strengthening effect (see figure 38). Shabib and Miller [155] propose a composite materials model with grains of the 'ductile' phase and of the 'strengthening' phase to characterize such an inhomogeneous behavior.

For deformed nanotwinned copper, experimental results indicate high densities of stacking faults and Shockley partials associated with TBs [113, 36, 112]. Our simulations confirm these qualitative observations and provide dislocation densities as a function of strain: The density of twinning partials reaches $2.2 \cdot 10^{16}\,\mathrm{m}^{-2}$ in nanotwinned Cu after deformation. This is in agreement with an estimation made by Lu et al. [112], who report a twinning partial density of $5 \cdot 10^{16}\,\mathrm{m}^{-2}$ determined from TEM images of nanotwinned Cu with 4 nm twin boundary spacing.

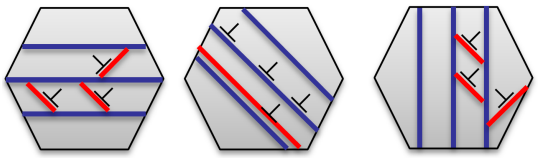

(a) Cu ($\gamma_{\text{tbm}} \approx \gamma_{\text{usf}}$)

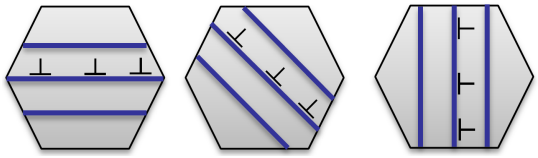

(b) Pd ($\gamma_{\text{tbm}} < \gamma_{\text{usf}}$)

Figure 38: Schematic illustration of the preferred glide systems in grains with varying orientation in nanotwinned Cu and Pd. Blue lines are pre-existing growth twins, red lines represent intrinsic stacking faults generated by Shockley partials.

In initially twin-free Cu, we observe deformation twinning (accompanyed by an increasing twin boundary density, see first plot in third row of figure 29), which is suppressed in pre-twinned Cu. Our simulations predict, however, a considerable generation of stacking faults in nanotwinned Cu. We measure a final ISF density of $0.6 \cdot 10^8\,\text{m}^{-1}$ after deformation. This is in qualitative agreement with experimental observations [113, 112], though, reliable experimental numbers have not been published.

In all four simulations, we measure a decreasing flow stress with increasing tensile strain (figure 27). This observation is in line with other computational studies. Brandl et al. [18] rationalized this by the occurrence of cross-slip, which allows dislocations to avoid regions of back-stresses in the grain boundaries caused by preceding dislocations not being fully absorbed in the boundaries. We, however, do not observe any significant occurrence of cross-slip in our simulations of nanocrystalline Cu and Pd. Instead, we can report a constantly increasing density of dislocations in the material (second row of figure 29), which certainly promotes plastic slip at higher strains. Our dislocation analysis gives no information on the mobility of dislocations, i.e., the exact fraction of pinned dislocations remains unknown. More advanced analysis methods need to be developed first to determine the contribution of individual dislocation lines to the total plastic slip.

The role of certain grain boundaries as effective dislocation sources is another important aspect that was revealed by our simulations. When preparing our virtual test samples, we explicitly excluded vicinal $\Sigma 3$ TBs as well as low-angle GBs. Both types of grain boundaries are already known to be effective sources for lattice dislocations [58, 51]. Our simulations

of nanocrystalline Cu and Pd show, however, that other high-angle grain boundaries can also exhibit a partially ordered structure. During relaxation of such as-prepared grain boundaries, an array of dislocation embryos evolves (see figure 31). These stacking faults can reach several angstroms into the grains. During deformation, they act as dislocation sources, which can easily be activated because no nucleation barrier has to be overcome. That is, our results show that some general high-angle grain boundaries can serve as efficient dislocation sources, similar to vicinal twin boundaries, and thereby promote the activation of non-optimal slip systems at low stresses.

5.7 SUMMARY

We have performed large-scale molecular dynamics simulations of nanotwinned fcc materials to study the effect of coherent twin boundaries on mechanical strength under uniaxial tension. All test samples consisted of a statistically significant number of grains and were prepared in exactly the same way to ensure comparability between materials as well as between twinned and conventional microstructures. A fully three-dimensional simulation setup was used to avoid intrinsic limitations of quasi-two-dimensional simulation cells. Our simulations clearly show that twin boundaries lower the yield strength of Pd, in contrast to nanotwinned Cu, were a strengthening effect is observed.

Based on a novel dislocation analysis method that identifies dislocation lines in atomistic simulations, we report exact dislocation densities in nanotwinned Cu and Pd as well as in their conventional nanocrystalline counterparts as a function of strain. Our measurements agree well with experimental data given for nanotwinned Cu. To explain the softening effect of twins in Pd, we determined the dominating type of dislocations in the material by partitioning the total dislocation density into contributions from lattice dislocations and twinning partials. We find that the low twin migration energy barrier of Pd promotes the generation of twinning partials at TB–GB junctions.

In nanotwinned Cu, dislocations are preferentially nucleated on slip systems with high Schmid factors. This leads to a blocking of dislocations in grains with twin boundaries on transversal crystal planes and the observed strengthening effect. In nanotwinned Pd, dislocations are restricted to twin boundary planes, irrespective of their Schmid factor, and plastic deformation proceeds by unhindered twin boundary migration.

Part IV

NANOCRYSTALLINE ALLOYS

6

MODELING TECHNIQUES FOR ALLOYS AT THE ATOMIC SCALE

6.1 INTRODUCTION

The interplay between chemistry and structure is of paramount importance in materials science. This applies in particular to alloys where chemical ordering and precipitation in conjunction with surfaces, grain boundaries, dislocations and other structural features give rise to an extraordinarily rich behavior.

In section 6.2, we discuss how to model chemical mixing on the atomic scale. The most common approach is to sample the chemical configuration space using transmutational Monte-Carlo (MC) methods, which require as key ingredient an appropriate statistical ensemble. We address how to adapt the introduced MC method for simulations of systems containing millions of particles. To this end, we derive transition matrices and their efficient decomposition. We finally discuss the simultaneous and efficient sampling of chemical, structural and vibrational degrees of freedom.

In the second part of this chapter, a concentration-dependent interatomic potential scheme is introduced that allows one to model concentrated alloys over the full composition range. In general, composition-dependent N-body terms in the total energy lead to explicit $(N+1)$-body forces, which potentially render them computationally expensive. We present an algorithm that overcomes this problem and that can speed up the calculation of the forces for composition-dependent pair potentials in such a way as to make them computationally comparable in efficiency and scaling behaviour to standard EAM potentials. We also discuss the implementation in Monte-Carlo simulations.

6.2 HYBRID MD/MC SIMULATION TECHNIQUE

Chemical mixing in alloys on the atomic scale is most commonly studied using Monte-Carlo (MC) simulations within either the semi-grandcanonical (SGC) or the canonical ensemble. The simulation algorithm for the canonical ensemble, however, is not suitable for massively-parallel simulations of large systems, because a simple decomposition of the transition matrix is not possible. That is why we employ the SGC ensemble in our simulations of

nanocrystalline alloys, which require large system sizes. In the following sections we describe the basic simulation method and a parallelization strategy that was developed to efficiently simulate large system sizes with regard to structural and chemical equilibration.

6.2.1 *The semi-grandcanonical ensemble*

The probability distribution function for the SGC ensemble reads

$$\pi_{\mathrm{SGC}} = \mathcal{Z}_{\mathrm{SGC}}^{-1} \exp[-\beta(E + \tilde{\mu}c)], \tag{6.1}$$

where $\mathcal{Z}_{\mathrm{SGC}}$ is the partition function of the SGC ensemble, β and E are the inverse temperature and the internal energy, while $\tilde{\mu}$ and c denote the chemical potential difference and the concentration.

For the present purpose, it is convenient to introduce the parameter $\mu = \beta\tilde{\mu}$ and rewrite equation 6.1 as

$$\pi_{\mathrm{SGC}} = \mathcal{Z}_{\mathrm{SGC}}^{-1} \exp[-\beta E - \mu c]. \tag{6.2}$$

The SGC ensemble can be sampled using a simple transmutation Monte-Carlo algorithm (Metropolis algorithm): (i) pick one particle at random, (ii) change its type from e.g., A to B or B to A, (iii) compute the energy change $\Delta E = E_{\mathrm{new}} - E_{\mathrm{old}}$, (iv) accept or reject this move using the transition matrix

$$K_{\mathrm{SGC}} = \min\{1, \exp[-\beta\Delta E - \mu\Delta c]\} \tag{6.3}$$

where $\Delta c = c_{\mathrm{new}} - c_{\mathrm{old}}$ is the concentration change associated with the trial move, and (v) return to the first step.

6.2.2 *Parallelization strategies for semi-grandcanonical MC simulations*

As discussed in the introduction, there are many problems including those addressed in this thesis which require simulations of systems with hundreds of thousands or millions of atoms. Efficient parallelization schemes with good scalability are needed in order to be able to address these cases. Here, we focus on short-ranged interactions as described by e.g., embedded atom method, bond-order, and Stillinger-Weber type potentials for which a spatial decomposition is the most efficient.

In systems with short-ranged interactions one can easily spatially decompose the simulation domain and assign the different parts to different processors (nodes) as shown schematically in figure 39. Then one divides each node into subdomains using e.g., the octant method as depicted in figure 39 with the only requirement that the side lengths of the octants

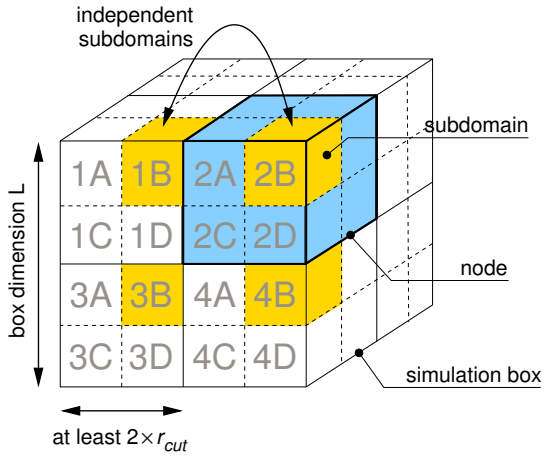

Figure 39: Spatial decomposition (solid lines) and subsequent division into octants (dashed lines) of a system with short-ranged interactions. Sets of octants with the same letter are independent of each other. One such set is marked in yellow.

cannot be smaller than a certain critical radius. (For pair interactions this critical radius equals the cutoff radius of the potential, while for EAM and three-body potentials the critical radius is usually twice the cutoff radius. An alternative to the simple octant method is presented in the next section). Now, it is possible to induce local modifications in these subdomains which do not affect the subdomains on the other processors: all subdomains "A" indicated in figure 39 are independent of each other and so are all subdomains "B" etc. The independence of certain sets of subdomains allows us to change them synchronously, i.e., the total change in energy is simply the sum of the local changes in energy $\overline{\Delta E} = \sum_i^N \Delta E_i$, where N is the number of nodes and ΔE_i is the change of the energy on the i-th node. Similarly, we have for the concentration $\overline{\Delta c} = \sum_i \Delta c_i$. In other words, the serial SGC-MC algorithm described in the provious section can be applied on each node individually.

Formally, the described procedure is equivalent to decomposing the transition matrix 6.3 into a product of subtransition matrices [81],

$$K_{\mathrm{SGC}}^{\mathrm{par}} = \min\left\{1, \exp[-\beta\overline{\Delta E} - \mu\overline{\Delta c}]\right\} = \prod_i^N \min\left\{1, \exp[-\beta\Delta E_i - \mu\Delta c_i]\right\} = \prod_i^N K_{\mathrm{SGC}}^{\mathrm{ser}}(i). \tag{6.4}$$

According to this equation each global Monte-Carlo trial move now consists of N independent local moves. To ensure uniform sampling of the system, the set of subdomains on which one operates has to be cycled. As long as the sampling is unbiased it does not matter whether this cycling is done systematically, e.g, following the sequence A $\rightarrow$ B $\rightarrow$ C $\rightarrow$ ..., or randomly.

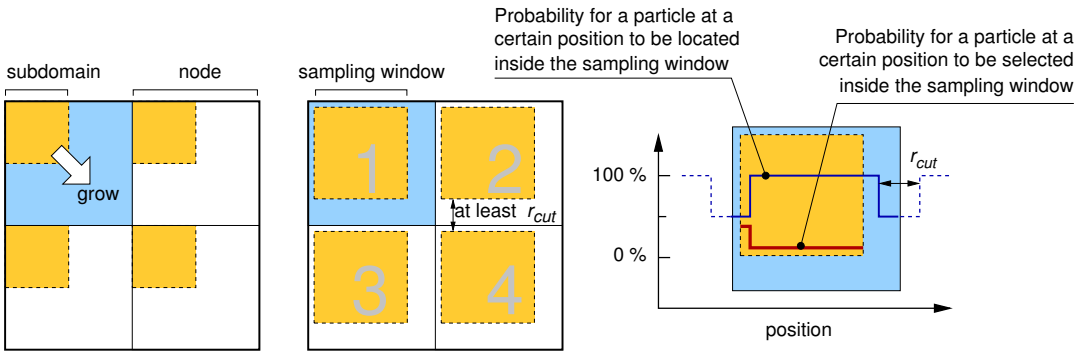

Figure 40: Schematic representation of an optimal spatial decomposition (compare figure 39)

This also implies that the parallelization does not affect the acceptance probability. In summary, the parallel SGC-MC algorithm comprises the following steps:

(i) pick a set of independent subdomains
(ii) in each subdomain pick a particle at random and change its type
(iii) compute the local energy change ΔE_i and the local concentration change Δc_i
(iv) on each node accept or reject the local trial move using the transition matrix $K^{\text{ser}}_{\text{SGC}}(i)$
(v) return to the first step.

6.2.3 *Optimal spatial decomposition*

If the simulation is run long enough to achieve equilibration, the octant method ensures that the system is sampled homogeneously and that the final result is unbiased. The octant method, however, does not guarantee that equilibrium is reached in the most efficient way. If during the equilibration phase precipitates are formed, the spatial confinement imposed by the size of the octants can "impede" their growth and thus the speed at which these precipitates coagulate and equilibrate. Since it is the size of the octants which causes this effect, one can mitigate the problem by increasing the size of the subdomains. As shown in figure 40, the octants introduced in figure 39 can be "grown" up to the maximum possible size dictated by the cutoff radius of the interaction model. In between MC trial moves the position of the sampling window has to be shifted synchronously over all processors in order to maintain the independence of the nodes and to include all particles in the sampling.

Now, however, special care must be taken to guarantee homogeneous sampling. Due to the larger size of the subdomains, the particles located at the center of a processor node will always be inside the sampling window regardless of its position. To ensure homogeneous sampling, the likelihood with which particles from different parts of the window are selected must therefore be inversely biased as schematically shown in the right panel of figure 40. For a given window position the particles at the border of the node must be picked with a higher probability than particles at the center of the node. By using this scheme one achieves an optimal sampling on each node without introducing a bias into the simulation.

6.2.4 *Sampling structural and vibrational degrees of freedom*

In the previous sections we have introduced the parallel SGC-MC algorithm that enables us to study systems with millions of particles. In many practical applications, the configuration space includes continuous (off-lattice) particle positions allowing for structural relaxations and thermal vibrations. We thus have to combine the transmutational MC scheme with an algorithm that captures structural and vibrational degrees of freedom. One option is to mix transmutation and displacement MC trial moves. In practice, however, such an approach is rather inefficient, especially for structural relaxation. A simple way to obtain a much more efficient algorithm is to combine transmutation MC moves with molecular dynamics simulations: After the systems has been evolved for a certain number of MD steps, one carries out a number of MC trial moves, before returning to the MD part. The number of MD steps between MC moves as well as the number of MC trial moves can be adjusted to optimize the convergence of the simulation.

6.3 CONCENTRATION-DEPENDENT POTENTIALS

In contrast to *ab-initio* methods, which can be applied to systems containing at most a few hundred atoms, semi-empirical interatomic potentials enable us to simulate systems containing millions of atoms on the time scale of nanoseconds. Large-scale MD and MC simulations of metals and alloys often make use of the embedded atom method (EAM) to calculate the interatomic energies and forces. Concentrated alloys that display a non-trivial concentration dependence in the heat of formation (HOF) are, however, beyond the scope of standard EAM models. In the standard EAM scheme, alloying effects are described in terms of the mixed pair interaction that has traditionally been adjusted to the heat of solution of a single impurity (dilute limit) [55]. Due to this constraint, the standard EAM model cannot

be adjusted to describe the inversion in the sign of the HOF of some binary alloys such as Fe–Cr and Ni–Pd.

The concentration-dependent model (CD-EAM) developed by Caro et al. [26] and first applied to the Fe–Cr system is an attempt to remedy this shortcoming. In this scheme, the pair potential for the mixed interaction is assumed to be the product of a function of the interatomic distance and the local concentration $h(x)$. This approach is particularly appealing since it is rooted in the Redlich-Kister expansion of the HOF used to describe alloys beyond the regular solution model. The introduction of the function $h(x)$, which can be obtained with minimal effort, allows the model to reproduce arbitrarily complex HOF curves. We will use the CD-EAM approach to create an alloy potential for the Pd–Au system in chapter 7.

An alternative approach to reproduce the complex shape of the HOF in Fe–Cr was proposed by Olsson et al. [134] based on the two-band model (2B-EAM) originally developed by Ackland and Reed [5] to describe materials with both *s*- and *d*-electron states at the Fermi energy. Both the CD-EAM and the 2B-EAM models have successfully been used at various occasions to study precipitation and ordering phenomena in Fe–Cr [134, 25, 99, 50, 13, 15].

In the literature, it has been argued that the CD-EAM and the 2B-EAM models are equivalent [14]. This equivalence, however, does not pertain to the expressions for the atomic forces. While the 2B-EAM model is a superposition of two EAM functions, the versatility of the CD-EAM total energy expression derives from terms that lead to explicit three-body forces. A naive evaluation of these forces in MD simulations requires much increased computational effort compared with the standard EAM. In addition, for MC simulations, the calculation of the energy change resulting from displacement or transmutation (change of chemical identity) of a single atom, involves atoms within twice the range of the potential cutoff, making it impractical for parallelized MC simulations as discussed in the previous sections [147]. In this chapter these computational issues of the CD-EAM model are addressed in two ways: First, the analytic expression for the CD-EAM forces is derived and it is shown how to efficiently calculate the three-body forces without a need for evaluating three nested sums, and second, a new formulation of the composition dependence is proposed that reduces the range for the energy calculations to the cutoff radius of the potential, while retaining the complexity implicit in its three-body interactions.

This second part of chapter 6 is organized as follows: The CD-EAM model is introduced in section 6.3.1, and the corresponding analytic force expressions for the CD-EAM model are derived in section 6.3.2. The computational efficiency of this model when implemented for MD simulations is discussed in section 6.3.3. On the basis of benchmark simulations we demonstrate that the computational effort for the CD-EAM model is only slightly higher

than for the standard EAM model. In section 6.3.4 we discuss why the original CD-EAM model is inefficient for MC simulations and show how this shortcoming can be circumvented by a modification of the model. The expressions for the interatomic forces for the modified model are obtained in section 6.3.5. The implementation of the modified CD-EAM model in MD and MC simulation codes is the subject of sections 6.3.3 and 6.3.6. We conclude that the new formulation speeds up the MC simulations by an order of magnitude while it is only slightly faster than the original formulation when applied to MD simulations.

6.3.1 *The concentration-dependent embedded atom method (CD-EAM)*

We begin by reviewing the CD-EAM potential model in its original form [26]. Analogous to the standard EAM model the total energy for a binary alloy involving elements A and B is given by

$$E = \sum_i^N E_i = \sum_i^N \left[F_{\alpha_i}(\varrho_i) + \frac{1}{2} \sum_{j \neq i} V_{\alpha_i \beta_j}(r_{ij}) \right], \tag{6.5}$$

where α and β denote the atom types and F_α is the embedding function for type α. The total electron density ϱ_i at site i is calculated as

$$\varrho_i = \sum_{j \neq i} \rho_{\alpha_j}(r_{ij}). \tag{6.6}$$

The pair potentials V_{AA} and V_{BB} for the pure elements are functions of the interatomic distance r_{ij} only, whereas the cross potential V_{AB} depends on both the distance r_{ij} and the local concentration x_{ij} according to

$$V_{AB}(r_{ij}) = h(x_{ij}) \phi_{AB}(r_{ij}). \tag{6.7}$$

The function $h(x)$ is fitted to reproduce the concentration dependence of the HOF. If $h(x) = 1$ the conventional EAM format is recovered. In the original CD-EAM model the cross pair potential ϕ_{AB} was simply chosen as

$$\phi_{AB}(r_{ij}) = \frac{1}{2} \left[V_{AA}(r_{ij}) + V_{BB}(r_{ij}) \right], \tag{6.8}$$

although in principle this function can be fitted as well. The local concentration of B atoms, x_{ij}, is estimated from the partial 'B electron densities' at sites i and j,

$$x_{ij} = \frac{1}{2}(x_i + x_j) = \frac{1}{2} \left(\frac{\varrho_i^B}{\varrho_i} + \frac{\varrho_j^B}{\varrho_j} \right) \tag{6.9}$$

with

$$\varrho_i^B = \sum_{j \neq i} \rho_{\alpha_j}(r_{ij}) \delta_{\alpha_j B}. \tag{6.10}$$

The Kronecker symbol $\delta_{\alpha_j B}$ in equation 6.10 equals 1 if atom j is of type B and equals 0 otherwise, i.e., the partial density ϱ_i^B includes only contributions from B atoms within the neighborhood of site i. Since the scaling function $h(x_{ij})$ and thus the pair interaction depends on the *local* concentration, the CD-EAM model can handle situations with a spatially varying composition including e.g., interfaces and precipitation processes.

To simplify the following derivations we introduce a shorthand notation for the site energies which can be split into three distinct parts:

$$E_i = F_i + v_i/2 + \overline{v}_i/2. \tag{6.11}$$

The energy of atom i comprises its embedding energy $F_i = F_{\alpha_i}(\varrho_i)$, its pair interaction sum v_i with atoms of the same species

$$v_i = \sum_{j \neq i} \delta_{\alpha_i \beta_j} V_{\alpha_i \alpha_i}(r_{ij}), \tag{6.12}$$

and its complementary pair interaction sum $\overline{v}_i$ with atoms of the other species

$$\overline{v}_i = \sum_{j \neq i} \overline{\delta_{\alpha_i \beta_j}} h\left(x_{ij}\right) \phi_{AB}(r_{ij}). \tag{6.13}$$

Here, the Kronecker symbol $\delta_{\alpha_i \beta_j}$ and its counterpart $\overline{\delta_{\alpha_i \beta_j}} = 1 - \delta_{\alpha_i \beta_j}$ have been used to differentiate between the case of two atoms of the same species and the case of two atoms of different species. The per-atom quantity v_i includes all pair-wise interactions of atom i with its neighbors of the same species, whereas $\overline{v}_i$ includes all cross interactions scaled by the concentration dependent factor $h(x_{ij})$.

Closer inspection of the total energy expression (equations 6.5 - 6.10) reveals that it contains three nested sums over atoms akin to a full-fledged three-body potential. In the present case, the absence of angular dependent terms, however, allows us to decompose the three-body sum into simple pairwise sums. As a result, the energy of the system can be calculated almost as efficiently as in the classical EAM model. Analogous to the latter model only two consecutive loops over all atom pairs are required to calculate all site energies simultaneously.

6.3.2 *Derivation of forces for the CD-EAM model*

For the sake of computational efficiency of MD simulations it is highly advantageous if the interatomic forces can be computed analytically. In this

section we derive the forces for the CD-EAM model. The force $\boldsymbol{f}_k$ acting on atom k is given by

$$-\boldsymbol{f}_k = \frac{\partial E}{\partial \boldsymbol{r}_k} = \sum_i^N \frac{\partial E_i}{\partial \boldsymbol{r}_k} \tag{6.14}$$

The terms F_i and v_i in the site energy expression equation 6.11 are part of the standard EAM model, so only the third term $\overline{v}_i$ needs special attention when doing the force derivation for the CD-EAM model. We begin by considering the derivative of the product $h(x_{ij})\phi_{AB}(r_{ij})$ from equation 6.13 with respect to the position $\boldsymbol{r}_k$ of some atom k:

$$\begin{aligned} \frac{\partial}{\partial \boldsymbol{r}_k}\left[h(x_{ij})\phi_{AB}(r_{ij})\right] = \\ h'(x_{ij})\phi_{AB}(r_{ij})\frac{1}{2}\left[\frac{\partial x_i}{\partial \boldsymbol{r}_k} + \frac{\partial x_j}{\partial \boldsymbol{r}_k}\right] + h(x_{ij})\phi'_{AB}(r_{ij})\frac{\partial r_{ij}}{\partial \boldsymbol{r}_k} \end{aligned} \tag{6.15}$$

The i-j-symmetry of the first term in equation 6.15 can be exploited in the context of a double sum. One can then do the simplification

$$\sum_{i,j\neq i}\frac{1}{2}\left[\frac{\partial x_i}{\partial \boldsymbol{r}_k} + \frac{\partial x_j}{\partial \boldsymbol{r}_k}\right] = \sum_{i,j\neq i}\frac{\partial x_i}{\partial \boldsymbol{r}_k}. \tag{6.16}$$

Thus we only have to differentiate the concentration at site i:

$$\frac{\partial x_i}{\partial \boldsymbol{r}_k} = \frac{\partial}{\partial \boldsymbol{r}_k}\frac{\varrho_i^B}{\varrho_i} = \frac{1}{\varrho_i^2}\sum_{l\neq i}\left[\rho'_{\alpha_l}(r_{il})\delta_{\alpha_l B}\varrho_i - \rho'_{\alpha_l}(r_{il})\varrho_i^B\right]\frac{\partial r_{il}}{\partial \boldsymbol{r}_k} \tag{6.17}$$

with

$$\frac{\partial r_{il}}{\partial \boldsymbol{r}_k} = \frac{\boldsymbol{r}_{il}}{r_{il}}[\delta_{ki} - \delta_{kl}]. \tag{6.18}$$

At this point, calculating the force $\boldsymbol{f}_k = -\frac{\partial E}{\partial \boldsymbol{r}_k}$ for a *single* atom k would require the evaluation of three nested sums over the indices i,j, and l (found in equations 6.14, 6.13, 6.17). But by incorporating the Kronecker deltas and by decoupling terms with independent indices we now prove that the computational complexity can be reduced to a single sum over index i.

Again we focus on the derivative of the cross potential term only (Equation 6.15), now in its full form, including both sums over i and j:

$$\begin{aligned} \sum_i \frac{\partial \overline{v}_i}{\partial \boldsymbol{r}_k} = \sum_i\sum_{j\neq i}\overline{\delta_{\alpha_i\beta_j}}\Bigg[h(x_{ij})\phi'_{AB}(r_{ij})\frac{\boldsymbol{r}_{ij}}{r_{ij}}[\delta_{ki} - \delta_{kj}] \\ + \sum_{l\neq i}h'(x_{ij})\phi_{AB}(r_{ij})\frac{1}{\varrho_i^2}\rho'_{\alpha_l}(r_{il})\left\{\delta_{\alpha_l B}\varrho_i - \varrho_i^B\right\}\frac{\boldsymbol{r}_{il}}{r_{il}}[\delta_{ki} - \delta_{kl}]\Bigg] \end{aligned} \tag{6.19}$$

The four Kronecker deltas in square brackets allow to eliminate one nested sum each, leaving only a double sum after renaming the indices:

$$\begin{aligned}\sum_i \frac{\partial \overline{v}_i}{\partial \boldsymbol{r}_k} = \sum_{i\neq k} \overline{\delta_{\alpha_k\beta_i}} \Bigg[& h(x_{ki})\phi'_{AB}(r_{ki})\frac{\boldsymbol{r}_{ki}}{r_{ki}} - h(x_{ik})\phi'_{AB}(r_{ki})\frac{\boldsymbol{r}_{ik}}{r_{ik}} \\ & + \sum_{j\neq i}\Bigg\{ h'(x_{ki})\phi_{AB}(r_{ki})\frac{1}{\varrho_k^2}\rho'_{\alpha_j}(r_{kj})\left\{\delta_{\alpha_j B}\varrho_k - \varrho_k^B\right\}\frac{\boldsymbol{r}_{kj}}{r_{kj}} \\ & - h'(x_{ij})\phi_{AB}(r_{ij})\frac{1}{\varrho_i^2}\rho'_{\alpha_k}(r_{ik})\left\{\delta_{\alpha_k B}\varrho_i - \varrho_i^B\right\}\frac{\boldsymbol{r}_{ik}}{r_{ik}}\Bigg\}\Bigg] \end{aligned} \tag{6.20}$$

The first two terms can be merged into one due to $\boldsymbol{r}_{ik} = -\boldsymbol{r}_{ki}$. In the inner sum's first term of equation 6.20 the indices i and j can be swapped without changing the value of the double sum. After this, terms that do no longer depend on index j can be moved out of the inner sum and the remaining part including the j-sum can be given a new name by defining the following per-atom quantity:

$$M_i = \frac{1}{\varrho_i^2}\sum_{j\neq i} h'\left(x_{ij}\right)\Phi_{AB}(r_{ij})\overline{\delta_{\alpha_i\beta_j}}. \tag{6.21}$$

Substituting this back into equation 6.20 leads to the simplified expression

$$\begin{aligned}\sum_i \frac{\partial \overline{v}_i}{\partial \boldsymbol{r}_k} = \sum_{i\neq k}\frac{\boldsymbol{r}_{ki}}{r_{ki}}\Big[& \overline{\delta_{\alpha_k\beta_i}}\cdot h(x_{ki})\phi'_{AB}(r_{ki}) \\ & + M_k\cdot\rho'_{\alpha_i}(r_{ki})\left\{\varrho_k\delta_{\alpha_i B} - \varrho_k^B\right\} \\ & + M_i\cdot\rho'_{\alpha_k}(r_{ki})\left\{\varrho_i\delta_{\alpha_k B} - \varrho_i^B\right\}\Big]. \end{aligned} \tag{6.22}$$

The full expression for the force acting on atom k is given in section 6.3.2, equation 6.26 along with the necessary steps to evaluate it in an efficient manner.

It was shown that the final expression for the forces can be broken down into pairwise sums in the same way as it is usually done for the standard EAM model. This allows for a very efficient calculation of the CD-EAM forces using three major computational steps:

- Step I. Compute and store the local electron density ϱ_i and partial density ϱ_i^B for each atom i,

$$\varrho_i = \sum_{l\neq i}\rho_{\alpha_l}(r_{il}) \tag{6.23}$$

$$\varrho_i^B = \sum_{l\neq i}\rho_{\alpha_l}(r_{il})\delta_{\alpha_l B}. \tag{6.24}$$

For performance reasons the derivative $F'_{\alpha_i}(\varrho_i)$ of the embedding energies should also be calculated at this stage and stored for later use in Step III.

- Step II. Compute and store the following per-atom quantity,

$$M_i = \frac{1}{\varrho_i^2} \sum_{j \neq i} h'(x_{ij}) \phi_{AB}(r_{ij}) \overline{\delta_{\alpha_i \beta_j}}. \tag{6.25}$$

- Step III. Compute the force $\boldsymbol{f}_k = -\frac{\partial E}{\partial \boldsymbol{r}_k}$ acting on each atom k,

$$\begin{aligned} \boldsymbol{f}_k = -\sum_{i \neq k} \frac{\boldsymbol{r}_{ki}}{r_{ki}} \Big[& F'_{\alpha_k}(\varrho_k) \rho'_{\alpha_i}(r_{ki}) + F'_{\alpha_i}(\varrho_i) \rho'_{\alpha_k}(r_{ki}) \\ & + \delta_{\alpha_k \beta_i} \cdot V'_{\alpha_k \alpha_k}(r_{ki}) + \overline{\delta_{\alpha_k \beta_i}} \cdot h(x_{ki}) \phi'_{AB}(r_{ki}) \\ & + M_k \cdot \rho'_{\alpha_i}(r_{ki}) \left[\varrho_k \delta_{\alpha_i B} - \varrho_k^B \right] / 2 \\ & + M_i \cdot \rho'_{\alpha_k}(r_{ki}) \left[\varrho_i \delta_{\alpha_k B} - \varrho_i^B \right] / 2 \Big]. \end{aligned} \tag{6.26}$$

Implementing these three steps in an MD code is straightforward and can be done on top of an existing EAM force routine. In the next section, we show that the computational cost for evaluating the CD-EAM forces in this way is only slightly larger than for conventional EAM models.

6.3.3 *Molecular dynamics performance*

We have implemented two different formulations of the CD-EAM potential model in the parallel MD code LAMMPS [139] to compare their computational performance with the standard EAM model. In this section we only discuss the original CD-EAM model, hereafter referred to as the *two-site* CD-EAM model for reasons that will become clear later. To benchmark its performance, we have carried out MD simulations of a bcc crystal at 300 K using periodic boundary conditions. For the CD-EAM case we considered a random alloy with 50% Cr while for the standard EAM case we considered a pure Fe sample. (Note that for standard EAM potentials the computational cost for pure phases and alloys is identical). Simulations were run on 1, 8, 27, 64, and 512 processors with 16,000 atoms per processor (weak scaling). The results for the CD-EAM routines and the LAMMPS standard EAM routine are displayed in figure 41. The two-site CD-EAM model is only about a factor of 1.7 slower than the standard EAM model. This is a small price considering the fact that the CD-EAM expression actually contains explicit three-body forces.

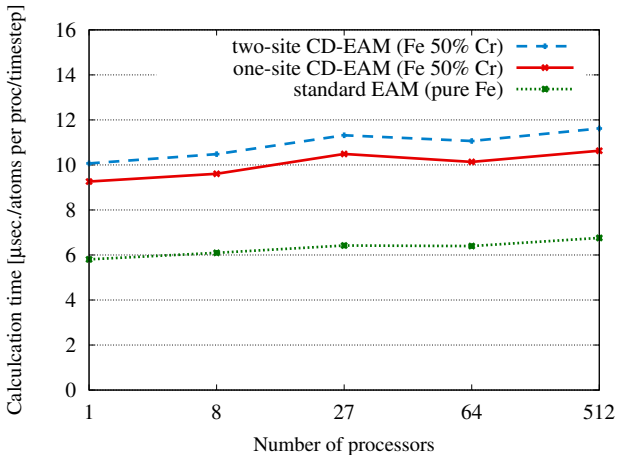

Figure 41: Comparison of the computation times for the CD-EAM models and the standard EAM model in a parallel molecular dynamics simulation. The benchmark simulation consists of a bcc crystal at 300 K with 16,000 atoms per processor.

6.3.4 *From the two-site concentration model to the one-site concentration model*

In the original formulation of the CD-EAM model the $h(x_{ij})$ function depends on the *average* concentration x_{ij} at the two sites i and j [see equation 6.9]. In section 6.3.1 it was pointed out that the calculation of the total potential energy is almost as straightforward as for the standard EAM case. But for the following two important reasons it turns out that this simultaneous dependency on two concentrations x_i and x_j is disadvantageous:

1. In a MC simulation one frequently needs to calculate the change in total energy, ΔE, resulting from a modification of the system. For most types of MC trial moves (atomic displacement, atom type exchange) the energy change ΔE is local. For performance reasons the calculation of ΔE is usually done by re-evaluating only those site energies that are immediately affected by the move. If one uses the original CD-EAM model the local concentration is computed as the average over the pair $i - j$ which implies that the effective range of the pair interaction is twice as large as the cutoff radius of the potential. While this definition is of little consequence for MD simulations in which the forces are calculated for *all* atoms at once, this definition implies that for the CD-EAM the calculation of local energy changes is much more expensive than for conventional EAM models (for which the effective pair interaction range is identical to the cutoff radius).

2. In section 6.3.2 it was shown that the calculation of the atomic forces for the CD-EAM model requires three loops over all atom pairs in the system. This is one step more than for the standard EAM model which requires only two consecutive passes: the first one to calculate the derivatives of the embedding energies and the second one to calculate the forces. For the CD-EAM model one additional computational step —and in a parallel implementation one additional communication call— are required to calculate the forces.

To summarize these arguments, although the CD-EAM is, in general, employable in large-scale MD studies, there is still room for improvement, and more importantly, its long-range character renders the model prohibitively expensive in the context of MC simulations.

Both of these shortcomings are remedied if one applies the following modification to the CD-EAM model. In equation 6.7 we make the replacement

$$h\left(\frac{x_i + x_j}{2}\right) \rightarrow \frac{h(x_i) + h(x_j)}{2}. \tag{6.27}$$

That is, instead of evaluating the function $h(x)$ at the average concentration of sites i and j, the average value of the $h(x)$ function at the two individual sites is taken to scale the A-B pair interaction. As a result, the individual site energies no longer depend on the local concentration at the neighboring sites. This can be shown by means of the identity

$$\sum_{i}^{N}\sum_{j\neq i}\frac{h(x_i) + h(x_j)}{2}\phi_{AB}(r_{ij}) = \sum_{i}^{N} h(x_i)\sum_{j\neq i}\phi_{AB}(r_{ij}). \tag{6.28}$$

The new site energy E_i^* then becomes

$$E_i^* = F_{\alpha_i}(\varrho_i) + v_i/2 + h(x_i)\overline{v}_i^*/2 \tag{6.29}$$

with

$$v_i = \sum_{j\neq i}\delta_{\alpha_i\beta_j}V_{\alpha_i\alpha_i}(r_{ij}), \tag{6.30}$$

$$\overline{v}_i^* = \sum_{j\neq i}\overline{\delta_{\alpha_i\beta_j}}\phi_{AB}(r_{ij}). \tag{6.31}$$

The per-atom quantity v_i includes all pair-wise interactions of atom i with its neighbors of the same species, whereas $\overline{v}_i^*$ includes all cross interactions scaled by the *same* concentration dependent factor $h(x_i)$ after the summation. This property of the site energy expression reduces the computational costs of the new CD-EAM formulation considerably, in particular in MC simulations.

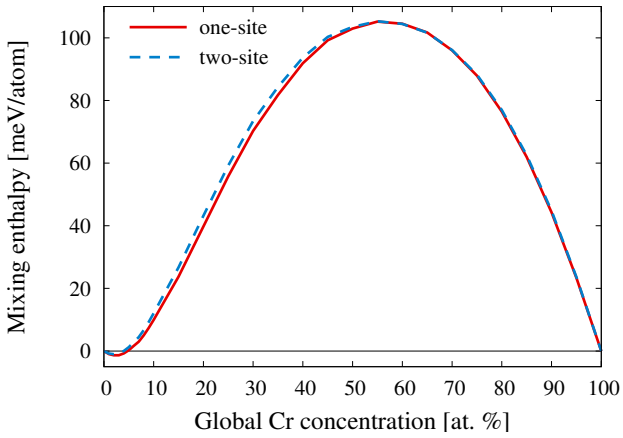

Figure 42: Formation energy of the Fe–Cr random alloy as a function of Cr concentration computed with the one-site and the two-site formulations of the CD-EAM model. The same scaling function $h(x)$ from [26] has been used in both cases. After fitting a new $h(x)$ function (as shown in figure 43) the one-site model yields exactly the same formation energy as the two-site model at all concentrations.

We refer to the new model as the *one-site* formulation, since the scaling function $h(x_i)$ is now a function of the local concentration at site i only. A detailed discussion of the performance aspects of this new formulation can be found in sections 6.3.5 and 6.3.6.

The substitution 6.27 corresponds to a linearization of the $h(x)$ function. Thus, as long as the concentration does not vary much from site i to site j, or if $h(x)$ is a rather smooth function of the local concentration, the effect of this replacement on the ij–pair energy is very small. It is, therefore, expected that the one-site CD-EAM model will give almost the same results as the two-site formulation when using the same parametrization.

The original CD-EAM model was developed for the Fe–Cr system. In Ref. [26] it was demonstrated that a CD-EAM potential can be fitted such that it exactly reproduces the shape of the input HOF curve at all concentrations. Based on the same EAM potentials for pure Fe [122] and Cr [197], and the $h(x)$ polynomial specified in Ref. [26] we have re-calculated the mixing enthalpy curve for the random alloy using the new one-site concentration CD-EAM formulation. The result, shown in figure 42, confirms that the proposed reduction to a single site dependency has a minor effect on the resulting mixing enthalpy. As expected, the difference between the two versions of the CD-EAM model is largest at concentrations between 20 and 30 at. % Cr, in the range in which the curvature of $h(x)$ is large (see figure 43). At concentrations above 50% Cr both models yield virtually the same result

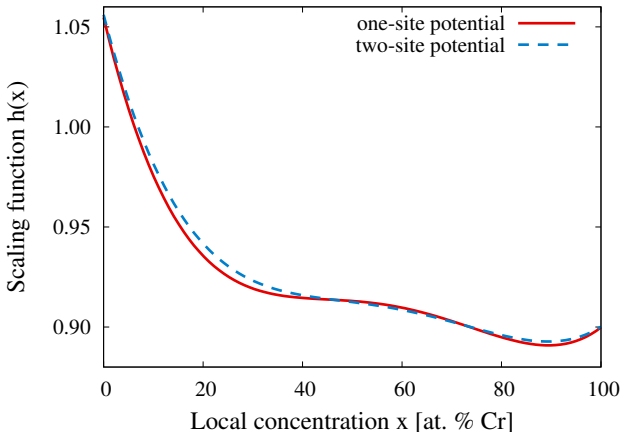

Figure 43: The $h(x)$ scaling polynomial for the original two-site Fe–Cr potential from [26] and the newly fitted polynomial for the one-site formulation. The nonlinear parts of the new curve are more pronounced to compensate for the larger fluctuations of the single site concentrations x_i in the random alloy.

Table 2: Coefficients of the 4th order polynomial $h(x)$ for the Fe–Cr potential in the one-site formulation. Here, x denotes the Cr concentration.

h_0	h_1	h_2	h_3	h_4
1.054732	−1.046606	2.886359	−3.445396	1.450731

because the $h(x)$ function is almost constant, and, therefore, linear in this composition range.

In order to further improve the one-site formulation, we re-fitted the $h(x)$ function using a least-square algorithm and a 4th order polynomial. The result is shown in figure 43 in comparison to the original polynomial of the two-site Fe–Cr potential [26]. The polynomial coefficients are given in table 2. As expected, inspection of the re-fitted $h(x)$ curve reveals that they differ the most in regions of large curvature. Recalculation of the random alloy formation energy based on the $h(x)$ function gives an exact match with the target curve, meaning that both formalisms are equally suitable to fit a given HOF.

6.3.5 *Derivation of forces for the one-site CD-EAM model*

In the one-site formulation of the CD-EAM model the main difference to the standard EAM model is the term $h(x_i)\overline{v}_i^*$ in equation 6.29. Therefore, it is sufficient to focus only on this term when doing the differentiation. We begin

by considering the derivative of this product with respect to the position $\boldsymbol{r}_k$ of some atom k:

$$\frac{\partial}{\partial \boldsymbol{r}_k}\left[h(x_i)\overline{v}_i^*\right] = h'(x_i)\frac{\partial x_i}{\partial \boldsymbol{r}_k}\overline{v}_i^* + h(x_i)\sum_{j\neq i}\overline{\delta_{\alpha_i\beta_j}}\phi'_{AB}(r_{ij})\frac{\partial r_{ij}}{\partial \boldsymbol{r}_k}. \tag{6.32}$$

The derivative of the concentration x_i is the same as for the two-site CD-EAM formulation, cf. equation 6.17. Again, we focus on the derivative of the cross potential term only as given by equation 6.32, now in its full form, including the outer sum over i from equation 6.14:

$$\begin{aligned}\sum_i^N \frac{\partial}{\partial \boldsymbol{r}_k}\left[h(x_i)\overline{v}_i^*\right] = \sum_i\sum_{j\neq i}\overline{\delta_{\alpha_i\beta_j}}\Bigg[&h(x_i)\phi'_{AB}(r_{ij})\frac{\boldsymbol{r}_{ij}}{r_{ij}}[\delta_{ki}-\delta_{kj}]\\ &+\sum_{l\neq i}h'(x_i)\phi_{AB}(r_{ij})\frac{\rho'_{\alpha_l}(r_{il})}{\varrho_i^2}\left\{\delta_{\alpha_l B}\varrho_i-\varrho_i^B\right\}\frac{\boldsymbol{r}_{il}}{r_{il}}[\delta_{ki}-\delta_{kl}]\Bigg].\end{aligned} \tag{6.33}$$

The four Kronecker deltas in square brackets allow to eliminate one nested sum each, leaving only a double sum after renaming the indices:

$$\begin{aligned}\sum_i^N \frac{\partial}{\partial \boldsymbol{r}_k}\left[h(x_i)\overline{v}_i^*\right] = \sum_{i\neq k}\overline{\delta_{\alpha_k\beta_i}}\Bigg[&h(x_k)\phi'_{AB}(r_{ki})\frac{\boldsymbol{r}_{ki}}{r_{ki}} - h(x_i)\phi'_{AB}(r_{ki})\frac{\boldsymbol{r}_{ik}}{r_{ik}}\\ &+\sum_{j\neq i}\Bigg\{h'(x_k)\phi_{AB}(r_{ki})\frac{1}{\varrho_k^2}\rho'_{\alpha_j}(r_{kj})\left\{\delta_{\alpha_j B}\varrho_k-\varrho_k^B\right\}\frac{\boldsymbol{r}_{kj}}{r_{kj}}\\ &-h'(x_i)\phi_{AB}(r_{ij})\frac{1}{\varrho_i^2}\rho'_{\alpha_k}(r_{ik})\left\{\delta_{\alpha_k B}\varrho_i-\varrho_i^B\right\}\frac{\boldsymbol{r}_{ik}}{r_{ik}}\Bigg\}\Bigg].\end{aligned} \tag{6.34}$$

The first two terms can be merged into one due to $\boldsymbol{r}_{ik} = -\boldsymbol{r}_{ki}$. In the inner sum's first term the indices i and j can be swapped without changing the value of the double sum. After this, terms that do no longer depend on index j can be moved out of the inner sum and the remaining parts including the j-sum have the same form as equation 6.31 and can therefore be replaced by $\overline{v}_k^*$ and $\overline{v}_i^*$ respectively. After this substitution equation 6.34 gets simplified to

$$\begin{aligned}\sum_i^N \frac{\partial}{\partial \boldsymbol{r}_k}\left[h(x_i)\overline{v}_i^*\right] = \sum_{i\neq k}\frac{\boldsymbol{r}_{ki}}{r_{ki}}\Bigg[&\overline{\delta_{\alpha_k\beta_i}}\left[h(x_k)+h(x_i)\right]\phi'_{AB}(r_{ki})\\ &+\overline{v}_k^*\frac{h'(x_k)}{\varrho_k^2}\cdot\rho'_{\alpha_i}(r_{ki})\left\{\varrho_k\delta_{\alpha_i B}-\varrho_k^B\right\}\\ &+\overline{v}_i^*\frac{h'(x_i)}{\varrho_i^2}\cdot\rho'_{\alpha_k}(r_{ki})\left\{\varrho_i\delta_{\alpha_k B}-\varrho_i^B\right\}\Bigg].\end{aligned} \tag{6.35}$$

Based on the above expressions for the interatomic forces, we now demonstrate that their calculation requires only two loops over all atom pairs (as opposed to three loops required for the two-site formulation). The necessary computational steps are,

- Step I. Compute and store the local electron density ϱ_i, the partial density ϱ_i^B, and the value $\overline{v}_i^*$ for each atom i:

$$\varrho_i = \sum_{l \neq i} \rho_{\alpha_l}(r_{il}) \tag{6.36}$$

$$\varrho_i^B = \sum_{l \neq i} \rho_{\alpha_l}(r_{il}) \delta_{\alpha_l B} \tag{6.37}$$

$$\overline{v}_i^* = \sum_{j \neq i} \overline{\delta_{\alpha_i \beta_j}} \phi_{AB}(r_{ij}). \tag{6.38}$$

  The derivative $F'_{\alpha_i}(\varrho_i)$ of the embedding energy should also be calculated at this point and stored for later use.

- Step II. Compute the force acting on each atom k,

$$\begin{aligned} -\boldsymbol{f}_k = \sum_{i \neq k} \frac{\boldsymbol{r}_{ki}}{r_{ki}} \Bigg[& F'_{\alpha_k}(\varrho_k) \rho'_{\alpha_i}(r_{ki}) + F'_{\alpha_i}(\varrho_i) \rho'_{\alpha_k}(r_{ki}) \\ & + \delta_{\alpha_k \beta_i} V'_{\alpha_k \alpha_k}(r_{ki}) + \overline{\delta_{\alpha_k \beta_i}} \frac{h(x_k) + h(x_i)}{2} \phi'_{AB}(r_{ki}) \\ & + \overline{v}_k^* \frac{h'(x_k)}{2\varrho_k^2} \cdot \rho'_{\alpha_i}(r_{ki}) \left\{ \varrho_k \delta_{\alpha_i B} - \varrho_k^B \right\} \\ & + \overline{v}_i^* \frac{h'(x_i)}{2\varrho_i^2} \cdot \rho'_{\alpha_k}(r_{ki}) \left\{ \varrho_i \delta_{\alpha_k B} - \varrho_i^B \right\} \Bigg]. \end{aligned} \tag{6.39}$$

Since it requires only two consecutive loops over all atom pairs, the new one-site CD-EAM model yields a superior simulation performance, as will be demonstrated in the following.

6.3.6 *MD/MC performance of the one-site CD-EAM*

In section 6.3.3, we have already discussed the MD performance of the two-site model. We concluded that in spite of its explicit three-body nature, the two-site CD-EAM model is only a modest 73% slower than the corresponding EAM model, if implemented optimally. In figure 41, we also show the performance of the one-site CD-EAM model. The latter is only 60% slower

than EAM, mainly because it does not require the additional third loop over all atom pairs to compute the forces as discussed in section 6.3.4.

Molecular dynamics simulations are limited when it comes to modeling phenomena such as precipitation, surface and grain boundary segregation, or ordering in alloys. Monte-Carlo (MC) methods, however, are ideally suited for such applications. The most common techniques are based on so-called swap trial moves, in which the chemical identity of a random particle is changed (see section 6.2.1). The resulting change in potential energy, ΔE, is used to decide whether the swap is accepted or rejected.

Therefore, the main task in a MC simulation is to calculate the change in potential energy induced by swapping the type of a single atom. For short-ranged potentials this can be done very efficiently, since the type exchange only affects the atoms in the neighborhood of the type swap. In the framework of the standard EAM model the situation is as follows: Changing the species of one atom directly affects (1) its embedding energy, (2) its pair-wise interactions with neighboring atoms, and (3) it indirectly changes the electron density at neighboring atoms and, thereby, their embedding energies. All these quantities need to be recalculated by visiting the atoms affected by the type swap.

In the case of the two-site CD-EAM model the situation turns out to be more laborious. Here, the site energy E_k of an atom k does not only depend on the local concentration x_k, but also on the concentrations x_j of all its neighbors j. This has a dreadful impact on the efficiency of the energy calculation. Changing the chemical identity of some atom i alters the local concentrations x_j of all its direct neighbors j, which in turn affects the mixed interaction of all atoms j with all of their respective neighbor atoms k. All of these have to be re-evaluated to compute the total change in energy induced by the single swap operation. The influence radius that has to be considered is therefore twice as large as the cutoff radius of the underlying EAM potential which – for the Fe–Cr potential – increases the computational costs by at least one order of magnitude.

The new one-site formulation proposed in section 6.3.4 resolves this issue. Although a single pair interaction between two atoms j and k still depends on the concentration at both sites [see equation 6.27], the site energy can be recast in a form that is independent of the concentrations on the neighboring sites [see equation 6.29]. As a result, the site energy of atom k is no longer affected by changing the type of an atom i that is farther away than one cutoff radius.

The performance gain due to the one-site formulation is illustrated in figure 44 which compares the timing of the one and two-site CD-EAM models in a serial MC simulation for a random Fe-Cr alloy at 50% composition. In

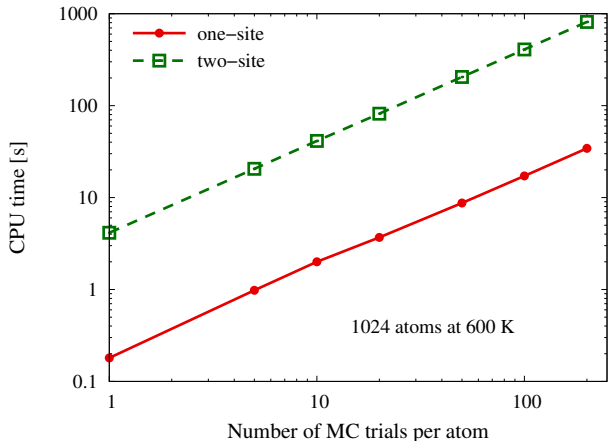

Figure 44: Comparison of the timing in a MC simulation of a Fe–Cr alloy at 50% composition. The simulation cell contained 1024 atoms.

this case the one-site CD-EAM model is twelve times faster than the two-site formulation.

Therefore, we advocate for the new one-site concentration version of the CD-EAM potential which exhibits superior performance in MD and especially MC simulations while preserving all advantages of the original (two-site) CD-EAM model. This model will enable large-scale MD and MC simulations of concentrated alloys and their complex thermodynamic and mechanical properties.

6.4 SUMMARY AND CONCLUSIONS

We have derived the analytic force expression for the concentration-dependent embedded atom method (CD-EAM) potential and have shown that the forces for this advanced many-body model can be calculated in a computationally efficient manner, at a cost which is only slightly larger than for standard EAM potentials. This facilitates the application of the CD-EAM model in large-scale molecular dynamics simulations of concentrated alloys.

The CD-EAM model in its original form is not suitable for Monte-Carlo simulations since its effective pair interaction range is twice as large as the cutoff radius of the potential function. By introducing a modification of the analytic form of the CD-EAM model it is, however, possible to reduce the effective interaction radius to be equal to the cutoff radius. This renders massively-parallel Monte-Carlo simulations based on the new CD-EAM model possible while preserving all of the qualities of the original CD-EAM model.

By combining the semi-grandcanonial Monte-Carlo (SGC-MC) method with molecular dynamics, one obtains a very powerful hybrid scheme that takes into account chemical mixing, structural relaxations, and thermal vibrations.

Energy and force calculation routines for the two-site and the new one-site CD-EAM model have been implemented into the massively-parallel molecular dynamics code LAMMPS [139] and have recently become part of the official LAMMPS distribution. The parallelized SGC-MC method has also been directly integrated into this MD code to enable the hybrid simulations presented in the next chapter.

7

NANOCRYSTALLINE ALLOYS: INTERPLAY OF GRAIN BOUNDARY SOLUTE SEGREGATION, FAULT ENERGIES AND GRAIN SIZE

7.1 INTRODUCTION

In pure metals, a grain size in the nanometer range is difficult to stabilize against grain growth even at room temperature [62, 206]. One way of lowering the driving force for grain growth is to reduce the GB energy by alloying of two or more elements. The stabilizing effect of strongly segregating solutes in nc materials has been derived theoretically [204, 86] and confirmed experimentally [43]. The amount of solutes added to the material controls the metastable grain size, above which grain growth is sufficiently suppressed. This, however, renders the independent variation of grain size and composition difficult. Accordingly, a separation of the effects of alloying and grain size on the mechanical properties of the material is difficult to achieve in experiments, being one reason why the role of solutes in the deformation processes of nc alloys is not yet fully understood.

Investigations of segregation and arrangement of impurity atoms in special grain boundaries were published by Udler and Seidman [177] in 1992, but only recently, computer simulation studies have been performed, which consider the effect of impurities [48] and solutes [76] on the mechanical properties of nanocrystalline structures. Most computational studies of binary nanocrystalline alloys focus on segregating elements, which show a lowering of the GB energy through the incorporation of solutes [76, 42, 126, 127, 128]. It was found that in strongly segregating systems, small amounts of solutes can significantly lower the GB energy, and, thereby, reduce the achievable metastable grain size [43]. Impurity drag effects [23] are an alternative stabilizing mechanism. Monk et al. [130] investigated the effect of impurity atoms at or near the GB on the response of the GB to an external stress. For example, simulations done for a symmetrical tilt boundary in bcc Fe, in which the GB migrates due to the nucleation and propagation of partial GB dislocations, demonstrated that both H and C can hinder dislocation glide and therefore migration.

Much less attention, however, has been paid to miscible solutes that in principle allow to specifically tune certain material properties: The nucleation of partial dislocations, for instance, is stimulated by miscible solutes as shown

by Rajgarhia et al. [142] in MD simulations. Alloying also affects the thermal stability of GBs and leads to a variation of the generalized planar fault energy (GPFE) of the bulk material [86, 126, 127, 128, 95, 28]. Dislocation nucleation and slip in fcc materials, in turn, depend on the GPFE [185], which also affects the twinnability of the material [10, 169, 84, 85]. In general, these characteristic energy barriers of an alloy cannot simply be predicted from the energies of the constituents. One prominent example is Al, which lowers the stacking fault energy (SFE) of Cu, even though the SFE of pure Al is higher. Schulthess et al. [152] have shown how to predict the SFE from the hcp–fcc energy difference for Al solid solutions. Morever, it is well known that the grain boundary structure and energy depend on the type and concentration of solutes [177], and, therefore, chemical equilibration of GBs should affect the mechanical properties of alloyed nanocrystals.

In view of these early, and yet unrelated findings on miscible systems, investigating the deformation behavior of nanocrystalline alloys by computer simulations can shed light on the role and interplay of the various factors that affect the deformation behavior of such samples.

In this chapter, we present molecular dynamics studies of nanocrystalline Pd–Au, with Pd and Au being fully miscible over the full concentration range. Samples of various grain sizes are constructed according to the Voronoi tessellation method, equilibrated and alloyed with the hybrid MD/Monte-Carlo scheme described in the last chapter, and finally characterized and tested in tensile straining experiments. We perform a detailed analysis of the element distribution in the nanocrystalline GB network and investigate its effect on the interplay of intergranular and intragranular deformation mechanisms. Our results are discussed in terms of the composition-dependence of defect nucleation energy barriers, planar fault energies, as well as composition and structure of the grain boundaries.

The chapter is organized as follows: We first describe the composition-dependent Pd–Au interatomic potential used throughout this work to model the alloy in atomistic simulations. Second, in sections 7.2.2 and 7.2.3, we explain the simulation procedure, preparation of the nanocrystalline samples, and their chemical and structural equilibration. These samples are subsequently characterized with respect to element distribution and deformation behavior in tensile test experiments. In the last section, we discuss the interplay between chemical GB configuration and deformation behavior.

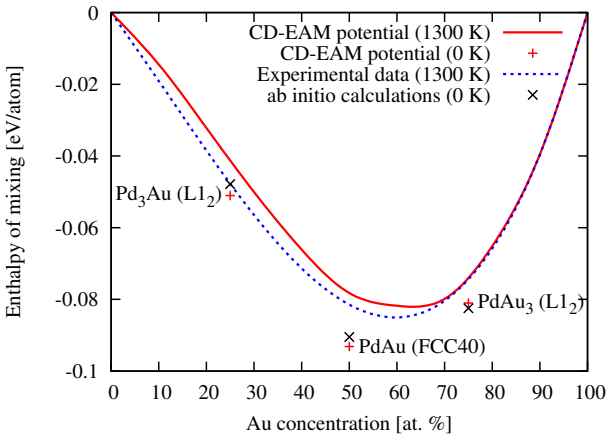

Figure 45: Enthalpy of mixing of the Pd–Au binary alloy.

7.2 METHODOLOGY

7.2.1 *Interatomic potential*

For studying the Pd–Au alloy at the atomic level, we employ the combination of MD and Monte-Carlo (MC) method introduced in the previous chapter. Pure elements are described by EAM potentials for Pd [56] and Au [6], while cross interactions follow the *concentration-dependent embedded-atom method* (CD-EAM) also described in the previous chapter. The Pd–Au binary system has a negative enthalpy of mixing over the whole compositional range and is completely miscible at higher temperatures. The CD-EAM formalism helps us to derive the cross potential V_{AB} from the experimental enthalpy of mixing curve in a very straightforward manner. In this formalism, the cross potential, $V_{AB}(x,r) = h(x)\Phi_{AB}(r)$, is composed of two parts: (i) the concentration-dependent function, $h(x)$, which is a forth-order polynomial of the local gold concentration, x, and (ii) the static cross potential, Φ_{AB}, which we choose to be the arithmetic mean of the elemental pair potentials: $\Phi_{AB} = (V_{AA} + V_{BB})/2$.

To make the EAM potentials for the pure elements compatible and to minimize nonlinear contributions of the embedding terms to the formation energy, we first normalized the Pd and Au EAM potentials to an *effective pair representation* [25] that preserves all properties of the pure elements. The five coefficients of the $h(x)$ polynomial were then determined such that the experimental enthalpy of mixing curve at 1300 K [2] is reproduced by the potential for a random solid solution (figure 45). Table 3 lists the coefficients of the $h(x)$ polynomial after fitting. The potential has exclusively

h_0	h_1	h_2	h_3	h_4
1.159085	−0.126781	0.481763	−0.488693	0.203778

Table 3: Coefficients of the 4th order polynomial $h(x) = \sum_{n=0}^{4} h_n x^n$ for the Au–Pd potential. Here, x denotes the local Au concentration ($0 \leq x \leq 1$).

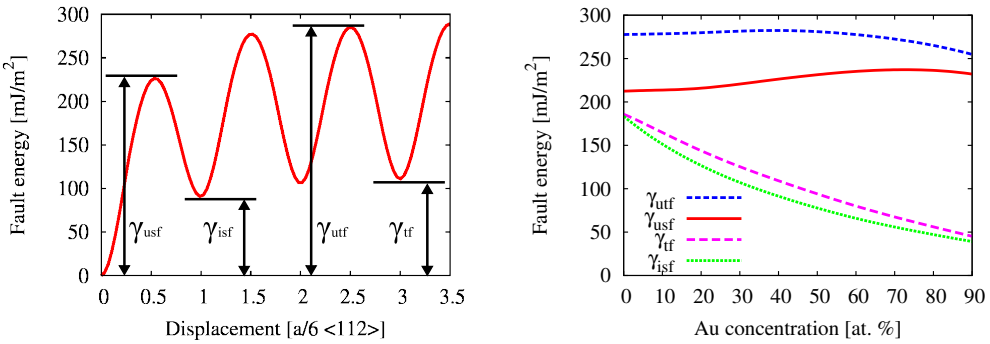

(a) (b)

Figure 46: (a) Generalized planar fault energy (GPFE) curve of Pd–Au (40%). The minima and maxima correspond to the unstable stacking fault, γ_{usf}, intrinsic stacking fault, γ_{isf}, unstable twinning fault, γ_{utf} and twinning fault, γ_{tf}, energies; (b) γ_{usf}, γ_{isf}, γ_{utf} and γ_{tf} as functions of Au concentration.

been fitted to the enthalpy of mixing of the disordered high-temperature phase of Pd–Au at 1300 K, but experimental data [133, 119] and *ab initio* calculations [33, 160, 8] indicate that several ordered phases occur at low temperatures. The formation energies of these phases, which were not part of the fitting procedure, are also properly predicted by the CD-EAM potential (see figure 45).

The EAM potentials for the pure elements yield elastic constants and stacking fault energies that are in good agreement with experimental data. Figure 46a displays the calculated generalized planar fault energy (GPFE) curve for a sample with 40% gold content. The concentration dependency of the stable and unstable fault energies as predicted by the CD-EAM potential is shown in figure 46b. Notably both, the intrinsic stacking and twinning fault energy, decrease with increasing gold content, whereas the unstable stacking and twinning fault energies only slightly vary with the Au fraction. In summary, the Pd–Au binary alloy used in this simulation study provides a way to vary the dislocation splitting distance and dislocation nucleation barriers by changing the composition.

7.2.2 *Alloying*

To model the equilibrium properties of nanocrystalline Pd–Au alloys, we utilize the previously introduced hybrid MD/MC simulation method that accounts for structural relaxations and thermal vibrations as well as exchange of atom types. One part of this technique is the transmutational Monte-Carlo scheme that samples the semi-grandcanonical ensemble, and thus allows us to determine the equilibrium concentration and element distribution in the sample for a given chemical potential difference $\Delta\mu = \mu_{Au} - \mu_{Pd}$. At the same time, we account for structural relaxations by interleaving molecular dynamics (MD) steps: After the system has been evolved for a certain number of MD steps, we carry out MC trial moves, before returning to the MD part again. The number of MD steps between MC moves as well as the number of MC trial moves can be adjusted to optimize the convergence of the simulation.

7.2.3 *Preparation of nanocrystalline model structures*

Our computational method allows us to produce samples of different compositions, while varying the grain size independently. We first created pure Pd nanocrystalline model structures with average grain sizes of 5, 10 and 15 nm consisting of 432, 128 and 54 grains, respectively. The Voronoi method (section 1.3.2) was used to set up the grain shapes based on randomly placed center points in a cubic simulation box. Three-dimensional periodic boundary conditions were applied to model a bulk structure. The lattice orientations of the grains were taken from a random isotropic distribution. To avoid spurious configurations in the as-prepared Voronoi samples, we deleted atoms from the grain boundaries that were closer than 2.0 Å to other atoms prior to relaxation.

Relaxation and alloying was performed at 600 K for 1 ns at zero pressure. During this MD run, one full MC step was performed every 40 fs, i.e., 25,000 trial moves were performed on each atom in the system on average to determine the equilibrium element distribution. The temperature parameter for the Metropolis MC algorithm was also set to 600 K as in the MD stage. At this temperature, some ordering effects in the Pd–Au solid solution have been suspected by several authors [33, 160, 8]. Indeed, we observe differences between MC equilibrated single crystals and random solid solutions in the short range order, which also affect the elastic properties.

To distinguish atoms located in grain boundaries from bulk atoms, we use the common neighbor analysis (CNA) [72]. The cutoff parameter R_{CNA} for identifying nearest neighbors was set to lie between the first and second

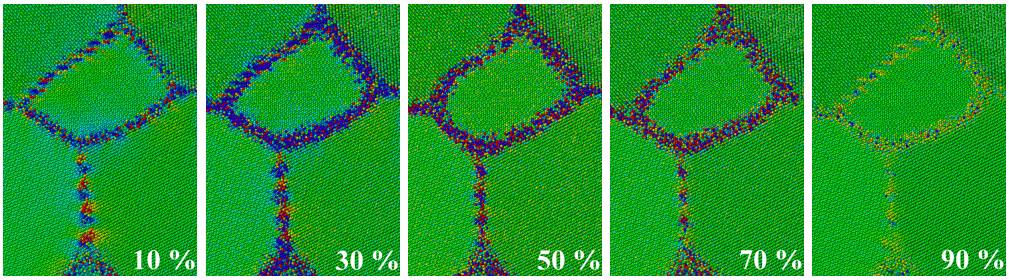

(a) (b) (c) (d) (e)

Figure 47: Cross-sections of a grain and its surrounding GBs and triple junctions for various global Au concentrations ranging from 10% to 90%. Colors indicate deviation of local concentration from global concentration (green). Blue denotes Au depletion of 10%, red denotes Au enrichment of 10%. In this context, concentration is defined as the average occupancy of a lattice site with an Au atom in the statistical semi-grandcanonical ensemble.

nearest neighbor shells: $R_{\mathrm{CNA}} = a_0(x) \cdot (1 + \sqrt{1/2})/2$, with $a_0(x)$ being the static lattice parameter for a given concentration x. For a later analysis, the local atomic volume of each atom was calculated by means of the atomic Voronoi tessellation [146] method, which divides the space between atoms into geometric regions. We define the atomic free volume of the grain boundaries to be the difference of the average atomic volume of all GB atoms and the average volume of atoms from the respective species located in the bulk.

7.2.4 *Loading*

Samples were deformed at 300 K by imposing a constant engineering strain rate of 10^8 1/s in uniaxial direction on the simulation cell. The cell size was allowed to relax perpendicular to the straining axis. To test the strain rate dependence of our results, individual runs were repeated with an engineering strain rate of 10^7 1/s.

7.3 RESULTS

7.3.1 *Structure characterization*

In a first step, the elemental distributions in the model structures relaxed by the hybrid MD/MC scheme were analyzed in order to quantify whether the grain boundary composition differs from the global concentration. At finite

temperature, however, the instantaneous element distribution is fluctuating, and therefore analyzing a single snapshot is not suitable for characterizing the local element distribution. Here, it is useful to introduce the concept of an 'effective atom' [198], which is also known as the *site occupancy* describing the average occupancy of an atomic lattice site with a given atomic species. We have thus calculated the site occupancy in the semi-grandcanonical ensemble by taking the ensemble average over a large number of MC steps. Note that the time-averaged position and occupancy of each site is expected to converge even for GBs in substitutional alloys [168].

Figure 47 shows the local site occupancy variations within the microstructure (for a sample with 15 nm average grain size). The color scale has been chosen such that a green color always corresponds to the global Au concentration, whereas blue denotes a gold depletion of -10 at.%, and red an enrichment of +10 at.%. In the grain boundaries, regions can be found where either Pd or Au is preferred. In addition, the magnitude of the variations depends on the global concentration, and the thickness of this 'deviation zone' changes with the global concentration as well. Note that the slice shown here is representative of the whole polycrystalline structure, effectively being independent of the grain boundary orientation. In particular, we obtained comparable results for various planar symmetric GBs in a bicrystal geometry.

The GB concentration has been determined by averaging the site occupancy values of all disordered GB atoms (according to the CNA). For most compositions, the GBs contain less gold than the bulk (figure 48). This finding is superimposed by the aforementioned variation in thickness of the 'depletion zone', which depends on the global solute concentration and does not coincide with the thickness of the disordered grain boundary layer. GB enrichment in nanocrystalline metals was studied computationally and experimentally also in segregating systems [43], but GB depletion in nanocrystalline miscible systems has, to our knowledge, not been reported before.

As can be seen in figure 48, the strength of the GB depletion effect depends on the grain size. This can be explained with the GB area to bulk ratio, which is smaller for large grain sizes. Then, a small excess concentration in the bulk is sufficient to balance a large depletion in the grain boundaries. Moreover, this observation is in agreement with the expectation that in the case of a very small grain size, i.e. in the amorphous limit, the material is a homogeneous phase again and all local deviations from the global composition must vanish.

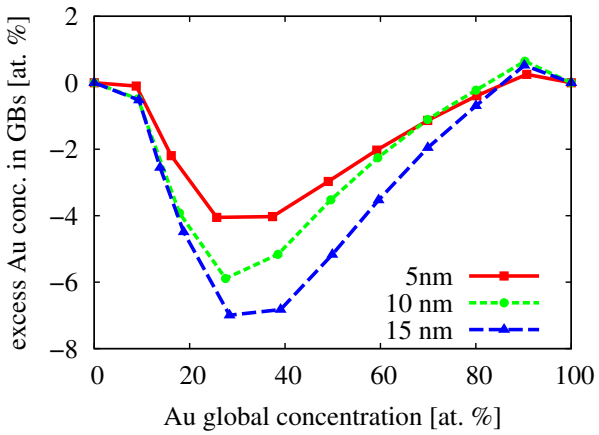

Figure 48: Average grain boundary excess concentration as a function of global concentration and grain size.

7.3.2 *Stress-strain behavior – compositional effects*

The observed stress-strain behavior of structures with two different grain sizes (5 and 15 nm) and three different concentrations (0, 10, and 40% Au) is shown in the first row of figure 49. The slope in the elastic regime is larger for the samples with increased gold concentration, which is due to the enhanced elastic modulus of the bulk crystal at intermediate compositions as predicted by the Pd–Au potential. In addition, an increasing elastic modulus of the grain boundaries by chemical relaxation contributes to this stiffening as will be shown below. The addition of gold is observed to have a strengthening effect for all grain sizes in the Pd rich regime. This is particularly pronounced for the intermediate concentrations as can be seen in figure 50a, where the maximum (ultimate tensile) stress versus composition is plotted for different grain sizes.

The stress-strain curves for the Pd–Au alloy shown in figure 49 exhibit an overshoot, which varies in height with composition. The origin of this overshoot, which –for pure metals– is usually explained by the ultra-high strain rates used in MD simulations [151], is obviously more intricate in the case of the nanocrystalline alloys. For larger grain sizes, we observe strain softening at larger deformations irrespective of composition. This effect, which is also observed in experiments [27], was explained with residual internal stresses due to nucleated and absorbed dislocations by Tang and Schoenung [170], and –for MD simulations– with the occurrence of cross slip by Brandl et al. [18]. Since isolated partial dislocations dominate in our samples, especially in Au rich alloys, the latter explanation cannot hold for our simulations.

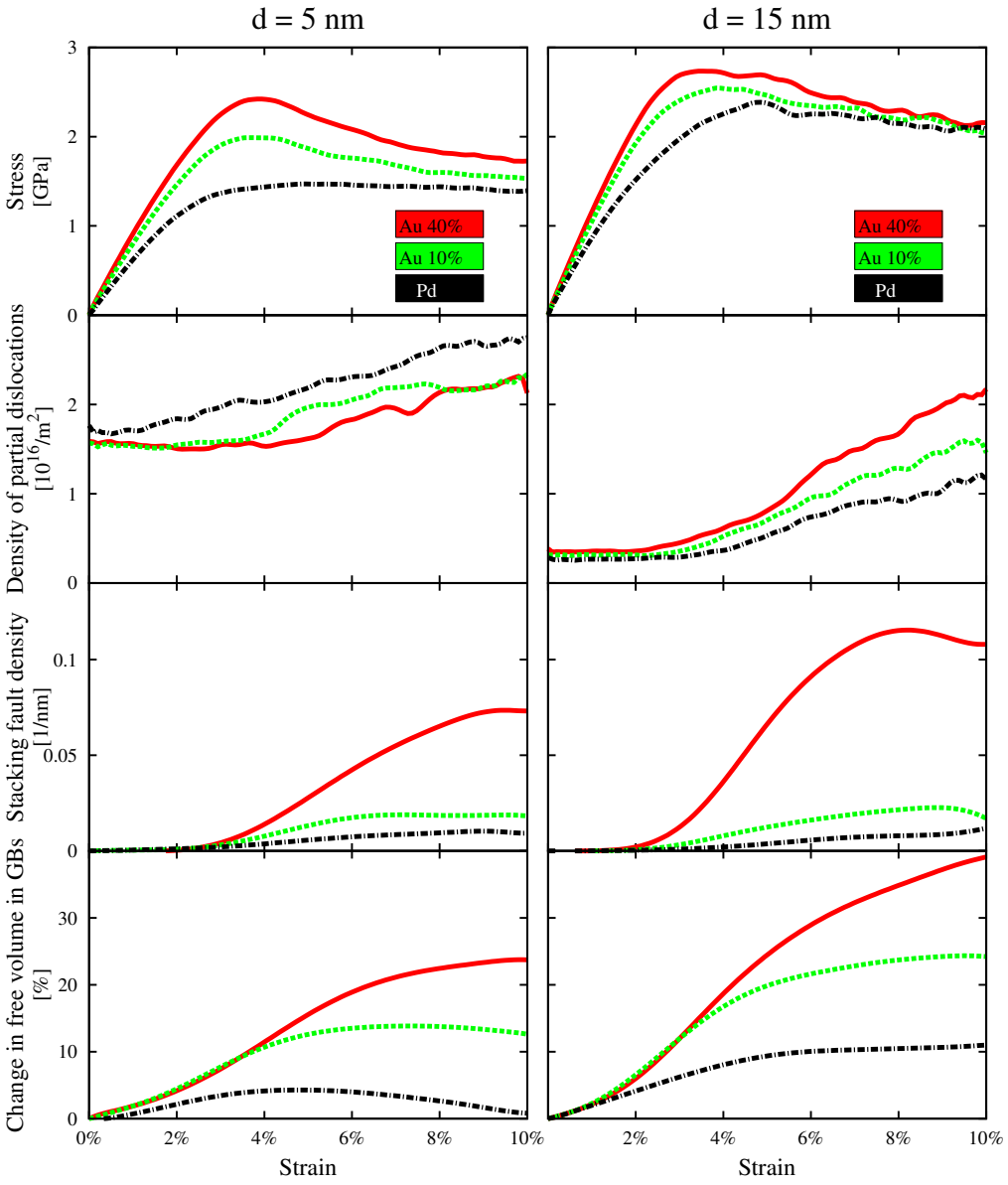

Figure 49: Compositional effects: Stress-strain behavior, partial dislocation density, stacking fault density and relative change in free volume in the GBs for two different grain sizes and three different compositions as functions of macroscopic strain.

As discussed in section 7.2.1, the stable and unstable fault energies predicted by our model potential for the Pd–Au alloy are composition-dependent. That is why we can expect the deformation mechanisms to be composition-dependent as well. To investigate this dependence, we have analyzed the activity of dislocations in the samples during deformation using the automated on-the-fly dislocation detection algorithm (ODDA) presented in chapter 4. This method allows us to monitor the dislocation lines in all grains and to determine their Burgers vector. A statistical analysis of this data gives the total dislocation density, which continuously increases during plastic deformation after dislocation nucleation from the grain boundaries has set in (second row of figure 49). Shockley partials dominate the measured dislocation density, since perfect $(a/2)\langle 110\rangle$ dislocations are in most cases resolved as two separate Shockley partials by the analysis algorithm, even for very small splitting distances. For a given strain level, one can observe an increased dislocation activity in alloys with higher Au content. This finding can be explained with the lowered dislocation resistance parameter [77, 144] for leading partial nucleation, γ_{usf}/G, at intermediate compositions (figure 50b). However, the intrinsic stacking fault energy, γ_{isf}, is lowered by the addition of gold as well. This leads to a higher resistance parameter for the nucleation of trailing partials (quantified by $(\gamma_{\mathrm{usf}} - \gamma_{\mathrm{isf}})/G$), effectively locking leading partials in the grain interior. In addition, lowering the stacking fault energy leads to a widening of intrinsic stacking faults and increases the probability of dislocation-dislocation reactions, which likely result in immobile products like stair-rod dislocation segments.

Note that dislocations constituting small-angle GBs and vicinal twin boundaries are also detected by our analysis algorithm, resulting in a considerable initial dislocation density in the 5 nm samples, which have the highest density of GBs. Unfortunately, structural changes in the GBs during deformation lead to a fluctuating GB dislocation density inhibiting the exact measurement of the dislocation density in the grain interiors. Regardless of this superimposed scatter, the 5 nm structures apparently show a less significant and less systematic increase in dislocation density. This is consistent with the general picture of a change from intragranular to intergranular mechanisms at the smallest grain sizes [217, 31, 32].

We have also measured the density of intrinsic stacking faults (ISF) and coherent twin boundaries (not shown) in the samples as functions of strain (third row of figure 49). As expected, the addition of gold leads to a strong increase in ISF density. These ISFs provide nucleation sites for Shockley partials on adjacent crystal planes, which let them first transform into extrinsic stacking faults and finally into two coherent TBs that constitute a nanoscale twin lamella.

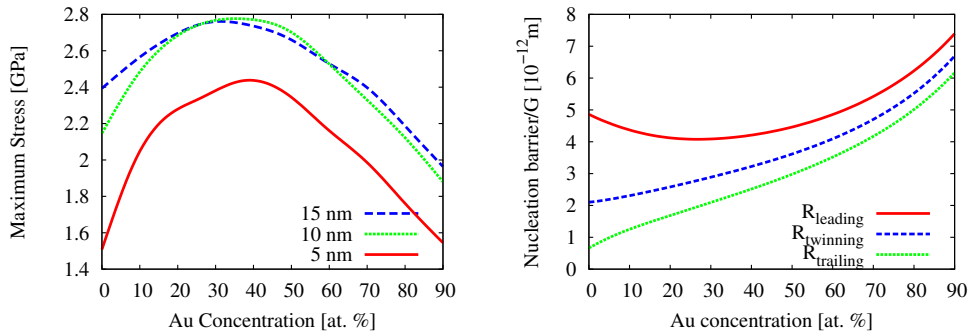

Figure 50: Compositional effects: (a) Maximum yield stress as a function of composition for different grain sizes. (b) Resistance parameters [77, 144], R, for the nucleation of leading partial dislocations, γ_{usf}/G, twinning partial dislocations, $(\gamma_{\mathrm{utf}} - \gamma_{\mathrm{tf}})/G$, and trailing partial dislocations, $(\gamma_{\mathrm{usf}} - \gamma_{\mathrm{isf}})/G$, as functions of the Au content.

To study the structural changes the GBs undergo during deformation, we measured the change in free volume in the GBs as a function of macroscopic strain. The fourth row of figure 49 shows the evolution of the excess free volume in the GBs relative to the initial value of the as-prepared samples. In pure nc-Pd, the free volume changes only slightly during deformation. In Pd–Au, in contrast, the free volume is raised considerably by GB mediated processes like sliding and random shuffling, which destroy the compact equilibrium chemical element distribution in the GBs.

7.3.3 *Re-straining and strain softening*

To assess the influence of the equilibrium element distribution in the GBs on the deformation processes in more detail, we preloaded alloy structures to 6% and 10% strain, and unloaded them before doing the actual tensile test. For the samples with 5 and 15 nm grain size with 40% gold content, the results are shown in figure 51. Since no additional equilibration was performed after the preloading step, one can assume that the GBs are more or less left in a non-equilibrium state after the first deformation pass. Since in the 5 nm sample, GB mediated deformation processes dominate, preloading to 10 % strain results in a stress-strain behavior similar to pure Pd, where the overshoot vanishes and almost no strain softening is observed. Re-straining a sample that was deformed to a lesser extent (6 %) results in a stress-strain behavior intermediate between the chemically equilibrated structure and a sample that was deformed to 10 %. Hence, a gradual destruction of the

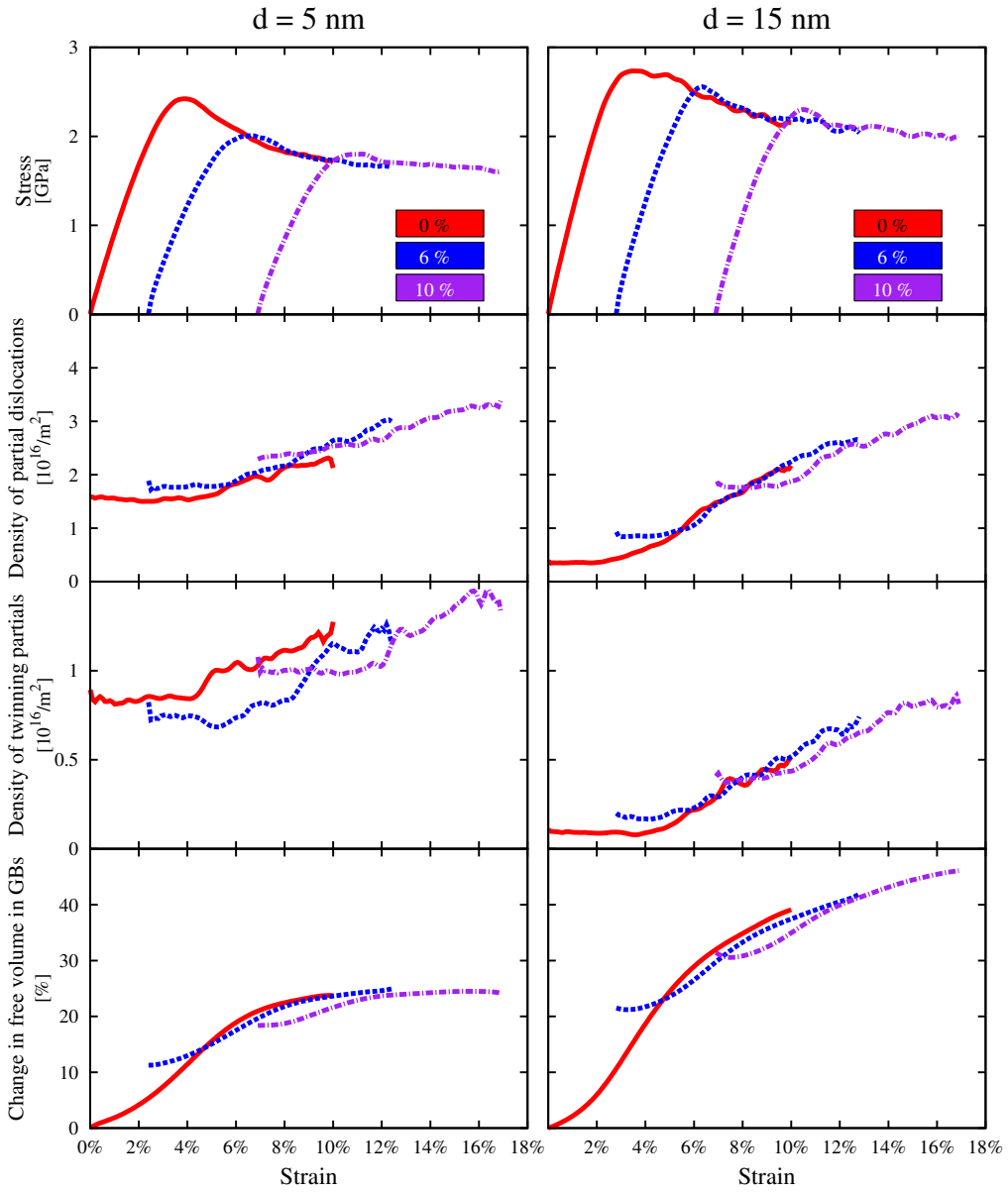

Figure 51: Restraining: Stress strain behavior, partial dislocation density, twinning partial density and relative change in free volume in the GBs for two different grain sizes and three different preloading states as a function of macroscopic strain.

equilibrated GB structure causes a lowering of the maximum flow stress. For the 5 nm sample, which deforms plastically by GB mediated processes, we can therefore reason that chemical equilibration impedes GB sliding. After the chemical order is destroyed (e.g. by a preceding deformation), the sample approaches a steady-state deformation regime where no strain softening is observed. The monitored change in free volume in the grain boundaries (figure 51, fourth row) supports this picture, where the re-strained samples converge to a constant value, suggesting a steady-state deformation mode mediated by GB processes.

For the larger grain sizes (10 and 15 nm), where intragranular deformation processes are more pronounced, the results are somewhat different (second column of figure 51). Here, the re-strained samples (after 10 % pre-strain), show a reduced maximum stress, but still considerable strain softening. This strain softening can be explained with the evolution of crystal defects within the structures. The grains within the initial, chemically equilibrated structures are free of any defects, whereas the preloaded samples already contain a significant number of planar defects and dislocations. Monitoring the dislocation activity (second row of figure 51) shows that in the 15 nm samples, the gain in dislocation density (which includes lattice Shockley partials as well as twinning partials) is more pronounced. Especially the increasing number of twinning partials can explain the observed softening of the material based on the same conclusions we made for nanotwinned Pd in chapter 5.

7.3.4 *Chemical GB relaxation*

Recently, Vo et al. [189] have shown for nc-Cu that the stress-strain behavior and the respective contributions of different deformation mechanisms not only depend on the grain size, but also on the state of GB relaxation of the sample. In order to elucidate the role of GB relaxation in the nanocrystalline alloy, we have first performed an additional mechanical cycling (loading/unloading) of three times up to 2% strain in the *elastic* regime before doing the actual tensile test. This mechanical equilibration step, in addition to the annealing treatment, however, did not change the stress-strain behavior of the sample as can be seen in figure 52.

As mentioned before, the high strain rate in the simulation is another factor that can affect the stress-strain behavior and possibly leads to an overshoot in the stress-strain curve [151]. We repeated the tensile test simulation at a reduced strain rate (10^7 1/s), but found only a slight reduction of the overshoot height (figure 52). This provides evidence that the profile of the

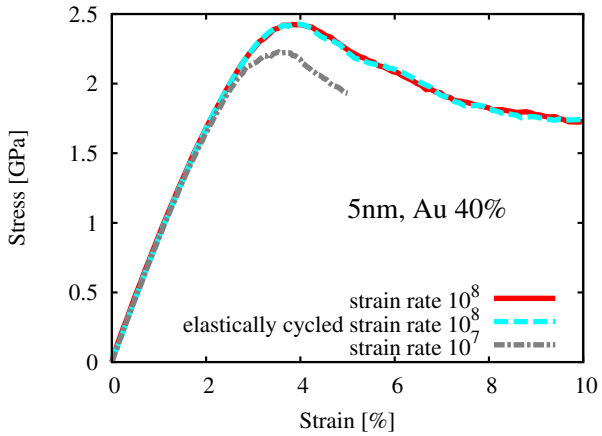

Figure 52: Strain rate effects and mechanical equilibration: Stress strain behavior of a (5 nm, 40% Au) mechanically cycled sample (3 times to 2% strain); Deformation at a lower strain rate (10^7 1/s). (The latter simulation was stopped after 5% strain.)

stress-strain curve is more influenced by the characteristics of the sample before deformation than by the suppression of thermally activated processes.

The fact that the overshoot occurs in the intermediate concentration range raises the question for its origin: Is it caused by the increased elastic modulus of the material (as predicted by the interatomic potential), or by some other property of the nanocrystalline alloy? To answer this question, we have generated nanocrystalline samples that were only structurally relaxed, but not chemically (i.e. no Monte-Carlo moves). That is, the chemical ordering and composition of the GBs was left in the as-prepared state, being a homogeneous, random solid solution similar to the bulk material. Note that this can only be done in computer simulations, and not in experiments. The summarized results are shown in figure 53.

Most interestingly, for the only structurally equilibrated samples, having a random element distribution in the GBs, the yield stress drops massively and the profile of the stress-strain curve becomes flat and similar to pure Pd (5 nm grain size in figure 53). Note again, that we have only changed the chemical structure of the GBs, but kept all other properties including the structural equilibration, global composition etc., the same. This shows that the details of the element distribution in the GBs play a crucial role for the yield strength of this miscible alloy. This is consistent with the re-straining tests (previous section), where the chemical order was destroyed by a preceding deformation and could not be restored by diffusional processes on the short timescale of the MD simulation. This observation hints to the fact that the chemical

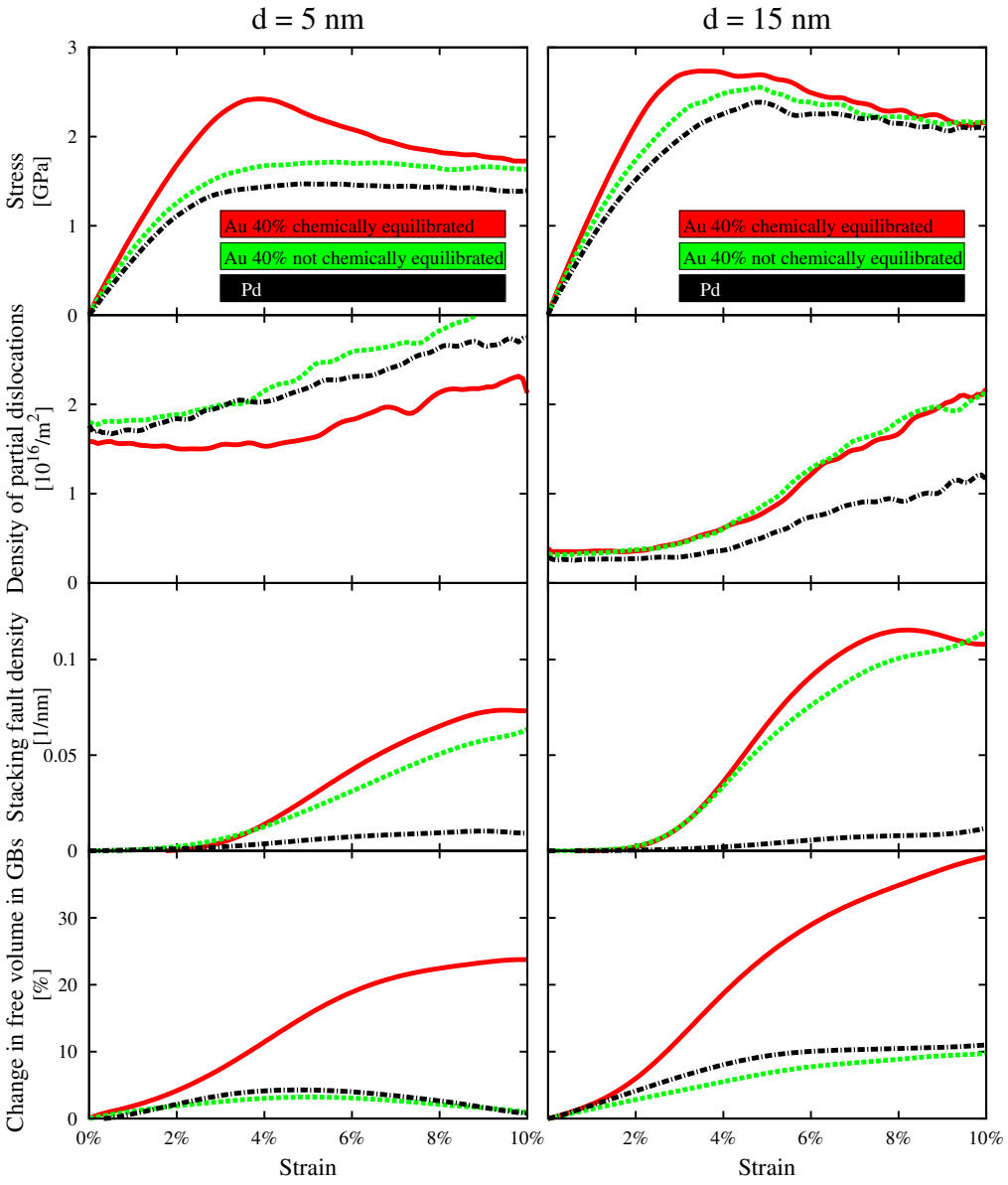

Figure 53: Effect of chemical GB relaxation: Stress-strain behavior, partial dislocation density, stacking fault density and relative change in free volume in the GBs for two different grain sizes and three different compositions as functions of macroscopic strain for samples that were only structurally equilibrated, but not with respect to the element distribution in the GBs.

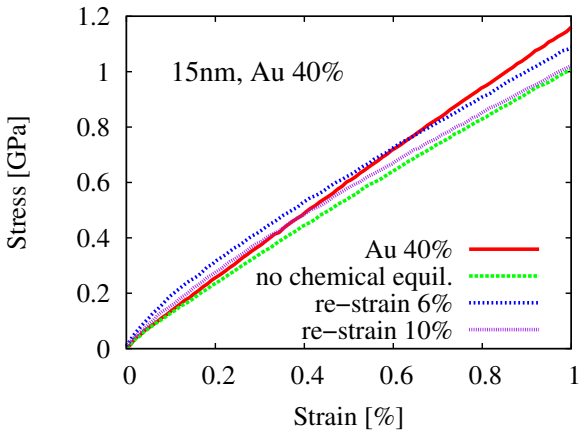

Figure 54: Modulus effect: Stress-strain behavior at small strains for different states of GB relaxation.

relaxation leads to a low energy GB configuration, being more stable against yielding than the GBs present in the random alloy.

Monitoring the free volume for the case of the only structurally equilibrated samples (figure 53, fourth row) shows, that the free volume in the GBs follows the behavior of pure Pd (which, by definition, can only be structurally equilibrated). This supports our hypothesis of a GB structure stabilized by chemical equilibration. In contrast, the dislocation activities and the number of planar faults (figure 53, rows 2 and 3) do not change. Thus, the mechanisms within the grains are not significantly affected by the chemical relaxation.

Improving the relaxation state of the GBs (e.g. by chemical equilibration) also slightly increases the modulus of the structure. To show this, we compared the elastic behavior at low strains for different structures of similar composition (figure 54). Apparently, the chemically equilibrated structure shows the highest stiffness and the smallest deviation from a perfect linear elastic behavior. Therefore, chemical equilibration can be considered to bring the GB structure into a metastable configuration having a higher resistivity to deformation. Note that the re-strained samples show a clear deviation from a perfect linear elastic behavior caused by recovery processes.

7.4 DISCUSSION

The stress-strain behavior of our model structures depends on the introduction of miscible solutes, and the distribution of these solutes plays a key role. For the case of fully equilibrated structures (figure 49) a significant

increase in stiffness and strength is achieved by alloying. This effect vanishes for samples in which the equilibrium distribution of solutes is destroyed by deformation (figure 51) and for samples, which were never chemically equilibrated at all (figure 53). The measured dislocation and ISF densities are not affected by the chemical equilibration. That is, the samples with a non-equilibrium random element distribution in the GBs show the same dislocation behavior as the fully equilibrated structures. Thus, the observed differences in the stress-strain curves between chemically equilibrated and not equilibrated samples (figure 52) must arise from changed intergranular deformation mechanisms like GB sliding. This is confirmed by the observed change in free volume in the GBs, where the fully equilibrated structures show a significant deviation from the behavior of pure Pd which is not the case for only structurally equilibrated samples.

At larger grain sizes, chemical equilibration can, however, not be the reason for the observed strain softening and cannot explain that the flow stress for the re-strained samples is lower compared to the only structurally equilibrated samples. Here, the dislocation analysis reveals that the observed differences originate from the presence of defects within the grains. Figure 51 shows how the density of twinning dislocations depends on the condition of the material. In the re-strained samples, the nucleation of twinning partials is facilitated by the pre-existing stacking and twinning faults, resulting in a softening of the material. This effect is in agreement with the findings we made for nanotwinned Pd (see chapter 5), where a large number of pre-existing twin boundaries leads to a softening of the material.

7.5 SUMMARY

We have performed molecular dynamics simulations of nanocrystalline Pd–Au alloys of various compositions and grain sizes to study the chemical structure, especially of the grain boundaries, and the mechanical properties of this alloy. The equilibrium element distribution in the nanocrystalline bulk samples has been determined with a hybrid Monte-Carlo/MD simulation scheme. Pd–Au is a fully miscible binary alloy, which is used in experiments to produce thermally stable nanocrystalline microstructures. Here, it served as a model system for a miscible alloy, in contrast to segregating alloys for which similar investigations have been published before. Elucidating the relationship between the intrinsic, composition-dependent properties of an alloy and the observed macroscopic mechanical behavior was the main goal of the present work.

We have found evidence that the element distribution in the GBs is of great importance for the strength of a nanocrystalline alloy. We conclude

that the equilibrium solute configuration in the GBs is inherently different from the random solid solution found in the grain interiors, even in the case of a completely miscible alloy. This element distribution, determined by a chemical equilibration of the GBs, raises the activation barrier for GB sliding, which is an important mode of deformation at small grain sizes. In contrast, the nucleation of dislocations is not affected by the chemical ordering in the GBs. However, the composition-dependence of planar fault energies and nucleation barriers still leads to a variation of the dislocation-based deformation mechanisms. In our measurements of the evolving dislocation density in 15 nm Pd–Au, we find an enhanced aggregation of dislocations in the grain interiors during deformation with increasing Au solute contents. But instead of strain hardening, the formation of stacking faults and coherent twin boundaries ultimately leads to a softening of the material at higher strains, because they act as additional dislocation sources.

CONCLUSIONS

In the present dissertation, structural and mechanical properties of nanocrystalline and nanotwinned metals and alloys have been investigated by means of atomistic computer simulations. In addition, several new computational methods have been developed that facilitate the analysis of simulation results.

As an integral part of this work, a new data analysis and visualization software for atomistic simulation data, the *Open Visualization Tool* (OVITO), has been developed and published for public use. It enables sophisticated analyses of large-scale atomistic simulations of solid-state materials, which have not been possible with existing tools. OVITO has been published on the website *http://www.ovito.org/*, where it has already attracted a large number of users since its publication in late 2009.

One of the first applications of this tool was to study the origins of microstrain peak broadening in x-ray diffraction experiments of nanocrystalline materials. To this end, we have devised an atomistically defined measure that quantifies the local lattice distortions contributing to reflection broadening. Our study, which also involved simulated diffraction experiments, has shown that atomic displacements, which inherently result from the reduction of the grain size of a polycrystalline solid to the nanometer scale, can be separated into (at least) two distinct types, with qualitatively different consequences for the scattering pattern. Local displacements near the grain boundaries are correlated over shorter distances, and they do not significantly affect the broadening of the Bragg reflections that underlies experimental diffraction microstrain data. This broadening arises, instead, from long-range correlated displacement fields that extend throughout the grains, and the microstrain value inferred from it provides a quantitative measure for the distortion far from the grain boundaries. The true origin of this distortion is not yet understood. Our results do confirm, however, that large microstrain values can be obtained even when there are no lattice defects besides grain boundaries. This suggests that diffraction-based strategies for inferring the dislocation density in ultrafine-grained metals may not transfer well to truly nanocrystalline materials.

The molecular dynamics simulation method has proven to be an ideal tool for studying microscopic processes of plasticity in the past. In general, snapshots from such atomistic simulations contain a wealth of information, which is difficult to exploit for two reasons: An atomistic representation of a crystalline material contains a lot of redundant information since most atoms are permanently located on regular lattice sites, and thus, do not play

a significant role for the plasticity of the material. Secondly, the atomistic representation of crystal defects provides no direct access to the important properties of these defects like the Burgers vector of a dislocation line or the geometric shape and lattice orientation of a grain. In view of this long-standing problem, which inhibited a quantitative analysis of MD simulation results, we devised two methods to reliably divide the wealth of information stored in a snapshot of an atomistic simulation into relevant and dispensable parts. The complexity of the relevant part, the crystal defects, is reduced as far as possible by transforming it into a higher-level description, which consists of continuous dislocation lines (and their Burgers vectors), stacking fault planes, and crystal defect surfaces, effectively making this data accessible for a quantitative analysis. The new analysis methods provide an unprecedented view of the dislocation processes in simulations of crystalline materials with a wide spectrum of future applications.

With the help of this on-the-fly dislocation detection method, we have studied the microscopic deformation mechanims of nanotwinned fcc metals and –in particular– have quantified the dislocation activity in this promising class of materials. We have extracted exact dislocation and stacking fault densities in nanotwinned Cu and Pd as well as in their conventional nanocrystalline counterparts as functions of strain. Our measurements agree well with experimental data on nanotwinned Cu. Nanotwinned Pd, however, having exactly the same internal structure, exhibits a softening due to the twin boundaries. To explain this softening effect of twins in Pd, we have determined the dominating type of dislocations in the material by partitioning the total dislocation density into contributions from lattice dislocations and twinning partials. We have found that the low twin migration energy barrier of Pd promotes the generation of twinning partials at twin boundary–grain boundary junctions, resulting in an increased number of dislocations on glide systems prescribed by the existing twin boundaries, and nearly irrespective of the Schmid factor. This mode of deformation effectively leads to a lack of strain hardening in nanotwinned Pd.

In the last part of the present dissertation, we have investigated the structure and mechanical behavior of the Pd–Au miscible alloy in nanocrystalline form. To enable these simulations, we first derived the analytic force expressions for the concentration-dependent embedded atom method (CD-EAM) and showed that the forces for this advanced many-body model can be calculated in a computationally efficient manner. This facilitates the application of the CD-EAM model in parallelized molecular dynamics simulations of concentrated alloys. A slight modification of the CD-EAM scheme allowed us to also employ it in hybrid molecular dynamics/semi-grandcanonial Monte-Carlo simulations, which take into account chemical mixing, structural relaxations, and thermal vibrations simultaneously. Finally we have

used these tools in simulations of nanocrystalline Pd–Au alloys of various compositions and grain sizes to elucidate the interplay of the chemical structure, especially of the grain boundaries, and the mechanical properties of this alloy. We were able to show that the element distribution in the GBs is of great importance for the strength of a nanocrystalline alloy. The equilibrium solute configuration in the GBs is inherently different from the random solid solution found in the bulk, even in the case of a completely miscible alloy. It raises the activation barrier for GB sliding, which is an important mode of deformation at small grain sizes. In contrast, the nucleation of dislocations is not affected by the chemical ordering in the GBs. However, the intrinsic composition-dependence of planar fault energies and nucleation barriers still leads to a variation of the dislocation-based deformation mechanisms. We found an enhanced aggregation of dislocations in the grain interiors during deformation at intermediate compositions. The formation of stacking faults and coherent twin boundaries ultimately leads to a softening of the material at higher strains, because they act as additional dislocation sources.

In summary, the present study has contributed to the understanding of the atomic-scale deformation mechanisms in nanostructured metals and alloys. In particular, it has resulted in the development of several powerful techniques for atomistic computer simulations and their analysis, which are well applicable to problems beyond the scope of the present dissertation.

OUTLOOK

Much of the research in dislocation physics has focused on the interaction of dislocations and their role in strain hardening – a phenomenon in which the hardness increases with continued deformation. The importance of these processes has led to the development of meso-scale simulation techniques that explicitly model the motion of dislocation lines. In three-dimensional discrete dislocation dynamics (DD) simulations [22], the dislocation network is described by line segments, each segment being associated with a certain Burgers vector, and connected to each other at nodal points. The dislocation lines are embedded in a continuum solid and linear elasticity theory is used to calculate the elastic fields that drive dislocation motion.

The MD method, which has been employed for most of the work in this thesis, and the DD method are based on two completely different data models. Note, however, that there are striking similarities between the vectorized dislocation representation produced by the dislocation detection algorithms presented in chapter 4 and the data model employed in DD simulations. With the availability of the new dislocation extraction algorithm, it seems feasible to develop a direct link between these two methods and to build up a concurrent multi-scale technique. This could allow one to combine the accurateness of the atomistic approach, which is able to model all non-linearities of the atomic interactions as well as all kinds of crystal defects like stacking faults and grain boundaries, with the efficiency of the DD method. An existing multi-scale approach, the so-called *coupled atomistic and discrete dislocation* (CADD) method, was devised a few years ago by Miller and co-workers [156]. The key idea behind the CADD method is to spatially decompose the simulation domain into a region with fully atomistic resolution and a region that is modeled as a continuum containing discrete dislocations. Both descriptions are coupled to each other at a special boundary layer that permits the seamless passage of dislocations in both directions. The CADD formulation is, however, currently limited to two-dimensional problems at zero temperature. This strong simplification was necessary to make the recognition and transfer of dislocations from the atomistic region to the continuum feasible, as dislocation lines are only point-like entities in such a two-dimensional description. However, the reduction of dislocations to zero-dimensional entities in a model suppresses many important phenomena observed in real dislocations behavior such as the formation of junctions and multiplication effects. The development of the dislocation detection method in this thesis is a pivotal element toward a

three-dimensional version of the CADD method that enables a simultaneous simulation of complete dislocation loops on two length scales.

The conversion from an atomistic model to a line representation of dislocations now also allows us to establish a direct link between atomistics and continuum mechanics models (e.g. strain gradient theories of plasticity). As outlined in Ref. [20], this coupling can be achieved through the *dislocation density tensor*. Given a representative volume element V, the dislocation density tensor $\mathbf{A}$ is defined as an integral over all infinitesimal line segments $\mathrm{d}\boldsymbol{l}$ contained in the volume element and their respective Burgers vectors $\boldsymbol{b}$:

$$\mathbf{A} = \frac{1}{V} \oint\limits_{\perp \text{ in } V} \mathrm{d}\boldsymbol{l} \otimes \boldsymbol{b}. \tag{7.1}$$

It is straightforward to calculate this quantity from the data obtained by the dislocation detection algorithms and could, for some applications, provide a way to cross-check continuum simulations of plasticity with atomistic simulations.

Realistic simulations of nanocrystalline materials require large three-dimensional model structures with a statistically significant number of grains. Such microstructures can be subject to significant changes during a simulation due to, for instance, plastic slip and twinning, grain sliding and rotation, or annealing and grain growth. Usually, a simple visualization of the atomic positions is not sufficient to reveal the evolving three-dimensional microstructure, or to make it accessible for a quantitative analysis. Therefore it is of interest to develop a computational method that allows to extract the geometric grain shapes and boundaries from an instantaneous snapshot of the simulation. In addition to shape and volume, such an algorithm would provide lattice orientation, deformation state, and elastic strain fields for each grain. With such a tool at hand, quantitative microstructural information, e.g., the grain size or the grain boundary angle distributions, could be obtained on-the-fly during the course of a simulation. Together with the dislocation analysis, which yields data on the activated slip systems in the polycrystal, a comprehensive description of the microstructure state and the ongoing processes would become available. Furthermore, these data –now detached from the underlying atomistic model and translated into a more compact form– can be used for a further quantitative assessment or the development of constitutive models.

The development of such advanced analysis tools will require the application of sophisticated algorithms from other fields of science. The decomposition of an atomistic bulk structure into individual grains can be performed with image segmentation algorithms developed for computer vision applica-

tions [52]. Such techniques must be extended into three dimensions as it has already been done for medical imaging analyses.

Improving the level of realism of the mesoscopic DD models by incorporating the concept of inhomogeneous nucleation and absorption of dislocations at the grain boundaries is a great challenge. To achieve this goal, a dislocation nucleation criterion must be derived from atomistic simulations. Efforts to study the conditions of homogeneous nucleation of dislocations in singlecrystals have already been made [176], and will have to be extended to dislocation nucleation at grain boundaries and triple junctions. The possibility to detect emerging dislocations in MD simulations, created by the presented methods, is the first step to correlate these dislocation nucleation events to the material state at the nucleation site. Building on the detailed analysis techniques described in this thesis, the relevant features that may have an influence on the nucleation, like the local stress and strain state, grain boundary orientations and triple junctions, could be resolved and be used for a statistical analysis. The development of a dislocation nucleation criterion is not only important for advancing DD simulation models but of fundamental importance for understanding plastic deformation at small scales and the formulation of materials models.

ERKLÄRUNG – DISCLAIMER

Die vorliegende Arbeit wurde im Zeitraum von März 2007 bis April 2010 im Fachgebiet Materialmodellierung am Institut für Materialwissenschaft der Technischen Universität Darmstadt bei Herrn Prof. Dr. rer. nat. Karsten Albe angefertigt.

Hiermit versichere ich an Eides statt, dass ich die vorliegende Arbeit selbstständig und nur unter Verwendung der angegebenen Hilfsmittel angefertigt habe. Von mir wurde weder an der Technischen Universität Darmstadt noch an einer anderen Hochschule ein Promotionsversuch unternommen.

Darmstadt, den 11. Mai 2010

Alexander Stukowski

DANKSAGUNG – ACKNOWLEDGMENTS

Während der Erstellung der vorliegenden Dissertation als auch meiner Arbeit als Wissenschaftlicher Mitarbeiter an der TU Darmstadt wurde ich von einer Reihe von Menschen unterstützt. Inbesondere möchte ich Professor Karsten Albe für das mir entgegengebrachte Vertrauen und seine fortwährende Unterstützung danken. Die von ihm geleitete Arbeitsgruppe bot ein optimales Umfeld für meine Forschungsarbeit.

Herrn Professor Horst Hahn möchte ich für die Begutachtung meiner Arbeit danken.

Bei meinen Kollegen aus dem Fachgebiet Materialmodellierung bedanke ich mich herzlich für die überaus angenehme Zeit, die wir miteinander verbracht haben. Dies gilt auch für die Mitglieder des Gemeinschaftlabors Nanomaterialien und Renate Hernichel, die zudem eine große Hilfe in vielen organisatorischen Dingen war.

Meiner Frau Sabrina danke ich für die unermüdliche Unterstützung, Geduld und Liebe, die sie mir während der ganzen Zeit zuteil werden lies. Ihre Anteilnahme an den Fortschritten und Rückschlägen in der Promotionszeit bedeuten mir viel. Auch meinen Eltern bin ich für ihre vielfältige Unterstützung während meiner Promotion zu Dank verpflichtet.

I am very grateful to the people from the Condensed Matter and Materials Division at Lawrence Livermore National Laboratory for their hospitality during my stay in Livermore. In particular Paul Erhart, Babak Sadigh, and Alfredo Caro supported me in my work described in chapter 6.

Jürgen Markmann, der die virtuellen Diffraktogramme erstellt und ausgewertet hat, und Jörg Weißmüller waren an der Arbeit zu Kapitel 3 beteiligt. Ihnen gilt mein Dank ebenso wie allen anderen Mitgliedern der Forschergruppe DFG714, mit denen ich zusammenarbeiten durfte.

Jonathan Schäfer danke ich für die erfolgreiche Zusammenarbeit. Er war maßgeblich an den Arbeiten zu Kapitel 7 mit beteiligt. Meine Kollegin Yvonne Ritter hat mich bei der Endkorrektur der Dissertation hilfreich unterstützt.

Die vorliegende Arbeit wurde finanziert von der Deutschen Forschungsgemeinschaft durch die Forschergruppe DFG714, 'Plastizität in Nanokristallinen Metallen und Legierungen'. Die Zusammenarbeit mit dem Lawrence Livermore National Laboratory wurde durch ein Doktorandenstipendium des Deutschen Akademischen Austauschdienstes ermöglicht. Rechenzeit wurde gewährt durch das Forschungszentrum Jülich, das Center for Scientific Computing der Goethe Universität Frankfurt und das D-Grid Projekt des

Bundesministeriums für Bildung und Forschung (bwGRiD an der Universität Mannheim).

CURRICULUM VITAE

Education

Diploma in Physics (*Dipl.-Phys.*), February 2007
Technische Universität Darmstadt, Germany

High School Graduation (*Abitur*), June 2000
Justus-Liebig-Schule, Darmstadt, Germany

Research experience

Visiting scientist (6 months), 2008–2009
Chemistry, Materials, Earth and Life Sciences Directorate
Lawrence Livermore National Laboratory, USA

Research scientist, PhD student, since March 2007
Materials Modeling Division, Institute of Materials Science,
Technische Universität Darmstadt, Germany

Research assistant (12 months), 2006
Institute of Materials and Mechanics in Civil Engineering (IWMB),
Technische Universität Darmstadt, Germany

Research assistant (6 months), 2005
Institute of Applied Physics,
Technische Universität Darmstadt, Germany

Publications based on the present dissertation

1. A. Stukowski and K. Albe, *Extracting dislocations and non-dislocation crystal defects from atomistic simulation data*, submitted to Modelling Simul. Mater. Sci. Eng.
2. A. Stukowski, K. Albe and D. Farkas, *Nanotwinned fcc metals: strengthening vs. softening mechanisms*, submitted to Phys. Rev. B.
3. A. Stukowski and K. Albe, *Dislocation detection algorithm for atomistic simulations*, Modelling Simul. Mater. Sci. Eng. **18**, 025016 (2010).
4. A. Stukowski, *Visualization and analysis of atomistic simulation data with OVITO – The Open Visualization Tool*, Modelling Simul. Mater. Sci. Eng. **18**, 015012 (2010).
5. A. Stukowski, B. Sadigh, P. Erhart and A. Caro, *Efficient implementation of the concentration-dependent embedded atom method for molecular-dynamics and Monte-Carlo simulations*, Modelling Simul. Mater. Sci. Eng. **7**, 075005 (2009).
6. A. Stukowski, J. Markmann, J. Weissmüller und K. Albe, *Atomistic origin of microstrain broadening in diffraction data of nanocrystalline solids*, Acta Mat. **57**, p. 1648 (2009).

   Proceedings:

7. K. Albe, A. Stukowski, J. Schäfer, Y. Ritter, and D. Farkas, *Deformation Processes in Nanostructured Metals and Alloys*, Proceedings of the NIC Symposium, FZ Jülich, Germany (2010).
8. J. Markmann, V. Yamakov, A. Stukowski, K. Albe and J. Weissmüller, *Intrinsic microstrain in nanocrystalline metals*, TMS Proceedings, 137th Annual Meeting, Materials Properties and Processing, 175 (2008).

   In preparation:

9. J. Schäfer, A. Stukowski and K. Albe, *Simulations of plasticity of nc-PdAu alloys: On the relationship between chemical grain boundary ordering and strength*

Other publications

1. A. Caro, A. Stukowski, J. Hetherly, M. Caro, S. Srivilliputhur, L. Zepeda-Ruiz, P. Erhart, and B. Sadigh, *Growth mechanism of Helium bubbles in Fe and FeCr alloys*, submitted to Phys. Rev. B.
2. B. Sadigh, P. Erhart, A. Stukowski and A. Caro, *Composition-dependent interatomic potentials: A systematic approach to modelling multicomponent alloys*, Philos. Mag. **89**, p. 3371 (2009).

3. B. Eidel and A. Stukowski, *A variational formulation of the quasicontinuum method based on energy sampling in clusters*, J. Mech. Phys. Solids **57**, p. 87 (2009).
4. B. Eidel and A. Stukowski, *A novel quasicontinuum method for the seamless transition from atomistic to continuum length scales and its application to nanoindentation of single-crystalline materials*, Proceedings in Applied Mathematics and Mechanics **7**, 4080007 (2007).
5. A. Stukowski and B. Eidel, *Atomistic to continuum scale transition for crystalline materials – a comparative study of quasicontinuum approaches*, Proceedings of Third International Conference on Multiscale Materials Modeling, Freiburg, Germany (2006).

BIBLIOGRAPHY

[1] XYZ file format specification.
http://en.wikipedia.org/wiki/XYZ_file_format.

[2] *Landolt–Börnstein*, volume Group IV Physical Chemistry, chapter Binary Systems, pages 283–286. Springer Berlin Heidelberg, 2002.

[3] F. F. Abraham, R. Walkup, H. Gao, M. Duchaineau, T. Diaz De La Rubia, and M. Seager. Simulating materials failure by using up to one billion atoms and the world's fastest computer: Work-hardening. *Proc. Natl. Acad. Sci. U. S. A.*, 99(9):5783–5787, 2002.

[4] G. J. Ackland and A. P. Jones. Applications of local crystal structure measures in experiment and simulation. *Phys. Rev. B*, 73(5):054104, 2006.

[5] G. J. Ackland and S. K. Reed. Two-band second moment model and an interatomic potential for caesium. *Phys. Rev. B*, 67(17):174108, 2003.

[6] G. J. Ackland, G. Tichy, V. Vitek, and M. W. Finnis. Simple N-body potentials for the noble metals and nickel. *Philos. Mag. A*, 56(6):735–756, 1987.

[7] R. J. Asaro, P. Krysl, and B. Kad. Deformation mechanism transitions in nanoscale fcc metals. *Philos. Mag. Lett.*, 83(12):733–743, 2003.

[8] I. Atanasov and M. Hou. Equilibrium ordering properties of Au-Pd alloys and nanoalloys. *Surf. Sci.*, 603(16):2639–2651, 2009.

[9] H. J. C. Berendsen, J. P. M. Postma, W. F. van Gunsteren, A. DiNola, and J. R. Haak. Molecular dynamics with coupling to an external bath. *J. Chem. Phys.*, 81(8):3684–3690, 1984.

[10] N. Bernstein and E. B. Tadmor. Tight-binding calculations of stacking energies and twinnability in fcc metals. *Phys. Rev. B*, 69(9):094116, 2004.

[11] E. Bitzek, C. Brandl, P. M. Derlet, and H. Van Swygenhoven. Dislocation cross-slip in nanocrystalline fcc metals. *Phys. Rev. Lett.*, 100(23):235501, 2008.

[12] E. Bitzek, P. M. Derlet, P. M. Anderson, and H. Van Swygenhoven. The stress-strain response of nanocrystalline metals: A statistical analysis of atomistic simulations. *Acta Mat.*, 56(17):4846–4857, 2008.

[13] G. Bonny, P. Erhart, A. Caro, R. C. Pasianot, L. Malerba, and M. Caro. The influence of short range order on the thermodynamics of Fe-Cr alloys. *Model. Simul. Mater. Sci. Eng.*, 17:025006, 2009.

[14] G. Bonny, R. C. Pasianot, and L. Malerba. Interatomic potentials for alloys: Fitting concentration dependent properties. *Philos. Mag.*, 89(8):711–725, 2009.

[15] G. Bonny, D. Terentyev, L. Malerba, and D. Van Neck. Early stages of alpha-alpha' phase separation in Fe-Cr alloys: An atomistic study. *Phys. Rev. B*, 79(10):104207, 2009.

[16] F. Boscherini, S. de Panfilis, and J. Weissmüller. Determination of local structure in nanophase palladium by x-ray-absorption spectroscopy. *Phys. Rev. B*, 57(6):3365–, 1998.

[17] E.A. Brandes and G.B. Brook. *Smithells Metals Reference Book*. Butterworth–Heinemann, 7th edition, 1992.

[18] C. Brandl, P. M. Derlet, and H. Van Swygenhoven. Strain rates in molecular dynamics simulations of nanocrystalline metals. *Philos. Mag.*, 89(34):3465–3475, 2009.

[19] S. Brandstetter, P. M. Derlet, S. Van Petegem, and H. Van Swygenhoven. Williamson-Hall anisotropy in nanocrystalline metals: X-ray diffraction experiments and atomistic simulations. *Acta Mat.*, 56(2):165–176, 2008.

[20] M. J. Buehler, A. Hartmaier, H. Gao, M. Duchaineau, and F. F. Abraham. Atomic plasticity: description and analysis of a one-billion atom simulation of ductile materials failure. *Comput. Meth. Appl. Mech. Eng.*, 193(48-51):5257–5282, 2004.

[21] V. V. Bulatov and W. Cai. *Computer Simulations of Dislocations*, chapter 3.3, page 63. Oxford University Press, 2006.

[22] V. V. Bulatov and W. Cai. *Computer Simulations of Dislocations*. Oxford University Press, 2006.

[23] J. W. Cahn. The impurity-drag effect in grain boundary motion. *Acta Metallurgica*, 10(9):789–798, 1962.

[24] A. J. Cao and Y. G. Wei. Molecular dynamics simulation of plastic deformation of nanotwinned copper. *J. Appl. Phys.*, 102(8):083511, 2007.

[25] A. Caro, M. Caro, E. M. Lopasso, and D. A. Crowson. Implications of ab initio energetics on the thermodynamics of Fe–Cr alloys. *Appl. Phys. Lett.*, 89(12):121902, 2006.

[26] A. Caro, D. A. Crowson, and M. Caro. Classical many-body potential for concentrated alloys and the inversion of order in iron-chromium alloys. *Phys. Rev. Lett.*, 95(7):075702, 2005.

[27] Y. Champion, C. Langlois, S. Guerin-Mailly, P. Langlois, J. L. Bonnentien, and M. J. Hytch. Near-perfect elastoplasticity in pure nanocrystalline copper. *Science*, 300(5617):310–311, 2003.

[28] I. S. Choi, R. Schwaiger, L. Kurmanaeva, and O. Kraft. On the effect of Ag content on the deformation behavior of ultrafine-grained Pd-Ag alloys. *Scr. Mater.*, 61(1):64–67, 2009.

[29] A.H. Chokshi, A. Rosen, J. Karch, and H. Gleiter. On the validity of the Hall-Petch relationship in nanocrystalline materials. *Scripta Metallurgica*, 23(10):1679–1683, 1989.

[30] F. Cleri and V. Rosato. Tight-binding potentials for transition metals and alloys. *Phys. Rev. B*, 48(1):22–33, 1993.

[31] H. Conrad and J. Narayan. Mechanism for grain size softening in nanocrystalline Zn. *Appl. Phys. Lett.*, 81(12):2241–2243, 2002.

[32] H. Conrad and J. Narayan. Mechanisms for grain size hardening and softening in Zn. *Acta Mat.*, 50(20):5067–5078, 2002.

[33] S. Curtarolo, D. Morgan, and G. Ceder. Accuracy of ab initio methods in predicting the crystal structures of metals: A review of 80 binary alloys. *Calphad*, 29(3):163–211, 2005.

[34] F. Dalla Torre, H. Van Swygenhoven, and M. Victoria. Nanocrystalline electrodeposited Ni: microstructure and tensile properties. *Acta Mat.*, 50(15):3957–3970, 2002.

[35] M. Dao, L. Lu, R. J. Asaro, J. T. M. De Hosson, and E. Ma. Toward a quantitative understanding of mechanical behavior of nanocrystalline metals. *Acta Mat.*, 55(12):4041–4065, 2007.

[36] M. Dao, L. Lu, Y. F. Shen, and S. Suresh. Strength, strain-rate sensitivity and ductility of copper with nanoscale twins. *Acta Mat.*, 54(20):5421–5432, 2006.

[37] M. S. Daw and M. I. Baskes. Semiempirical, quantum mechanical calculation of hydrogen embrittlement in metals. *Phys. Rev. Lett.*, 50(17):1285, 1983.

[38] M. S. Daw and M. I. Baskes. Embedded-atom method: Derivation and application to impurities, surfaces, and other defects in metals. *Phys. Rev. B*, 29(12):6443, 1984.

[39] M. de Koning, W. Cai, and V. V. Bulatov. Anomalous dislocation multiplication in fcc metals. *Phys. Rev. Lett.*, 91(2):025503, 2003.

[40] Department of Energy (DOE) Advanced Simulation and Computing Initiative (ASCI). VisIt software.

[41] P. M. Derlet, S. Van Petegem, and H. Van Swygenhoven. Calculation of x-ray spectra for nanocrystalline materials. *Phys. Rev. B*, 71(2):024114, 2005.

[42] A. J. Detor and C. A. Schuh. Grain boundary segregation, chemical ordering and stability of nanocrystalline alloys: Atomistic computer simulations in the Ni-W system. *Acta Mat.*, 55(12):4221–4232, 2007.

[43] A. J. Detor and C. A. Schuh. Tailoring and patterning the grain size of nanocrystalline alloys. *Acta Mat.*, 55(1):371–379, 2007.

[44] I. L. Dillamore and R. E. Smallman. The stacking-fault energy of f.c.c. metals. *Phil. Mag.*, 12(115):191, 1965.

[45] J. A. Eastman, M. R. Fitzsimmons, and L. J. Thompson. The thermal properties of nanocrystalline Pd from 16 to 300 K. *Philos. Mag. B*, 66(5):667–696, 1992.

[46] F. Ebrahimi, Q. Zhai, and D. Kong. Deformation and fracture of electrodeposited copper. *Scripta Materialia*, 39(3):315–321, July 1998.

[47] B. Eidel and A. Stukowski. A variational formulation of the quasicontinuum method based on energy sampling in clusters. *J. Mech. Phys. Solids*, 57(1):87–108, 2009.

[48] A. Elsener, O. Politano, P. M. Derlet, and H. Van Swygenhoven. Variable-charge method applied to study coupled grain boundary migration in the presence of oxygen. *Acta Mat.*, 57(6):1988–2001, 2009.

[49] F. Ercolessi and J. B. Adams. Interatomic potentials from first-principles calculations: The force-matching method. *Europhys. Lett.*, 26(8):583, 1994.

[50] P. Erhart, A. Caro, M. Caro, and B. Sadigh. Short-range order and precipitation in Fe-rich Fe–Cr alloys: Atomistic off-lattice Monte-Carlo simulations. *Phys. Rev. B*, 77(13):134206, 2008.

[51] D. Farkas and L. Patrick. Tensile deformation of fcc Ni as described by an EAM potential. *Philos. Mag.*, 89(34):3435–3450, 2009.

[52] P. Felzenszwalb and D. Huttenlocher. Efficient graph-based image segmentation. *Int. J. Comput. Vis.*, 59(2):167–181, 2004.

[53] M. W. Finnis and J. E. Sinclair. A simple empirical N-body potential for transition metals. *Philos. Mag. A*, 50(1):45–55, 1984.

[54] S. M. Foiles and J. B. Adams. Thermodynamic properties of fcc transition metals as calculated with the embedded-atom method. *Phys. Rev. B*, 40(9):5909, 1989.

[55] S. M. Foiles, M. I. Baskes, and M. S. Daw. Embedded-atom-method functions for the fcc metals Cu, Ag, Au, Ni, Pd, Pt, and their alloys. *Phys. Rev. B*, 33(12):7983, 1986.

[56] S. M Foiles and J. J. Hoyt. Computer simulation of bubble growth in metals due to He. Technical report, Sandia National Laboratories, 2001.

[57] A. G. Froseth, P. M. Derlet, and H. Van Swygenhoven. Grown-in twin boundaries affecting deformation mechanisms in nc-metals. *Appl. Phys. Lett.*, 85(24):5863–5865, 2004.

[58] A. G. Froseth, P. M. Derlet, and H. Van Swygenhoven. Vicinal twin boundaries providing dislocation sources in nanocrystalline Al. *Scr. Mater.*, 54(3):477–481, 2006.

[59] A. G. Froseth, H. Van Swygenhoven, and P. M. Derlet. The influence of twins on the mechanical properties of nc-Al. *Acta Mat.*, 52(8):2259–2268, 2004.

[60] H. Gleiter. Nanocrystalline materials. *Prog. Mater. Sci.*, 33(4):223–315, 1989.

[61] D. Gross and M. Li. Constructing microstructures of poly- and nanocrystalline materials for numerical modeling and simulation. *Appl. Phys. Lett.*, 80(5):746–748, 2002.

[62] B. Gunther, A. Kumpmann, and H. D. Kunze. Secondary recrystallization effects in nanostructured elemental metals. *Scripta Metallurgica Et Materialia*, 27(7):833–838, 1992.

[63] E. Haines. *Graphics Gems IV*, chapter Point in Polygon Strategies, pages 24–46. Academic Press, 1994.

[64] J. Hartford, B. von Sydow, G. Wahnström, and B. I. Lundqvist. Peierls barriers and stresses for edge dislocations in Pd and Al calculated from first principles. *Phys. Rev. B*, 58(5):2487, 1998.

[65] C. S. Hartley and Y. Mishin. Characterization and visualization of the lattice misfit associated with dislocation cores. *Acta Mat.*, 53(5):1313–1321, 2005.

[66] A. J. Haslam, D. Moldovan, V. Yamakov, D. Wolf, S. R. Phillpot, and H. Gleiter. Stress-enhanced grain growth in a nanocrystalline material by molecular-dynamics simulation. *Acta Mat.*, 51(7):2097–2112, 2003.

[67] A. J. Haslam, V. Yamakov, D. Moldovan, D. Wolf, S. R. Phillpot, and H. Gleiter. Effects of grain growth on grain-boundary diffusion creep by molecular-dynamics simulation. *Acta Mat.*, 52(7):1971–1987, 2004.

[68] J. P. Hirth and J. Lothe. *Theory of Dislocations*. Wiley, New York, 2nd edition, 1982.

[69] A. M. Hodge, Y. M. Wang, and T. W. Barbee, Jr. Large-scale production of nano-twinned, ultrafine-grained copper. *Mater. Sci. Eng. A*, 429(1-2):272–276, 2006.

[70] A.M. Hodge, Y.M. Wang, and T.W. Barbee Jr. Mechanical deformation of high-purity sputter-deposited nano-twinned copper. *Scr. Mater.*, 59(2):163–166, 2008.

[71] P. Hohenberg and W. Kohn. Inhomgeneous electron gas. *Phys. Rev. B*, 136(3B):B864, 1964.

[72] J. D. Honeycutt and H. C. Andersen. Molecular dynamics study of melting and freezing of small Lennard-Jones clusters. *J. Phys. Chem.*, 91(19):4950–4963, 1987.

[73] J. Y. Huang, Y. T. Zhu, H. Jiang, and T. C. Lowe. Microstructures and dislocation configurations in nanostructured Cu processed by repetitive corrugation and straightening. *Acta Mat.*, 49(9):1497–1505, 2001.

[74] D. Hull and D. J. Bacon. *Introduction to Dislocations*. Butterworth–Heinemann, 4th edition, 2001.

[75] W. Humphrey, A. Dalke, and K. Schulten. VMD – Visual Molecular Dynamics. *Journal of Molecular Graphics*, 14:33–38, 1996. http://www.ks.uiuc.edu/Research/vmd/.

[76] S. Jang, Y. Purohit, D. L. Irving, C. Padgett, D. Brenner, and R. O. Scattergood. Influence of Pb segregation on the deformation of nanocrystalline Al: Insights from molecular simulations. *Acta Mat.*, 56(17):4750–4761, 2008.

[77] Z.-H. Jin, P. Gumbsch, K. Albe, E. Ma, K. Lu, H. Gleiter, and H. Hahn. Interactions between non-screw lattice dislocations and coherent twin boundaries in face-centered cubic metals. *Acta Mat.*, 56(5):1126–1135, 2008.

[78] Z.-H. Jin, P. Gumbsch, E. Ma, K. Albe, K. Lu, H. Hahn, and H. Gleiter. The interaction mechanism of screw dislocations with coherent twin boundaries in different face-centred cubic metals. *Scr. Mater.*, 54(6):1163–1168, 2006.

[79] I. T. Jolliffe. *Principal Component Analysis*. Springer, NY, 2nd edition, 2002.

[80] K. Kadau, P. Lomdahl, B. Holian, T. Germann, D. Kadau, P. Entel, D. Wolf, M. Kreth, and F. Westerhoff. Molecular-dynamics study of mechanical deformation in nano-crystalline aluminum. *Metall. Mater. Trans. A*, 35(9):2719–2723, 2004.

[81] M. H. Kalos and P. A. Whitlock. *Monte Carlo methods*, volume 1: basics. New York: Wiley-Interscience, 1986.

[82] P. Keblinski, D. Wolf, S. R. Phillpot, and H. Gleiter. Structure of grain boundaries in nanocrystalline palladium by molecular dynamics simulation. *Scr. Mater.*, 41(6):631–636, 1999.

[83] C. L. Kelchner, S. J. Plimpton, and J. C. Hamilton. Dislocation nucleation and defect structure during surface indentation. *Phys. Rev. B*, 58(17):11085, 1998.

[84] S. Kibey, J. B. Liu, D. D. Johnson, and H. Sehitoglu. Predicting twinning stress in fcc metals: Linking twin-energy pathways to twin nucleation. *Acta Mat.*, 55(20):6843–6851, 2007.

[85] S. A. Kibey, L. L. Wang, J. B. Liu, H. T. Johnson, H. Sehitoglu, and D. D. Johnson. Quantitative prediction of twinning stress in fcc alloys: Application to Cu-Al. *Phys. Rev. B*, 79(21):214202, 2009.

[86] R. Kirchheim. Grain coarsening inhibited by solute segregation. *Acta Mat.*, 50(2):413–419, 2002.

[87] C. Kittel. *Introduction to Solid State Physics*. Wiley, New York, 6th edition, 1986.

[88] Kitware, Inc. ParaView data analysis and visualization application.

[89] H. P Klug and L. E. Alexander. *X-Ray Diffraction Procedures For Polycrystalline and Amorphous Materials*, chapter 9. Wiley-Interscience, 2nd edition, 1974.

[90] C. C. Koch. Optimization of strength and ductility in nanocrystalline and ultrafine grained metals. *Scr. Mater.*, 49(7):657–662, 2003.

[91] C. C. Koch, D. G. Morris, K. Lu, and A. Inoue. Ductility of nanostructured materials. *MRS Bulletin*, 24:54–58, 1999.

[92] W. Kohn and L. J. Sham. Self-consistent equations including exchange and correlation effects. *Phys. Rev.*, 140(4A):A1133–, 1965.

[93] G. Kresse and J. Furthmüller. Efficient iterative schemes for ab initio total-energy calculations using a plane-wave basis set. *Phys. Rev. B*, 54(16):11169, 1996.

[94] C. E. Krill and R. Birringer. Estimating grain-size distributions in nanocrystalline materials from X-ray diffraction profile analysis. *Philos. Mag. A*, 77(3):621–640, 1998.

[95] C. E. Krill, H. Ehrhardt, and R. Birringer. Thermodynamic stabilization of nanocrystallinity. *Z. Metallk.*, 96(10):1134–1141, 2005.

[96] C. E. Krill, R. Haberkorn, and R. Birringer. *Handbook of nanostructured materials and nanotechnology*, volume 2, chapter Specification of Microstructure and Characterization by Scattering Techniques, pages 155–211. Academic Press, San Diego, CA, 2000.

[97] M.A. Krivoglaz. *Theory of X-Ray and Thermal-Neutron Scattering by Real Crystals*. Plenum Press, New York, 1969.

[98] Y. Kulkarni and R. J. Asaro. Are some nanotwinned fcc metals optimal for strength, ductility and grain stability? *Acta Mat.*, 57(16):4835–4844, 2009.

[99] M. Yu. Lavrentiev, R. Drautz, D. Nguyen-Manh, T. P. C. Klaver, and S. L. Dudarev. Monte carlo study of thermodynamic properties and clustering in the bcc Fe–Cr system. *Phys. Rev. B*, 75(1):014208, 2007.

[100] M. Legros, B. R. Elliott, M. N. Rittner, J. R. Weertman, and K. J. Hemker. Microsample tensile testing of nanocrystalline metals. *Philos. Mag. A*, 80(4):1017–1026, 2000.

[101] J. Li and F. Shimizu. Least-square atomic strain. Report, 2005.

[102] JCM Li. Petch relation and grain boundary sources. *Transactions of the Metallurgical Society of AIME*, 227:239, 1963.

[103] Ju Li. Atomeye: an efficient atomistic configuration viewer. *Model. Simul. Mater. Sci. Eng.*, 11(2):173–177, 2003. http://mt.seas.upenn.edu/Archive/Graphics/A/.

[104] Lan Li and Nasr M. Ghoniem. Twin-size effects on the deformation of nanotwinned copper. *Phys. Rev. B*, 79(7):075444, 2009.

[105] X. Z. Liao, S. G. Srinivasan, Y. H. Zhao, M. I. Baskes, Y. T. Zhu, F. Zhou, E. J. Lavernia, and H. F. Xu. Formation mechanism of wide stacking faults in nanocrystalline Al. *Appl. Phys. Lett.*, 84(18):3564–3566, 2004.

[106] X. Z. Liao, Y. H. Zhao, S. G. Srinivasan, Y. T. Zhu, R. Z. Valiev, and D. V. Gunderov. Deformation twinning in nanocrystalline copper at room temperature and low strain rate. *Appl. Phys. Lett.*, 84(4):592–594, 2004.

[107] X. Z. Liao, F. Zhou, E. J. Lavernia, D. W. He, and Y. T. Zhu. Deformation twins in nanocrystalline Al. *Appl. Phys. Lett.*, 83(24):5062–5064, 2003.

[108] H. Lin, W. Chen, and G. Wang. Curve reconstruction based on an interval B-spline curve. *The Visual Computer*, 21(6):418–427, 2005.

[109] Y. Liu, H. Yang, and W. Wang. Reconstructing B-spline curves from point clouds – a tangential flow approach using least squares minimization. *International Conference on Shape Modeling and Applications*, pages 4–12, 2005.

[110] J. Löffler and J. Weissmüller. Grain-boundary atomic structure in nanocrystalline palladium from x-ray atomic distribution functions. *Phys. Rev. B*, 52(10):7076–7093, 1995.

[111] K. Lu, L. Lu, and S. Suresh. Strengthening materials by engineering coherent internal boundaries at the nanoscale. *Science*, 324(5925):349–352, 2009.

[112] L. Lu, X. Chen, X. Huang, and K. Lu. Revealing the maximum strength in nanotwinned copper. *Science*, 323(5914):607–610, 2009.

[113] L. Lu, R. Schwaiger, Z.W. Shan, M. Dao, K. Lu, and S. Suresh. Nano-sized twins induce high rate sensitivity of flow stress in pure copper. *Acta Mat.*, 53(7):2169–2179, 2005.

[114] L. Lu, Y. Shen, X. Chen, L. Qian, and K. Lu. Ultrahigh strength and high electrical conductivity in copper. *Science*, 304(5669):422–426, 2004.

[115] L. Lu, T. Zhu, Y. Shen, M. Dao, K. Lu, and S. Suresh. Stress relaxation and the structure size-dependence of plastic deformation in nanotwinned copper. *Acta Mat.*, 57(17):5165–5173, 2009.

[116] M. Mäntylä. *An introduction to solid modeling*. Computer Science Press, New York, 1987.

[117] J. Markmann, V. Yamakov, and J. Weissmüller. Atomic structure of nanocrystalline palladium: Experiment versus molecular dynamics. In *Poster Presentation at the International Conference on Nanostructured Materials*, Orlando, FL, 2002.

[118] J. Markmann, V. Yamakov, and J. Weissmüller. Validating grain size analysis from x-ray line broadening: A virtual experiment. *Scripta Mater.*, 59:15–18, 2008.

[119] Y. Matsuo, A. Nagasawa, and J. Kakinoki. Ordered alloys of the gold-palladium system. II. electron diffraction study on evaporated $AuPd_3$ films. *J. Phys. Soc. Jpn.*, 21(12):2633–2637, 1966.

[120] T. R. Mattsson and A. E. Mattsson. Calculating the vacancy formation energy in metals: Pt, Pd, and Mo. *Phys. Rev. B*, 66(21):214110–, 2002.

[121] J. May, H.W. Höppel, and M. Göken. Strain rate sensitivity of ultrafine-grained aluminium processed by severe plastic deformation. *Scr. Mater.*, 53(2):189–194, 2005.

[122] M. I. Mendelev, S. Han, D. J. Srolovitz, G. J. Ackland, D. Y. Sun, and M. Asta. Development of new interatomic potentials appropriate for crystalline and liquid iron. *Phil. Mag.*, 83(35):3977, 2003.

[123] M. Methfessel, D. Hennig, and M. Scheffler. Trends of the surface relaxations, surface energies, and work functions of the 4d transition metals. *Phys. Rev. B*, 46(8):4816, 1992.

[124] M. A. Meyers, A. Mishra, and D. J. Benson. Mechanical properties of nanocrystalline materials. *Prog. Mater. Sci.*, 51(4):427–556, 2006.

[125] M. A. Meyers, O. Vöhringer, and V. A. Lubarda. The onset of twinning in metals: a constitutive description. *Acta Mat.*, 49(19):4025–4039, 2001.

[126] P. C. Millett, R. P. Selvam, and A. Saxena. Molecular dynamics simulations of grain size stabilization in nanocrystalline materials by addition of dopants. *Acta Mat.*, 54(2):297–303, 2006.

[127] P. C. Millett, R. P. Selvam, and A. Saxena. Stabilizing nanocrystalline materials with dopants. *Acta Mat.*, 55(7):2329–2336, 2007.

[128] P. C. Millett, R. P. Selvan, S. Bansal, and A. Saxena. Atomistic simulation of grain boundary energetics - effects of dopants. *Acta Mat.*, 53(13):3671–3678, 2005.

[129] Y. Mishin, M. J. Mehl, D. A. Papaconstantopoulos, A. F. Voter, and J. D. Kress. Structural stability and lattice defects in copper: Ab initio, tight-binding, and embedded-atom calculations. *Phys. Rev. B*, 63(22):224106, 2001.

[130] J. Monk, B. Hyde, and D. Farkas. The role of partial grain boundary dislocations in grain boundary sliding and coupled grain boundary motion. *J. Mater. Sci.*, 41(23):7741–7746, 2006.

[131] P. H. Mott, A. S. Argon, and U. W. Suter. The atomic strain tensor. *J. Comput. Phys.*, 101(1):140–150, 1992.

[132] M. Murayama, J. M. Howe, H. Hidaka, and S. Takaki. Atomic-level observation of disclination dipoles in mechanically milled, nanocrystalline Fe. *Science*, 295(5564):2433–2435, 2002.

[133] A. Nagasawa, Y. Matsuo, and J. Kakinoki. Ordered alloys of gold-palladium system. I. electron diffraction study of evaporated Au_3Pd films. *J. Phys. Soc. Jpn.*, 20(10):1881–1885, 1965.

[134] P. Olsson, J. Wallenius, C. Domain, K. Nordlund, and L. Malerba. Two-band modeling of alpha-prime phase formation in Fe-Cr. *Phys. Rev. B*, 72(21):214119, 2005.

[135] I. A. Ovid'ko. Materials science: Deformation of nanostructures. *Science*, 295(5564):2386–, 2002.

[136] C. S. Pande, R. A. Masumura, and R. W. Armstrong. Pile-up based hall-petch relation for nanoscale materials. *Nanostructured Materials*, 2(3):323–331.

[137] N. I. Papanicolaou and D. A. Papaconstantopoulos. Interatomic potential for pd and molecular-dynamics simulation of diffusion in Pd/Pd(111) system. *Thin Solid Films*, 428(1-2):40–46, 2003.

[138] Persistence of Vision Pty. Ltd. Persistence of vision raytracer (version 3.6) [computer software]. Retrieved from http://www.povray.org/.

[139] S. Plimpton. Fast parallel algorithms for short-range molecular dynamics. *J. Comp. Phys.*, 117(1):1, 1995. Software available at http://lammps.sandia.gov/.

[140] B. Polak and G. Ribiere. Note surla convergence des méthodes de directions conjuguées. *Rev. Fr. Imform. Rech. Oper.*, 16:35–43, 1969.

[141] E.W. Qin, L. Lu, N.R. Tao, J. Tan, and K. Lu. Enhanced fracture toughness and strength in bulk nanocrystalline Cu with nanoscale twin bundles. *Acta Mat.*, 57(20):6215–6225, 2009.

[142] R. K. Rajgarhia, D. E. Spearot, and A. Saxena. Heterogeneous dislocation nucleation in single crystal copper-antimony solid-solution alloys. *Model. Simul. Mater. Sci. Eng.*, 17(5):055001 (13 pp.)–055001, 2009.

[143] D. C. Rapaport. *The art of molecular dynamics simulation*. Cambridge University Press, 1995.

[144] J. R. Rice. Dislocation nucleation from a crack tip: An analysis based on the Peierls concept. *J. Mech. Phys. Solids*, 40(2):239–271, 1992.

[145] A. E. Romanov. Importance of disclinations in severe plastically deformed materials. *Adv. Eng. Mater.*, 5(5):301–307, 2003.

[146] C. H. Rycroft, G. S. Grest, J. W. Landry, and M. Z. Bazant. Analysis of granular flow in a pebble-bed nuclear reactor. *Phys. Rev. E*, 74(2):021306, 2006.

[147] B. Sadigh, P. Erhart, A. Stukowski, and A. Caro. Composition-dependent interatomic potentials: A systematic approach to modelling multicomponent alloys. *Philos. Mag.*, 89(34):3371–3391, 2009.

[148] P. G. Sanders, J. A. Eastman, and J. R. Weertman. Elastic and tensile behavior of nanocrystalline copper and palladium. *Acta Mat.*, 45(10):4019–4025, 1997.

[149] R. A. Sayle and E. J. Milner-White. RasMol: Biomolecular graphics for all. *Trends Biochem. Sci.*, 20:374–376, 1995.

[150] J. Schiotz, . D. Di Tolla, and K. W. Jacobsen. Softening of nanocrystalline metals at very small grain sizes. *Nature*, 391(6667):561–563, 1998.

[151] J. Schiotz and K. W. Jacobsen. A maximum in the strength of nanocrystalline copper. *Science*, 301(5638):1357–1359, 2003.

[152] T. C. Schulthess, P. E. A Turchi, A. Gonis, and T.-G. Nieh. Systematic study of stacking fault energies of random Al-based alloys. *Acta Mat.*, 46(6):2215–2221, 1998.

[153] A. Seeger, D. Schumacher, W. Schilling, and J. Diehl. *Vacancies and Interstitials in Metals*. North-Holland, Amsterdam, 1970.

[154] I. Shabib and R. E. Miller. Deformation characteristics and stress-strain response of nanotwinned copper via molecular dynamics simulation. *Acta Mat.*, 57(15):4364–4373, 2009.

[155] I. Shabib and R. E. Miller. A molecular dynamics study of twin width, grain size and temperature effects on the toughness of 2d-columnar nanotwinned copper. *Model. Simul. Mater. Sci. Eng.*, (5):055009, 2009.

[156] L. E. Shilkrot, R. E. Miller, and W. A. Curtin. Coupled atomistic and discrete dislocation plasticity. *Phys. Rev. Lett.*, 89(2):025501, 2002.

[157] F. Shimizu, S. Ogata, and J. Li. Theory of shear banding in metallic glasses and molecular dynamics calculations. *Mater. Trans.*, 48(11):2923–2927, 2007.

[158] C. J. Shute, B. D. Myers, S. Xie, T. W. Barbee Jr., A. M. Hodge, and J. R. Weertman. Microstructural stability during cyclic loading of multilayer copper/copper samples with nanoscale twinning. *Scr. Mater.*, 60(12):1073–1077, 2009.

[159] G. Simmons and H. Wang. *Single Crystal Elastic Constants and Calculated Aggregate Properties: A Handbook*. MIT Press, Cambridge, Massachusetts, 1971.

[160] M. H. F. Sluiter, C. Colinet, and A. Pasturel. Ab initio calculation of the phase stability in Au-Pd and Ag-Pt alloys. *Phys. Rev. B*, 73(17):174204, 2006.

[161] L. J. Sluys and Y. Estrin. The analysis of shear banding with a dislocation based gradient plasticity model. *Int. J. Solids Struct.*, 37(46–47):7127–7142, 2000.

[162] D. E. Spearot, K. I. Jacob, and D. L. McDowell. Nucleation of dislocations from [001] bicrystal interfaces in aluminum. *Acta Mat.*, 53(13):3579–3589, 2005.

[163] D. E. Spearot, K. I. Jacob, and D. L. McDowell. Dislocation nucleation from bicrystal interfaces with dissociated structure. *Int. J. Plast.*, 23(1):143–160, 2007.

[164] J. Stadler, R. Mikulla, and H.-R. Trebin. IMD: A software package for molecular dynamics studies on parallel computers. *International Journal of Modern Physics C*, 8:1131–1140, 1997.

[165] A. R. Stokes and A. J. C. Wilson. The diffraction of X-rays by distorted crystal aggregates - I. *Proceedings of the Physical Society*, 56(3):174–181, 1944.

[166] A. P. Sutton and R. W. Baluffi. *Interfaces in Crystalline Materials*. Clarendon Press, Oxford, 1995.

[167] A. P. Sutton and J. Chen. Long–range Finnis–Sinclair potentials. *Philos. Mag. Lett.*, 61(3):139–146, 1990.

[168] A. P. Sutton, P. A. Mulheran, and A. M. Stoneham. Direct free energy minimization methods: Application to grain boundaries [and discussion]. *Philos. Trans. R. Soc. A*, 341(1661):233–245, Nov. 16, 1992.

[169] E. B. Tadmor and N. Bernstein. A first-principles measure for the twinnability of fcc metals. *J. Mech. Phys. Solids*, 52(11):2507–2519, 2004.

[170] F. Tang and J. M. Schoenung. Strain softening in nanocrystalline or ultrafine-grained metals: A mechanistic explanation. *Mater. Sci. Eng. A*, 493:101–103, 2008.

[171] M. Tarini, P. Cignoni, and C. Montani. Ambient occlusion and edge cueing for enhancing real time molecular visualization. *IEEE T. Vis. Comput. Gr.*, 12(5):1237–1244, 2006.

[172] R. Tarjan. Enumeration of the elementary circuits of a directed graph. *SIAM Journal on Computing*, 2(3):211–216, 1973.

[173] G. Taubin. A signal processing approach to fair surface design. In *Computer Graphics Proceedings. SIGGRAPH 95*, Los Angeles, CA, USA, 1995.

[174] D. Tomanek, Z. Sun, and Steven G. Louie. Ab initio calculation of chemisorption systems: H on Pd(001) and Pd(110). *Phys. Rev. B*, 43(6):4699–, 1991.

[175] M. A. Tschopp and D. L. McDowell. Grain boundary dislocation sources in nanocrystalline copper. *Scr. Mater.*, 58(4):299–302, 2008.

[176] M. A. Tschopp, D. E. Spearot, and D. L. McDowell. Atomistic simulations of homogeneous dislocation nucleation in single crystal copper. *Model. Simul. Mater. Sci. Eng.*, 15(7):693–709, 2007.

[177] D. Udler and D. N. Seidman. Solute-atom segregation at symmetrical twist boundaries studied by Monte-Carlo simulation. *Physica Status Solidi B*, 172(1):267–285, 1992.

[178] T. Ungár and A. Borbely. The effect of dislocation contrast on x-ray line broadening: A new approach to line profile analysis. *Appl. Phys. Lett.*, 69(21):3173–3175, 1996.

[179] T. Ungár, I. Dragomir, A. Revesz, and A. Borbely. The contrast factors of dislocations in cubic crystals: the dislocation model of strain anisotropy in practice. *J. Appl. Crystallogr.*, 32(5):992–1002, 1999.

[180] T. Ungár, S. Ott, P. G. Sanders, A. Borbély, and J. R. Weertman. Dislocations, grain size and planar faults in nanostructured copper determined by high resolution x-ray diffraction and a new procedure of peak profile analysis. *Acta Mat.*, 46(10):3693–3699, 1998.

[181] T. Ungár, A. Revesz, and A. Borbely. Dislocations and grain size in electrodeposited nanocrystalline Ni determined by the modified Williamson–Hall and Warren–Averbach procedures. *J. Appl. Crystallogr.*, 31(4):554–558, 1998.

[182] G. Van Rossum. Python language website. http://www.python.org/.

[183] H. Van Swygenhoven. Polycrystalline materials: Grain boundaries and dislocations. *Science*, 296(5565):66–67, 2002.

[184] H. Van Swygenhoven and P. M. Derlet. Grain-boundary sliding in nanocrystalline fcc metals. *Phys. Rev. B*, 64(22):224105, 2001.

[185] H. Van Swygenhoven, P. M. Derlet, and A. G. Froseth. Stacking fault energies and slip in nanocrystalline metals. *Nat. Mater.*, 3(6):399–403, 2004.

[186] H. Van Swygenhoven, P.M. Derlet, and A. G. Froseth. Nucleation and propagation of dislocations in nanocrystalline fcc metals. *Acta Mat.*, 54(7):1975–1983, 2006.

[187] H. Van Swygenhoven, M. Spaczer, and A. Caro. Microscopic description of plasticity in computer generated metallic nanophase samples: a comparison between Cu and Ni. *Acta Mat.*, 47(10):3117–3126, 1999.

[188] H. Van Swygenhoven and J. R. Weertman. Deformation in nanocrystalline metals. *Materials Today*, 9(5):24–31, 2006.

[189] N. Q. Vo, R. S. Averback, P. Bellon, and A. Caro. Limits of hardness at the nanoscale: Molecular dynamics simulations. *Phys. Rev. B*, 78(24):241402, 2008.

[190] N. Q. Vo, R. S. Averback, P. Bellon, and A. Caro. Yield strength in nanocrystalline Cu during high strain rate deformation. *Scr. Mater.*, 61(1):76–79, 2009.

[191] N. Q. Vo, R. S. Averback, P. Bellon, S. Odunuga, and A. Caro. Quantitative description of plastic deformation in nanocrystalline Cu: Dislocation glide versus grain boundary sliding. *Phys. Rev. B*, 77(13):134108, 2008.

[192] F. A. Volkening, M. N. Naidoo, G. A. Candela, R. L. Holtz, and V. Provenzano. Characterization of nanocrystalline palladium for solid-state gas sensor applications. *Nanostructured Materials*, 5(3):373–382, 1995.

[193] B. Von Sydow, J. Hartford, and G. Wahnstrom. Atomistic simulations and Peierls-Nabarro analysis of the Shockley partial dislocations in palladium. *Comput. Mater. Sci.*, 15(3):367–379, 1999.

[194] G. Z. Voronoi. *J. Reine Angew. Math.*, 134:199, 1908.

[195] VSG, Visualization Sciences Group, Inc. Avizo visualization software.

[196] A. Wachter, K. P. Bohnen, and K. M. Ho. Structure and dynamics at the Pd(100) surface. *Surf. Sci.*, 346(1-3):127–135, 1996.

[197] J. Wallenius, P. Olsson, C. Lagerstedt, N. Sandberg, R. Chakarova, and V. Pontikis. Modeling of chromium precipitation in Fe–Cr alloys. *Phys. Rev. B*, 69(9):094103, 2004.

[198] H. Y. Wang, R. Najafabadi, D. J. Srolovitz, and R. Lesar. Segregation to Sigma-5 [001] twist grain-boundaries in Ni-Cu alloys. *Philos. Mag. A*, 65(3):625–655, 1992.

[199] W. Wang, H. Pottmann, and Y. Liu. Fitting B-spline curves to point clouds by squared distance minimization. *ACM Trans. Graphics*, 25(2):214–238, 2006.

[200] Y. B. Wang, B. Wu, and M. L. Sui. Dynamical dislocation emission processes from twin boundaries. *Appl. Phys. Lett.*, 93(4):041906, 2008.

[201] B.E. Warren. *X-ray Diffraction*. Dover, New York, 1990.

[202] Q. Wei, S. Cheng, K. T. Ramesh, and E. Ma. Effect of nanocrystalline and ultrafine grain sizes on the strain rate sensitivity and activation volume: fcc versus bcc metals. *Mater. Sci. Eng. A*, 381(1-2):71–79, 2004.

[203] K. Weiler. Edge-based data structures for solid modeling in curved-surface environments. *IEEE Comput. Graph.*, 5:21–40, 1985.

[204] J. Weissmüller. Alloy effects in nanostructures. *Nanostructured Materials*, 3(1-6):261–272, 1993.

[205] J. Weissmüller. Grain-boundaries and their impact on thermodynamic equilibrium. In A.R. Dinesen, M. Eldrup, D. Juul-Jensen, S. Linderoth, T.B. Pedersen, N.H. Pryds, A. Schrøder-Pedersen, and J.A. Wert, editors, *Science of Metastable and Nanocrystalline Alloys: Structure Properties and Modelling*, pages 155–176, Roskilde, Denmark, 2001. 5th Risø International Symposium on Materials Science, Risø National Laboratory.

[206] J. Weissmüller, J. Löffler, and M. Kleber. Atomic structure of nanocrystalline metals studied by diffraction techniques and EXAFS. *Nanostructured Materials*, 6(1-4):105–114, 1995.

[207] J. Weissmüller and J. Markmann. Deforming nanocrystalline metals: New insights, new puzzles. *Adv. Eng. Mater.*, 7(4):202–207, 2005.

[208] G. K. Williamson and R. E. Smallman. III. Dislocation densities in some annealed and cold-worked metals from measurements on the X-ray Debye-Scherrer spectrum. *Philos. Mag.*, 1(1):34–46, 1955.

[209] D. Wolf, V. Yamakov, S.R. Phillpot, A. Mukherjee, and H. Gleiter. Deformation of nanocrystalline materials by molecular-dynamics simulation: relationship to experiments. *Acta Mat.*, 53(1):1–40, 2005.

[210] Z. X. Wu, Y. W. Zhang, and D. J. Srolovitz. Dislocation-twin interaction mechanisms for ultrahigh strength and ductility in nanotwinned metals. *Acta Mat.*, 57:4508–4518, 2009.

[211] V. Yamakov, D. Moldovan, K. Rastogi, and D. Wolf. Relation between grain growth and grain-boundary diffusion in a pure material by molecular dynamics simulations. *Acta Mat.*, 54(15):4053–4061, 2006.

[212] V. Yamakov, D. Wolf, S. R. Phillpot, and H. Gleiter. Deformation twinning in nanocrystalline Al by molecular-dynamics simulation. *Acta Mat.*, 50(20):5005–5020, 2002.

[213] V. Yamakov, D. Wolf, S. R. Phillpot, and H. Gleiter. Grain-boundary diffusion creep in nanocrystalline palladium by molecular-dynamics simulation. *Acta Mat.*, 50(1):61–73, 2002.

[214] V. Yamakov, D. Wolf, S. R. Phillpot, A. K. Mukherjee, and H. Gleiter. Dislocation processes in the deformation of nanocrystalline aluminium by molecular-dynamics simulation. *Nat. Mater.*, 1(1):45–48, 2002.

[215] V. Yamakov, D. Wolf, S. R. Phillpot, A. K. Mukherjee, and H. Gleiter. Deformation-mechanism map for nanocrystalline metals by molecular-dynamics simulation. *Nat. Mater.*, 3(1):43–47, 2004.

[216] Z. Yang, J. Deng, and F. Chen. Fitting unorganized point clouds with active implicit B-spline curves. *The Visual Computer*, 21(8):831–839, 2005.

[217] S. Yip. Nanocrystals - the strongest size. *Nature*, 391(6667):532–533, 1998.

[218] Z. S. You, L. Lu, and K. Lu. Temperature effect on rolling behavior of nano-twinned copper. *Scr. Mater.*, 62(6):415–418, 2010.

[219] A. Zaluska, L. Zaluski, and J. O. Strom-Olsen. Nanocrystalline magnesium for hydrogen storage. *J. Alloy. Compd.*, 288(1-2):217–225, 1999.

[220] Y. W. Zhang, P. Liu, and C. Lu. Molecular dynamics simulations of the preparation and deformation of nanocrystalline copper. *Acta Mat.*, 52(17):5105–5114, 2004.

[221] H. Zhou and S. Qu. The effect of nanoscale twin boundaries on fracture toughness in nanocrystalline Ni. *Nanotechnology*, 21(3):035706, 2010.

[222] J. A. Zimmerman, D. J. Bammann, and H. Gao. Deformation gradients for continuum mechanical analysis of atomistic simulations. *Int. J. Solids Struct.*, 46(2):238–253, 2009.

[223] J. A. Zimmerman, H. Gao, and F. F. Abraham. Generalized stacking fault energies for embedded atom fcc metals. *Model. Simul. Mater. Sci. Eng.*, 8(2):103, 2000.

[224] J. A. Zimmerman, C. L. Kelchner, P. A. Klein, J. C. Hamilton, and S. M. Foiles. Surface step effects on nanoindentation. *Phys. Rev. Lett.*, 87(16):165507, 2001.